UNIVERSITY OF CALIFORNIA, MERCED

Chloride Selective Membranes in Outflow Geometries for Water Treatment and Power Generation

by

Neda Seyedhassantehrani

A dissertation submitted in partial satisfaction of the
requirements for the degree of
Doctor of Philosophy

in

Mechanical Engineering

Committee in charge:

Professor Jamse Palko
Professor Min Hwan Lee
Professor Venkattraman Ayyaswamy
Professor Erik Menke

2023

The dissertation of Neda Seyedhassantehrani is approved, and it is acceptable in quality and form for publication on microfilm and electronically:

Professor James Palko, Advisor	Date
Professor Min Hwan Lee, Chair	Date
Professor Venkattraman Ayyaswamy	Date
Professor Erik Menke	Date

University of California, Merced

2023

To my beloved family and friends,

This work is dedicated to you, for the countless sacrifices you've made and for being my pillars of strength and sources of inspiration. As I take this step forward in my academic journey, I carry with me the profound impact of your presence in my life.

Curriculum Vitae

EDUCATIONAL BACKGROUND

- Master of Science, Mechanical Engineering – Wichita State University, Wichita, KS, 2014 – 2017
- Master of Science, Chemical Engineering – Azad University, Science and Research Branch, Tehran, Iran, 2009 – 2012
- Bachelor of Science, Chemical Engineering – Azad University, Science and Research Branch, Tehran, Iran, 2002 – 2007

PUBLICATIONS & CONFERENCES

- **N. Seyedhassantehrani**, J. Palko, Outflow geometry for electrochemical desalination cells, Electrochimica Acta. 449 (2023) 142180.
- E.M. Dede, C. Zhang, Q. Wu, **N. Seyedhassantehrani**, M. Shattique, S. Roy, J.W. Palko, S. Narumanchi, B. Kekelia, S. Hazra, K.E. Goodson, R. Giglio, M. Asheghi, Techno-economic feasibility analysis of an extreme heat flux micro-cooler, IScience. 26 (2023) 105812.
- Ercan M. Dede, Sougata Hazra, Qianying Wu, Chi Zhang, Mehdi Asheghi, Kenneth E. Goodson, Muhammad Shattique, **Neda Seyedhassantehrani**, Souvik Roy, James Palko, Bidzina Kekelia, Gilbert Moreno, Sreekant Narumanchi.U.S. Patent Appln. No. 17/575,071 “Heat Flux Micro Coolers Having Multi-Stepped Features and Fluid Wicking”.
- **N. Seyedhassantehrani**, R. Faridi-Majidi, H. Attar, S. Mahdi, R. Sorkhabadi, Preparation of polymer nanofibers via the electrospinning technique for burn dressing purposes, J. Crit. Rev. 8 (2021) 17–27.
- F. Desai, **N. Seyedhassantehrani**, M. Shagar, S. Gu, R. Asmatulu, Preparation and characterization of KOH-treated electrospun nanofiber mats as electrodes for iron-based redox-flow batteries, J. Energy Storage. 27 (2020) 101053.

- **N. Seyedhassantehrani**, J. Palko, Advective approaches to enhancing throughput in electrochemical separations, presented at GRS, Ventura, USA. Oct 1-2, 2022
- **N. Seyedhassantehrani**, J. Palko, Microfluidic ionic separations using selective electrodes, presented at AIChE, San Francisco, USA. Nov 16-20, 2020
- **N. Seyedhassantehrani**, R. Faridi-Majidi, H. Attar, M. Rezayat "Controlled Release of Silver Sulfadiazine from Chitosan Electrospun Nanofibers for Burn Treatment" presented at 4th International Congress on Nanoscience & Nanotechnology (ICNN4), 2012, Kashan, I.R. Iran. 10 September 2012.
- **N. Seyedhassantehrani**, R. Faridi-Majidi, H. Attar, M. Rezayat "Burn-dressing Materials with Antibacterial Activity from Electrospun Chitosan Nanofiber Mats Containing Silver sulfadiazine" presented at 4th International Conference on Nanostructures (ICNS4), 2012, Kish Island, I.R. Iran. 13 March 2012

Table of Contents

Nomenclature

A	Projected electrode area (m^2)
ASR	Area specific resistance (resistance normalized by projected area) ($\Omega\ m^2$)
C	Concentration of NaCl in solution (mol m^{-3})
C_0	Inlet concentration (mol m^{-3})
C_{high}	Higher concentration (mol m^{-3})
C_{low}	Lower concentration (mol m^{-3})
C_M	Average of the feed concentrations (mol m^{-3})
D	Net diffusion coefficient of NaCl in solution (m^2 s)
E_{cell}	Equilibrium electrode potential (V)
F	Faraday's constant (96,485 C mol^{-1})
G	Total molar Gibbs free energy of solution (J mol^{-1})
G_{fresh}	Initial Gibbs free energy for freshwater (J mol^{-1})
G_i	Molar Gibbs energy of species i at temperature T and pressure P (J mol^{-1})
G_{salt}	Initial Gibbs free energy for saltwater (J mol^{-1})
G_{tot}	Gibbs free energy for the final mixture (J mol^{-1})
i	Current density (A m^{-2})
J	Molar flux (mol $m^{-2}s^{-1}$)
L	Distance between inlet and outlet (m)
n	Number of electrons (dimensionless)
Pe	Peclet number (dimensionless)
R	Universal gas constant (8.314 J mol^{-1} K^{-1})
s	Distance between inlet and electrodes positions (m)
T	Temperature (K)
u	Superficial velocity (m/s)

V Total potential across cell (V)

x Position (m)

x_i Mole fraction of species *i* in solution (dimensionless)

Greek letters

γ_i Activity coefficient of species *i* (dimensionless)

δ_{elec} Electrode thickness (m)

ΔC Concentration difference of NaCl between outlet and inlet (mol m^{-3})

ΔG_{mix} Gibbs free energy of mixing per mole ($Jmol^{-1}$)

η Charge efficiency (dimensionless)

Λ Molar conductivity of NaCl (S m^2/mol)

ν Number of ions each electrolyte molecule dissociates into (dimensionless)

ϕ Ratio of total moles in low concentration solution to total moles in system (dimensionless)

ϕ_{fresh} Ratio of the total moles of freshwater (dimensionless)

ϕ_{salt} Ratio of the total moles of saltwater (dimensionless)

ϕ_m Mesh porosity (dimensionless)

List of Figures

List of Tables

Abstract

Clean power generation and global water scarcity are two intertwined challenges that have become increasingly critical in our modern world. With the growth of population, the expansion of industrialization, and the disruption of traditional weather patterns, demand for energy and freshwater has surged. As a result, the world has turned its attention to innovative sustainable energy sources, offering a reliable and eco-friendly solution to our growing energy needs while protecting the environment from negative impacts associated with conventional energy generation methods.

The electrochemical cell explored in this study holds significant promise in three separate domains, with each domain playing a crucial role in tackling demanding global challenges. This cell demonstrates applicability in desalination, separation processes, and power generation.

The cell relies on the use of regenerable porous silver electrodes, which have the ability to selectively attract chloride ions through an electrochemical reaction involving silver and chloride. Symmetric silver/ silver chloride porous electrodes are employed to alternatively capture Cl^- ions. The silver anode is oxidized and reacts with Cl^- ions from the solution to form insoluble AgCl. Simultaneously, the silver cathode releases Cl^- ions. The distinctive feature here is the new geometry, allowing the inlet flow to extend outward through the porous electrodes. This feature minimizes the energy consumption of the process by alleviating concentration polarization through advection. Concentration polarization is one of the main contributors to energy loss in electrochemical processes.

Chapter one thoroughly explores strategies and technologies targeted at addressing environmental challenges, with a primary focus on desalination, separation, and power generation. The chapter emphasizes electrochemical methods as sustainable and efficient solutions for overcoming the environmental challenges Additionally, it introduces the electrochemical cell utilized in this study and outlines its role in addressing these environmental challenges.

In chapter two, our focus is entirely on the field of desalination. Desalination plays a pivotal role in addressing water scarcity, especially in regions with limited or contaminated freshwater sources. We delve into the growing application of electrochemical desalination methods. Our exploration of this system's behavior encompasses the use of steady-state analytical models, transient numerical models, and practical experimentation. Our analysis of desalination performance involves an assessment of the degree of separation attained, the system's throughput capacity, its charge efficiency, and its energy consumption [1].

In the third chapter, the system is harnessed for specific ion separation, capitalizing on the chemical selectivity of its electrodes. These capabilities for selective separation also prove to be a valuable asset for tackling urgent environmental issues in industries like food processing, leather production, and petroleum refineries. This chapter reports results of experiments to separate chloride ions from other anions present in solutions representative of industrial and agricultural wastewater.

Chapter 4 introduces a shift in the electrochemical cell's role, transitioning from desalination to power generation. This transformation is based on the cell's capability to harness energy arising from the difference in salt concentration between saltwater and freshwater, thereby introducing a renewable energy source. The analysis of power generation performance in this chapter relies on the use of steady-state analytical models. It involves a comprehensive exploration of the cell's behavior across a range of parameters. This examination encompasses the impact of different velocities, variations in inlet concentration differences, adjustments in electrode spacing, and diverse current levels.

We believe that there is a need for further research to optimize the utilization of the electrochemical cell across various applications, as will be discussed in chapter 5.

Collectively, our study emphasizes the potential of this electrochemical cell to serve as a bridge connecting the domains of desalination, selective separation, and power generation to address global challenges with issues such as water scarcity, the demand for sustainable energy sources, and environmental conservation.

Chapter 1

1. Introduction

Electrochemical approaches have emerged as potent tools in the fight against environmental concerns, particularly in the domains of desalination, wastewater treatment, and power generation. These innovative techniques leverage the principles of electrochemistry to provide sustainable and efficient solutions for some of the most pressing environmental challenges.

The heart of this study is dedicated to introducing an innovative geometry for an electrochemical cell. This novel approach seeks to provide comprehensive solutions to the most challenging environmental problems, desalination, wastewater treatment, and power generation. In this chapter, I will review the evolution of the technologies that have been developed to tackle the immediate concerns in the domains of desalination, wastewater treatment, and power generation.

1.1Need for Desalination

Freshwater scarcity is now a major global concern, driven by a combination of factors that are closely linked. The ever-expanding global population, the impact of human activities on the environment, including industrial processes and agriculture, and the consequences of climate change causing more frequent and severe droughts, and altering natural water cycles leads to major challenges for water resource management and sustainability. [2,3].

These factors collectively contribute to the rising need for freshwater. In response, there is an ongoing evolution of water treatment methods, all geared towards achieving two primary goals: improving the quality and increasing the quantity of available water resources. This led to the development of more effective and sustainable water treatment techniques to address the growing challenge of water scarcity and to ensure that communities worldwide have access to safe and clean drinking water.

1.1.1 Desalination

Desalination processes are methods used to reduce or completely remove salt from a solvent, typically water. In an ideal desalination technology, the process results in two distinct fractions: pure salt and pure water. In practice, complete separation of salt and water is often unnecessary, and desalinated water may require remineralization or treatment to make it potable. The selection of desalination technology is primarily determined by the cost rather than energy requirements (measured in kWh/m^3). An ideal technology meets process requirements at the lowest cost and with the least energy demand [2,3].

Desalination technologies involve splitting a water stream with a specific salt concentration into a concentrate or brine stream and a dilute or desalinated stream. The existence of a brine stream leads to water loss, which is undesirable. Achieving higher water recovery results in increased energy consumption and desalination costs [4,5]. Brine streams also present significant environmental challenges and can threaten marine ecosystems [3,6–8]. There are efforts to develop zero-liquid discharge (ZLD) technologies to treat brine streams [9–11]. ZLD technologies can also be used in combination with mineral and metal extraction from desalination concentrates [9,12–15].

Sustainability plays a critical role in desalination processes. Seawater desalination is energy-intensive, and this leads to integrating desalination with renewable energy sources [16–21] or desalination and energy production [21,22]. The future of desalination depends on using less energy and cleaner energy sources. This change is vital to move away from using polluting fossil fuels for freshwater and adopt ecofriendly methods.

1.1.2 Desalination Technologies

Desalination systems come in various types, classified based on their energy sources, such as thermal, mechanical, electrical, and chemical sources [23]. They can also be grouped according to the desalination process they use, including evaporation-condensation, filtration, and crystallization techniques. Some promising desalination technologies are still in the developmental phase, like solar chimney, greenhouse, natural vacuum, adsorption desalination, membrane

distillation (MD), membrane bioreactor (MBR), forward osmosis (FO), and ion exchange resin (IXR). However, the most widely implemented desalination technologies worldwide are reverse osmosis (RO), followed by multi-stage flashing (MSF) and multi-effects distillation (MED) systems [23,24]

Thermal desalination and membrane desalination are the two primary categories of desalination methods. Thermal desalination relies on heat as a driving force and has been historically prevalent in areas with low energy costs. Membrane desalination, which uses pressure as the driving force and is gaining favor due to its energy efficiency. RO is a particularly popular choice among membrane technologies because of its low energy consumption, high water recovery rates, and the production of high-quality freshwater. However, membrane fouling remains a challenge, which can be reduced through pretreatment or hydrophilic membranes.

Desalination methods vary across the globe based on regional preferences and resource availability. Western countries use energy-efficient RO systems. Meanwhile, in the Middle East, where there's an abundance of oil, MSF and MED systems are more commonly used. Ras Al-Khair is the largest desalination plant in Saudi Arabia, which began operations in 2014. This plant adopts both MSF and RO technologies, producing a significant 728,000 cubic meters of desalinated water daily. On the other hand, the second-largest desalination facility, Carlsbad in California, USA, employs RO technology and has been operational since December 2015, producing approximately 190,000 cubic meters of desalinated water per day [24,25].

Electrochemical desalination also offers an alternative way to extract salt ions from water using an electric potential. Two common methods in this category are electrodialysis (ED) and capacitive deionization (CDI), relying on creating an electric potential difference to purify water. In the following sections, a brief overview of various electrochemical desalination techniques will be discussed to provide insights on the diverse approaches utilized for water purification.

1.1.2.1 Electrodialysis and Electrodialysis Reversal

Electrodialysis and Electrodialysis Reversal (EDR) are innovative techniques for removing salt ions from water using electric potential as the driving force. In an electrodialysis system, two types of ion-exchange membranes, known as cation exchange membranes (CEM) and anion exchange membranes (AEM), are placed between electrodes. These membranes are arranged alternately within an electrodialysis stack, creating multiple electrodialysis cells. There is migration of positively charged cations such as Na^{+}, Ca^{2+}, and Mg^{2+} toward the cathode and negatively charged anions such as Cl^{-}, and $SO4^{2-}$ toward the anode. The selectivity and semipermeability of these membranes allow only one type of charge (either cations or anions) to pass through each membrane. This results in the concentration of salts in some areas and the generation of freshwater in others. Figure 1-1 displays an illustration of electrodialysis.

EDR also works on the same principles, with one key difference: the polarity of the electrodes is periodically reversed. This reverses the migration direction of the ions, which is a unique feature for reducing scaling and fouling. This reduction in membrane fouling significantly extends the lifespan of the membranes used in the process.

Both ED and EDR systems can achieve high water recovery. This means they can efficiently reduce the volume of concentrated brine produced, especially when compared to technologies like RO. However, it's essential to consider that the energy cost for treatment tends to increase as the total dissolved solids in the feedwater rise, making it a factor to be mindful of in desalination operations [4,26–31].

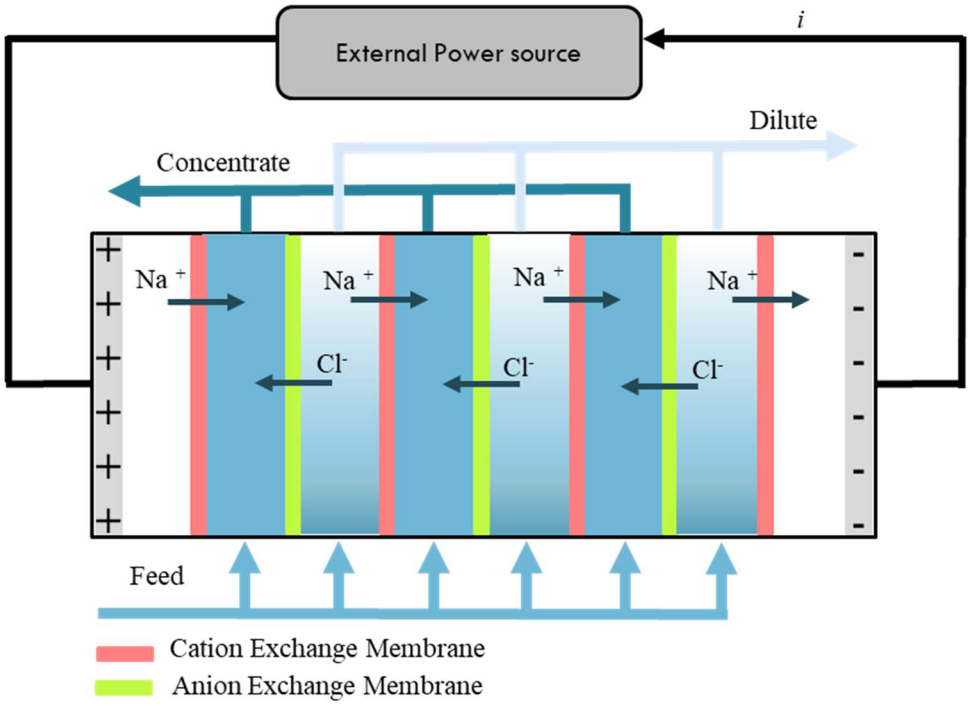

Figure 1-1 Principle of electrodialysis

1.1.2.2 Capacitive Deionization and Desalination Batteries

Capacitive Deionization is an innovative desalination method that relies on electrical forces to remove salt from water. In this process, an electric field is applied across two porous electrodes positioned near a flow channel, driving the migration of ions from the feedwater towards these electrodes. These ions are temporarily absorbed within an electrical double layer (EDL) forming on the porous electrode surfaces [32–35]. Typically, a negatively charged electrode (cathode) attracts cations, while a positively charged electrode (anode) attracts anions. To enhance the selectivity of this process, an Ion-Exchange Membrane (IEM) can be applied, leading to what's known as Membrane Capacitive Deionization (MCDI).

As water flows along these electrodes, ions are removed, resulting in the production of a diluted stream. However, after a certain period of applying an electric current to the electrodes, the electrodes reach their ion adsorption

capacity. This is when the ion release step occurs: the current is turned off, and ions return to the solution between the electrodes, forming a concentrated stream. This intermittent cycle of ion removal and release creates both diluted and concentrated streams. A portion of the applied current can be reclaimed in the discharge step, adding to the efficiency of the process.

CDI is particularly well-suited for water with low to moderate salt concentrations. As the ion concentration in the solution increases, the required voltage for CDI also rises. It's worth noting that CDI consumes 30-50% more energy for seawater desalination compared to RO, a more traditional desalination method [36]. Scaling, which can affect water quality and energy consumption, is another challenge associated with CDI [37]. However, CDI offers the advantage of operating at room temperature and pressure at low voltages. One limitation is that the salt adsorption capacity of the electrode is constrained by its surface area, a constraint that can be alleviated by using electrodes with electrochemical reactions [38–42]. Figure 1-2 depicts the schematic design of a cell for CDI.

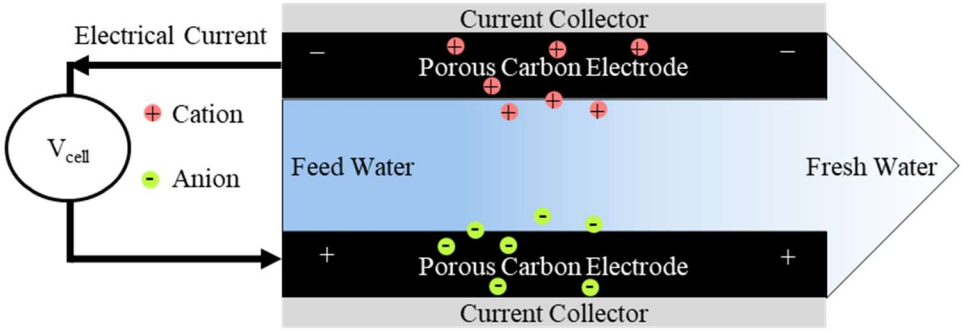

Figure 1-2 Schematic design of a cell for capacitive deionization

1.1.2.3 Ion Shuttling

Smith and his research team have introduced a unique desalination method that utilizes symmetric electrochemical desalination electrodes, drawing inspiration from electrodialysis. These electrodes are equipped with redox-active intercalation host compounds (IHCs) capable of absorbing cations within the host lattice through a reduction reaction of species found within the IHC. This innovative approach is known as cation intercalation desalination (CID), wherein desalination occurs on

one electrode, and the other electrode concentrates the salt. Specifically, the positive electrode, enriched with Na^+ ions, releases Na^+ ions into the electrolyte through an oxidation reaction, while the negative electrode absorbs Na^+ ions from the electrolyte via a reduction reaction. This process establishes a salt concentration gradient, resulting in two distinct streams with varying salt concentrations [43–45].

Smith and his team pioneered the use of an electrochemical cell with symmetric electrodes containing Na-ion intercalants for desalination, known as NID. Their belief is that a cell featuring Na in both electrodes offers better volumetric desalination capacity compared to CDI. The key distinction lies in the fact that, in CDI, charges are only stored in the double layer, whereas NID allows charges to be stored inside electroactive particles as well.

Figure 1-3 illustrates the ion shuttling with symmetric electrodes desalination process during charging. In the figure, we can see that sodium ions on the left side (cathode) move from the electroactive material into the electrolyte, while sodium ions on the right side (anode) move into the electroactive material. The difference in sodium ion concentration in the solution between the two electrodes drives chloride ion migration from the anode to the cathode. This results in a concentration increase of both sodium and chloride ions in the cathode solution, while the anode solution becomes more diluted in both ions.

Smith's approach also incorporates a membrane to separate concentrated and dilute streams, bearing similarities to electrodialysis as it relies on a selective membrane, specifically anion exchange in this instance. This novel desalination technique opens up promising possibilities for efficient and sustainable salt removal from water sources.

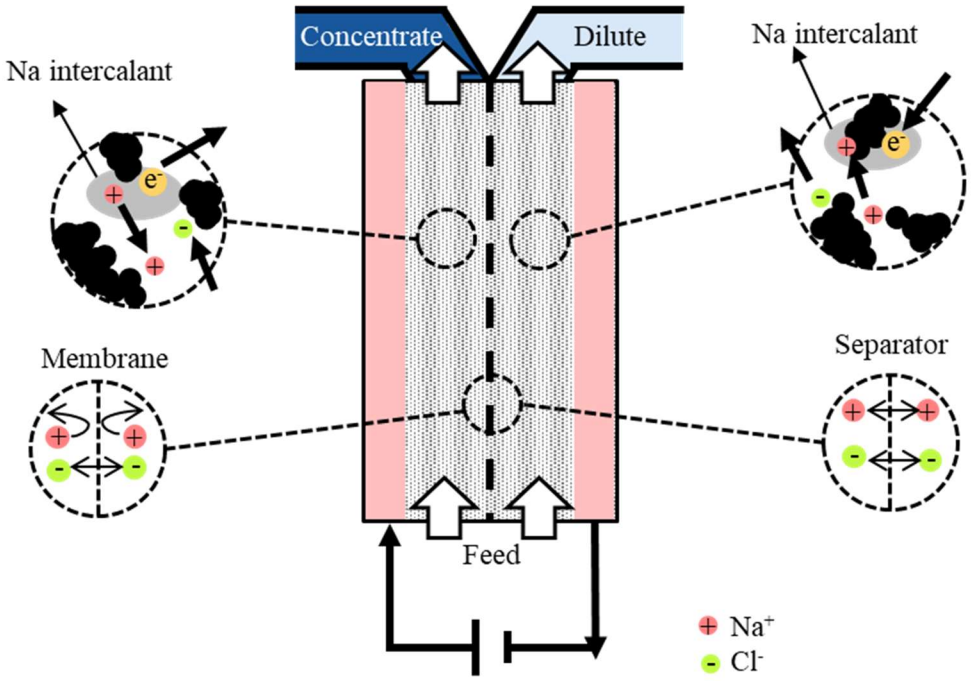

Figure 1-3 Schematic of the ion shuttling desalination with symmetric electrodes during a charging cycle

1.2Need for Separation

The issue of dealing with large amounts of wastewater containing salt and organic substances is a big environmental challenge. If not handled properly, this wastewater can harm various aspects of the environment, especially soil, surface water, and groundwater. It can contaminate soil, disrupt water ecosystems, and make surface and groundwater unsafe. This can lead to problems like soil becoming too salty for farming and water pollution that threatens aquatic life and the availability of clean drinking water.

To address these environmental concerns, strict rules have been put in place by organizations and governments. These rules are aimed at reducing the negative effects of salty wastewater discharge. Recently, these rules have gained more attention as people become more aware of the need to protect the environment and natural resources. The main goal of these rules is to encourage responsible management and treatment of salty wastewater to reduce harm to soil, surface water, and groundwater.

Several major industries, such as food processing, leather production, and petroleum manufacturing, produce a lot of salty wastewater. These industries are now required to follow these stricter rules and invest in better treatment processes to limit the environmental impact of their activities. By making these changes, they not only meet legal requirements but also show their dedication to taking care of the environment and conserving resources.

1.2.1 Separation

The contamination of subsurface soils and groundwaters with heavy metals can result from human activities, including the discharge of industrial waste, the use of fertilizers and pesticides, mining, metal plating, and vehicle emissions.

To address the challenge of heavy metal contamination, a range of specialized processes have been developed for both removing heavy metals from waste discharges and remediating contaminated soils and groundwaters. Among these techniques, numerous physical and chemical methods have been thoroughly studied and implemented. Some key approaches include chemical precipitation, coagulation and flocculation, ion exchange, solvent extraction, cementation, complexation, electrochemical operations, evaporation, and filtration [46]. These diverse methods are crucial in effectively separating and removing heavy metals from the environment, ensuring the protection of ecosystems and human health.

1.2.2 Separation Approaches

Some industries handle the treatment of dilute liquid mixtures, while others face the challenge of dealing with highly concentrated wastewater loaded with toxic elements and heavy metals. There are industries still relying on traditional techniques such as distillation, crystallization, and drying, primarily because they have a long history of using these methods and are comfortable with them. However, there is a growing demand for more effective approaches to handle wastewater. The choice of separation methods is crucial both economically and environmentally, and it depends on several factors like improved selectivity, improved energy efficiency, development of new process configuration and

integration, economic viability, environmental safety and compatibility, and sustainability (recycle and reuse) [46,47].

Engineers and scientists have been actively exploring and enhancing various methods to improve the efficiency and reduce the costs associated with traditional separation techniques. These separation processes can be categorized based on the phases involved [47].

i. Solid-solid separation: This includes methods like screening, classification, flotation, flocculation, and field-based techniques for separating solid particles from one another.

ii. Solid-liquid separation: Involves processes such as thickening, centrifugation, filtration, drying, and crystallization, which are used to separate solid particles from liquid.

iii. Solid-gas separation: This category covers techniques like cyclones, filters, and adsorption for separating solid particles from gases.

iv. Liquid-liquid separation: Includes methods such as distillation, extraction, membrane processes, and adsorption for separating different liquids from one another.

v. Liquid-gas separation: Encompasses processes like absorption, stripping, and pervaporation, used for separating gases from liquids.

vi. Gas-gas separation: Involves the use of membranes to separate different gases from one another.

vii. Solid-liquid-gas separation: This category addresses complex processes that involve the separation of solids, liquids, and gases simultaneously.

This study will explore various separation methods relevant to common ions. These methods include ion exchange, membrane filtration, chemical precipitation, and electrodialysis, which have been reported as effective approaches for treating wastewaters.

1.2.2.1 Membrane Filtration

Pressure-driven membrane processes like microfiltration (MF), ultrafiltration (UF), nanofiltration (NF), and reverse osmosis play a significant role in water treatment. These processes rely on the differences in pressure across a membrane to separate dissolved and undissolved substances in wastewater. The choice of the specific membrane process depends on the size of particles and molecules that need to be retained, with each category offering a distinct level of filtration. Membrane filtration includes four main subcategories.

Microfiltration membranes are used to remove impurities, including particles, viruses, and bacteria, in the size range of 0.1–10 mm from a solvent or other low molecular weight components. This separation process relies on a sieving effect, with particles separated based on their dimensions, allowing for some charge or adsorptive separation. MF operates at relatively low pressures (<2 bars) [48,49].

Ultrafiltration is a separation process well-suited for particles in the size range of 0.01-0.1 μm, including microorganisms, proteins, colloids, turbidity, fungi, and more. Unlike RO membranes, UF membranes do not produce a significant osmotic pressure because their porous structure, with pore sizes between 1 and 100 nm, permits the permeation of small solutes (with molecular weights less than 300) through the membranes. UF membranes function as barriers that effectively separate macromolecules, colloids, and solutes with molecular weights exceeding 10,000 from smaller, lower molecular weight species. The driving force for UF relies on hydrostatic pressure differences, typically in the range of 1-10 bars. The selectivity of UF membranes is based on variations in the size and surface charge of the components to be separated, the properties of the membrane itself, and the hydrodynamic conditions within the system [49,50].

Nanofiltration membranes consist of multiple-layer thin-film polymer composites with negatively charged chemical groups. They are used to retain molecular solids like sugar and certain multivalent salts such as magnesium sulfate while allowing the passage of most monovalent salts like sodium chloride. NF operates at pressures of about 14 bars or 200 psig.

These membranes effectively reject substances with sizes in the range of 0.0005–0.007 mm, including color, viruses, hardness, calcium ions, magnesium ions, iron ions, permanganate ions, phosphate ions, and sulfate ions. NF membranes, with pore sizes ranging from 1-10 nm, work by excluding particles based on size and utilizing charge interactions between the membrane's surface and the ions in the solution. They are useful for treating drinking water as they can efficiently remove divalent cations such as calcium and magnesium, effectively reducing water hardness without the need for traditional chemical softening methods. Additionally, NF membranes can reject larger organic molecules that contribute to taste, odor, and the formation of disinfection byproducts when exposed to chlorine, enhancing downstream disinfection processes [49,51–53]

Reverse osmosis processes have membranes with tiny pores (0.1-1 nm) and operate at high pressures (20-50 bars) [49,54–56]. These RO membranes are able to reject organics and monovalent ions like sodium, potassium, and chloride. RO works based on semi-permeable membranes, allowing a substantial flow of water while blocking colloids, ions, and charged particles (high water permeability and low solute permeability). High-quality RO membranes can achieve an impressive 99.7% rejection of sodium chloride (NaCl) [57]. To make water pass through these membranes, pressure exceeding the osmotic pressure is applied. In seawater desalination, pressures generally range from 55 to 68 bar [3], and spiral wound membrane configurations [58] are commonly used. Modern seawater RO systems often incorporate energy recovery mechanisms, which significantly reduce energy consumption to less than 2 kWh/m³ of freshwater [3,58]. RO is predominantly employed in seawater desalination, but it is also applied in brackish water desalination and water purification [3,59]. The focus of membrane development in this field is primarily on enhancing water permeability. Various membrane types, including nanostructured ceramics, mixed matrix membranes, block copolymer membranes, and thin film nanocomposite membranes, are in development to make desalination more efficient and cost-effective [60]. Figure 1-4 illustrates the schematic principles of reverse osmosis.

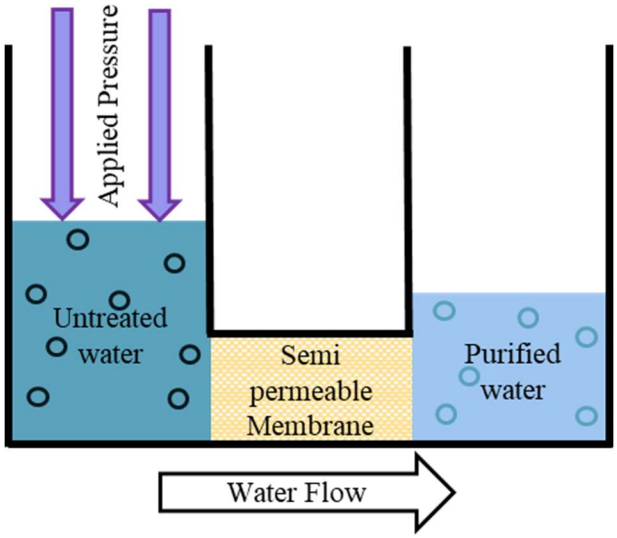

Figure 1-4 Schematic diagram illustrating the principles of reverse osmosis

1.2.2.2 Ion Exchange

Ion exchange (IX) is a powerful method that involves swapping ions between a solution and an ion exchanger. These exchangers come in two types: cation exchangers, which handle positively charged ions, and anion exchangers, designed for negatively charged ions. IX is used to purify, separate, and decontaminate solutions containing ions, making it an invaluable tool in water treatment. Ion exchangers can be in various forms, such as ion exchange resins, zeolites, clay, or soil humus.

In IX systems, water flows through the ion exchanger until it becomes saturated, resulting in an excess of the ions that need removal in the outgoing water. To regenerate the resin, backwashing removes accumulated solids, and flushed-out ions are replaced with a concentrated resin solution. However, the need for backwash can limit the application of IX in wastewater treatment. Fouling and contamination are other limitations.

Despite these limitations, IX offers cost-effective water treatment with low energy requirements and economical resin regeneration. Well-maintained resins can last for many years before needing replacement.

IX is widely used in various applications, including softening water, demineralization, and in the sugar and chemical industries, as well as in beverages and pharmaceutical manufacturing. Its advantages make it a popular choice in these fields [46,54,61].

1.2.2.3 Chemical Precipitation

Chemical precipitation is a method that converts soluble compounds into insoluble forms by introducing specific chemicals, creating a supersaturated environment where the solubility limit is exceeded. This transformation occurs through a series of stages, including nucleation, crystal growth, and flocculation [46].

The primary goal of chemical precipitation is to reduce the solubility of contaminants in various environmental applications. This technique is effective for addressing soluble ionic species, especially heavy metals. It is commonly used in the treatment of industrial wastewater and contaminated groundwater [46,62].

Chemical precipitation is most suitable for industrial wastewater and groundwater remediation, often employed with a pump-and-treat approach. Additionally, it can serve as a pre-treatment method for removing heavy metals from solutions before the biodegradation of hazardous organic compounds. Chemical precipitation offers a promising approach for the removal of soluble ionic species from aqueous solutions in various environmental and industrial contexts [46,62].

1.2.2.4 Electrodialysis

Electrodialysis is an electrochemical membrane separation technique that harnesses the power of an electric field as a driving force for its operation. This innovative process involves the selective movement of ions through specialized ion-exchange membranes, leading to the depletion of ions in the dilute effluent while concurrently enriching ions in the concentrated effluent [46,63,64].

As discussed in section 1.1.2.1, electrodialysis offers a remarkable capability to selectively separate ions based on their charge and characteristics. This means that

electrodialysis can be tailored to focus on specific ion types and achieve the desired separation outcomes [46,63–65].

The significance of electrodialysis lies in its versatility and precision in controlling ion movement. This factor led to the use of electrodialysis in various fields, including water treatment, desalination, and the separation of complex ionic mixtures. Electrodialysis offers an environmentally friendly and energy-efficient way to achieve ion separation, making it a valuable solution to address complex ion-related challenges [46,63–65].

1.3 Need for Power Generation

The demand for renewable energy is essential to combat pollution, reduce carbon emissions, and decrease our reliance on fossil fuels [66–68]. Technologies such as solar, wind, and geothermal power have gained significant attention in recent years as sources of clean energy. Additionally, there is growing interest in "salinity energy," which harnesses the salinity difference between seawater and freshwater as a substantial renewable energy source [69,70]. When a river meets the sea, irreversible mixing increases system entropy, which can be used to convert thermal energy into electricity [71]. It's estimated that every cubic meter of river water flowing into the sea dissipates about 2.3 MJ of free energy during the process, and a portion of this energy can be harnessed [71,72]. Worldwide, the potential for energy extraction from this "salinity potential" resource, when considering all river effluents combined, is estimated at roughly 2.4-2.6 TW. This amount is approaching the global electricity consumption in 2014, as noted in Jia et al.'s review paper on the topic [72–74].

1.3.1 Salinity Energy

Since the 1950s, scientists have investigated the potential of harnessing the salinity difference between freshwater and saltwater. By placing a suitable device between the flow of these waters, it becomes possible to capture the free energy stored in this salinity difference, creating what is now known as "blue energy" [73].

The Gibbs free energy, ΔG_{mix}, resulting from the mixing of two solutions with different concentrations, is an underestimated energy source that holds the potential for valuable work production [75–77]. This energy, often referred to as salinity gradient energy, osmotic power, or blue energy [78–82], can be harnessed from various sources. It can be naturally occurring, such as when fresh river water mixes with salty seawater in the hydrological cycle [75–77], or it can be generated from human activities, for instance, by combining desalination brine with low-salinity effluent from wastewater treatment [83–86].

1.3.2 Salinity Energy Approaches

Salinity gradient power generation technologies [81,84] encompass pressure retarded osmosis (PRO) [87–89], reverse electrodialysis (RED) [73,81,90], capacitive mixing (CapMix) and also battery mixing (BattMix) [74,91–93].

Moreover, alternative methods such as nano-fluidic diffusion techniques [94] and devices that leverage variations in vapor pressure [95] have been investigated to expand the options for harnessing blue energy.

1.3.2.1 Pressure Retarded Osmosis

Pressure-retarded osmosis harnesses the energy derived from the salinity gradient between river water and seawater, creating an osmotic pressure difference equivalent to a 231-meter dam or 23 atm under ordinary conditions [66,96–99]. This energy can be converted into mechanical energy or electricity. The PRO process utilizes semi-permeable membranes to facilitate the movement of water from a low-concentration solution (such as river or wastewater) to a high-concentration draw solution (seawater or brine water). This flow of water increases the static energy of the high-concentration side, which can be used to drive a turbine. The maximum energy that can be extracted during this mixing process is significant, ranging from 0.75 kWh to 14.1 kWh per cubic meter, depending on the low-concentration stream [96–103]

In a PRO plant, freshwater and seawater are sent through special modules with semi-permeable membranes. These membranes allow freshwater to move into pressurized seawater. The mixed solution is divided into two streams: one goes

through a hydropower turbine to make electricity, while the other stream passes through a pressure exchanger in order to pressurize incoming seawater. The plant has a high-pressure side for saltwater and a low-pressure side for freshwater. The pressure exchanger and membrane are crucial components, and when efficient versions are used, a PRO plant can generate about 1 MW from each cubic meter per second of freshwater passing through the membranes [101–104].

The effectiveness of PRO is restricted by its membrane properties. Membranes aren't perfectly impermeable to solutes, resulting in energy loss due to salt moving to freshwater. Another challenge is finding a membrane that allows sufficient flow, which has slowed PRO development for years. The challenge lies in fragile membranes; salt permeation decreases energy efficiency, and membrane contamination harms performance. Developing fouling-resistant and solutes-impermeable membranes with tailored properties and improved hydrodynamic mixing is essential. Graphene, an ultra-thin, strong membrane, shows promise. It could separate salt from water effectively, with high water transport rates and rejection of salt ions. If used in osmotic power plants, it could greatly improve energy output and efficiency [73].

1.3.2.2 Reverse electrodialysis

Reverse electrodialysis is a sustainable technology that directly converts energy from mixing two aqueous solutions into electrical power. It operates by passing seawater and freshwater through stacks of membranes that generate an electrochemical potential due to differences in solution concentration. This potential creates an electrical current, which is carried by an electrochemical redox couple to an external circuit [42,77,105,106]. Recent advancements have focused on improving membrane materials, spacing, and architecture to enhance RED power density and energy efficiency. However, challenges remain, including addressing electrode over-potentials and pumping losses, and reducing the cost of ion-exchange membranes for practical RED application [107–110].

1.3.2.3 Capacitive Mixing

Capacitive Mixing, introduced in 2009, and operates differently from PRO and RED [93]. Instead of relying on membranes, CapMix employs porous electrode pairs immersed in an electrolyte, acting like an electrical double layer capacitor [71,93]. In a simplified four-phase process, external electric potential charges the electrodes in phase I, causing ions in the electrolyte to accumulate near the electrode surface to maintain electro-neutrality. This charging process consumes energy. Then, in phase II, the high concentration solution is replaced with low concentration solution, reducing the capacitance of the electrical double layer due to changes in ionic strength. In phase III, controlled mixing takes place as ions diffuse into the low concentration solution, releasing stored charges and producing useful work. The energy output in phase III exceeds the energy consumed in phase I because discharge occurs at a higher potential difference. The low concentration solution is then replaced with high concentration solution in phase IV to complete the cycle. By repeating this process until concentration equilibrium is reached, CapMix makes efficient use of the salinity gradient to produce energy [86].

CapMix's controlled mixing is accomplished by the adsorption of ions to porous electrodes in the high salinity solution and their desorption in the low salinity environment. In an alternative CapMix setup, ion-exchange membranes can be used between the porous electrodes and the electrolyte [74,111,112]. These membranes allow selective ion passage, driving a current in the circuit and producing useful work. Switching to low concentration solution reverses the electrochemical gradient, causing ions to move across the ion-exchange membranes, leading to a change in current direction. While PRO and RED use mechanical and redox intermediates to convert salinity energy into electricity, CapMix directly produces electrical energy through controlled mixing [86].

1.3.2.4 Battery Mixing

Mixing entropy batteries or battery mixing, are similar to CapMix but use faradaic electrodes to convert the chemical energy in salinity gradients to electricity instead of using inert porous electrodes [92,113,114]. This technique employs electrodes like $MnO_2|Na_2Mn_5O_{10}$ as cathode and Ag|AgCl as anode with NaCl electrolyte [92]. In BattMix, the cell is charged by applying an external voltage, which moves Na^+ and Cl^- ions out of the electrodes into a low concentration

solution. To start the discharge, the low concentration solution is swapped with a high-concentration solution. This causes Na^+ ions to intercalate into the MnO_2 cathode, and Ag(s) is oxidized to Ag^+ ions at the anode. Since the energy produced during discharge through an external load is greater than the energy used during charging, controlled mixing of the salinity gradient results in net energy production. BattMix is a newer technology than PRO, RED, and CapMix, and shows significant potential in the generation of electricity from salinity gradients.

1.4An Introduction to an Outflow Electrochemical Cell

We're presenting a novel electrochemical cell design to tackle water scarcity, wastewater treatment, and green electricity generation. A notable innovation lies in the novel geometry that permits the inlet flow to expand outward across the porous electrodes. This design element effectively reduces the process's energy consumption by mitigating concentration polarization through advection. Concentration polarization stands out as a major driver of energy losses in electrochemical procedures.

This electrochemical cell utilizes symmetric porous Ag/AgCl electrodes. These electrodes can alternately capture and release Cl^- ions by forming or removing an AgCl coating. As the AgCl coating forms on the oxidation electrode, Cl^- ions are simultaneously removed from the reducing electrode. This redox reaction causes a variation in the solution concentration close to each electrode. The area near the oxidizing electrode experiences a reduction in the solution's content, while the region around the reducing electrode becomes more concentrated. This geometric approach can be applied to a system with porous electrodes of any type.

Chapter 2

Outflow Geometry for Electrochemical Desalination Cells

2.1Introduction

Expanding demand for freshwater is driving continued development of desalination methods. Reverse osmosis is the most popular current technology, due to low energy consumption and superior water quality [53,59,115–117]. However, desalination approaches using electric potential to drive separation, such as electrodialysis and capacitive deionization, are gaining interest for a variety of reasons including system simplicity, potential for energy efficient operation on less concentrated inlet streams, selectivity, and high recovery (particularly for ED) [28,118].

In electrodialysis and electrodialysis reversal, salt ions are removed via electromigration through selective ion-exchange membranes [26–28,119]. In capacitive deionization, salt is removed by applying a voltage between two capacitive electrodes both acting as sinks for the oppositely charged ion thus desalinating the solution [32–37]. The capacity limitation of capacitive electrodes can be alleviated by electrodes that use Faradaic reactions to form a "desalination battery" [38–41].

Like traditional batteries, desalination batteries can operate using various modes in terms of the participation of the ions in solution. In one implementation, one electrode removes cations from solution via a specific reaction during charging, while the other electrode removes anions. Another mode of operation is possible, resembling "rocking chair" or ion shuttling batteries, such as Li-ion. In this mode, one electrode sequesters ions while the other releases the same type of ion. Simultaneously, the counter ion migrates from the electrode acting as an ion sink to the one acting as a source to maintain charge neutrality. Smith and coworkers introduced this approach using symmetric electrodes both containing the same redox-active intercalation host compound (IHC) that absorbs cations in the bulk of the host lattice via a reduction reaction of species in the IHC [41,44,45]. The IHCs drive a process thus termed cation intercalation desalination (CID) where Na^+ is the active ion, which is stored/released by the electrodes. Since the electrodes are

undergoing the same electrochemical reaction, their equilibrium potential is similar, with the only difference arising from the local difference in solute concentration. The only energy consumed by the cell is due to the free energy of mixing and the various losses. A membrane is used to maintain separation of the concentrated and dilute solutions residing near the discharging and charging electrodes, respectively [120,121].

This ion shuttling mode is also applicable to anions. Bi/BiOCl was used in the first symmetric Cl^- ion desalination cell in which electrodes were separated by a cation-exchange membrane [43]. Ag/AgCl has also been used in Cl^- ion shuttling desalination by several research groups [122,123]. In a study by Yoon et al [122], implementing silver/silver chloride electrodes and a cation exchange membrane in a symmetric configuration, 80% salt removal from 500 mM NaCl solution was achieved. High salt adsorption capacity and fast desalination at low voltages were demonstrated. A similar system successfully separated chloride and nitrate based on the chloride selectivity of the electrodes (Selectivity of $Cl^-/NO3^-$ = 80) [124].

The Faradaic electrodes in ion-shuttling desalination batteries need not be symmetric. Different chemistries may be applied for the ion sink and source electrodes (as in traditional ion-shuttling storage batteries) resulting in a difference in the equilibrium electrode potentials and storage of energy during charging and release of energy on discharge. For example, an asymmetric configuration with two different Na-storage electrodes (Nickel hexacyanoferrate/Iron hexacyanoferrate) has been demonstrated [125].

2.1.1 Cell flow geometries

Electrochemical desalination systems can be used in batch mode, where the solution is stagnant in the cell, but generally operate with continuous flow of the inlet solution. Different flow geometries have been studied [126–131]. In the most common approach, feed water flows perpendicular to the electric field and along the plane of the electrodes, known as flow-by or flow between electrodes [32,118]. In this approach, significant depletion of electrolyte occurs near the electrode surfaces due to slow diffusion across the boundary layer, resulting in higher cell resistance and increased electrode potential due to local enhancement of depletion/enrichment. This affects the energy performance and

the throughput of the system [132]. Suss et al, introduced flow through electrodes, allowing flow parallel to the electric field [35,133,134]. Flow in this system is in the same direction through both electrodes with the inlet solution introduced at the outer surface of one electrode and effluent collected from the outer surface of the other. This geometry allows advection to aid in electrolyte replenishment at the electrode surfaces, reducing the effects of depletion at electrode surfaces, and flow through electrodes have faster cell charging compared to flow by electrodes [32]. However, the region between the electrodes in this geometry still experiences a significantly lower solute concentration, and higher solution resistance, than that of the inlet solution. This geometry is also only applicable to a mode of operation in which both electrodes are operating as ion sinks.

2.1.2 Novel outflow cell

Here we introduce an outflow geometry for electrochemical desalination. In contrast to previous work on symmetric electrochemical desalination cells, flow from the center of the cell outward through each of the porous electrodes distributes effluent with concentration different than the inlet to each output channel. The system is schematically shown in Figure 2-1. This flow geometry reduces concentration polarization effects and solution resistance losses and can therefore improve throughput and energy efficiency. Depletion and concentration polarization still occurs, but the magnitude of these effects is reduced and the length scale they operate over is dramatically reduced, moving from the volume between the electrodes to the pore volume within the electrodes.

Symmetric porous Ag/AgCl electrodes are employed, which alternatively sequester/expel Cl^- ions by accumulating/stripping an AgCl coating. Due to the electrode symmetry, the cell acts in an ion-shuttling mode. Switching of cell polarity results in regeneration of the coated electrode and coating of the stripped one by oxidation and reduction reactions, respectively. In parallel, the concentration of the solution near each electrode changes. The solution is depleted near the electrode being oxidized and enriched near the electrode being reduced. Charge neutrality in the solution requires concentrations of cations and anions to be the same at distances significantly larger than the Debye length. Cations are therefore diluted/enriched along with the Cl^- ions, resulting in a local decrease/increase of salt concentration with respect to the feed water. As the cell specifically acts on Cl^-, it is applicable to solutions that contain chloride ions.

The outflow geometry eliminates the need for a membrane in the ion-shuttling mode. This can simplify cell design and maintenance and lessen difficulties related to membrane fouling. However, the flow geometry presented is equally applicable to modes with both electrodes acting as ion sinks. Likewise, while several properties make silver an effective electrode for application here including high capacity, compatibility with the electrochemical stability of the solvent, reversibility, and robustness [135], the flow approach can be used with any porous electrode chemistry.

The remainder of the paper explores the behavior of a system using the outflow geometry over a range of operational parameters. We discuss the physical mechanisms affecting performance and consider potential benefits of the system with a particular emphasis on throughput.

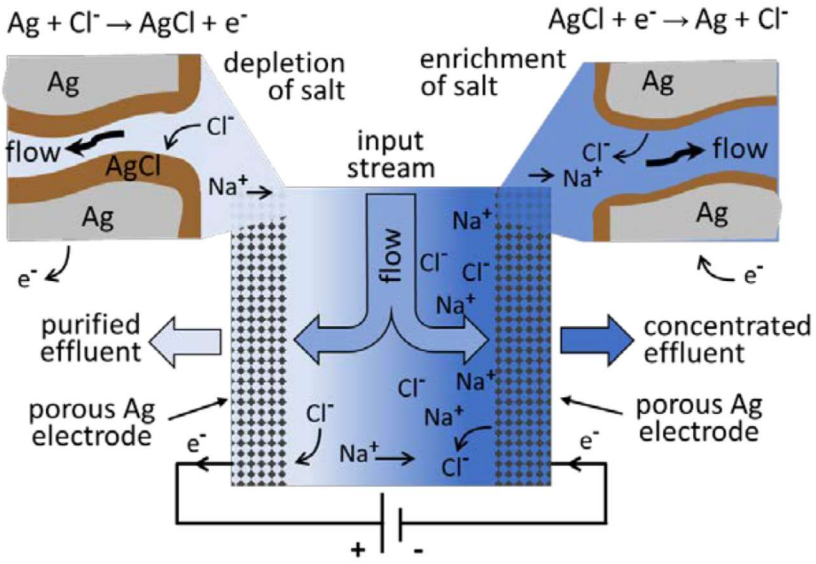

Figure 2-1: Schematic of Ag/AgCl electrochemical desalination cell with outflow through electrodes. Electrodes are alternatively corroded (left in figure) or reduced (right) producing purified or enriched outlet streams, respectively.

2.2Methods

The system introduced above is characterized here using analytical, computational, and experimental methods.

2.2.1 Mathematical models

We model the system behavior using the Nernst-Planck formalism with advection. The mathematical model is presented below including assumptions, governing equations, boundary conditions and methods for calculation of the potential across the system. The model is solved analytically for steady state conditions and numerically under transient conditions.

2.2.1.1 Assumptions and approximations

Assumptions and approximations used to simplify analysis of the model are detailed here. The cell is modeled in one dimension, along the direction of current

and fluid flow, and assumed uniform in the other two dimensions. This is a severe approximation, as the feedwater is introduced from one side of the stream as shown in Figure 2-1. The model allows essential insight into the cell operation, but we believe this approximation is a contributor to differences in modeled and experimental behavior.

Electrodes are considered as simple sources/sinks, and they are approximated as points in the 1D model, with negligible thickness. This is again a severe approximation as the actual electrodes are relatively thick compared to the domain between them. However, reactions likely do occur preferentially near the surfaces of the electrodes facing each other. The specific distribution depends on the internal surface area of the electrode, electrode resistivity, the local resistance for the reaction at the surface considered, and the operational conditions of the cell including current density, feed concentration, and flow rate [136]. In the extreme case of small resistance except for the solution contribution, the reaction would be limited to a narrow band. This is relatively well represented by the point model invoked here, although the position of the equivalent point electrode would shift as the reaction proceeds. Effects of this approximation are also considered later.

The electrolyte is approximated as symmetric, with the mobilities and diffusivities for the anion and the cation taken to be the same. Furthermore, electrolyte diffusivity and molar conductivity are considered independent of concentration. The concentration of NaCl in the cell is continuously changing in time and space, which affects the true diffusivity and molar conductivity values. However, due to the relatively small concentrations treated here, we consider constant values reasonable.

For model simplicity, activation and AgCl layer resistance at the electrode are considered negligible for AgCl thicknesses of interest. The only contributions to cell voltage considered are the equilibrium electrode potentials with respect to the local environment and solution resistance. This approximation relies on the large surface area of the porous electrodes. The components of resistance for Ag/AgCl electrodes have been well characterized by Ha, and Payer [137] and are discussed in supplementary materials. We note that the simplifications in resistance applied suggest uniform distribution of current across the internal electrode surface, which may not be maintained, as

mentioned above and discussed below. The activation and AgCl resistances may have significant effects, particularly in current distribution throughout the volume of the electrode. The resistance of the silver electrode material itself is also considered negligible.

Finally, the electrode capacitance corresponding to double layers at the surfaces is neglected, since the volumetric capacity of the electrodes is large compared to the surface area.

2.2.1.2 Governing equation

The transport equation used to model this system, eq. (2.1), is derived from the general mass conservation law for a solute dissolved in a flowing solvent with a net volumetric source or sink [138,139].

$$\frac{\partial C}{\partial t} = -\nabla \cdot \vec{J} + Source/-Sink = -D\frac{d^2C}{dx^2} + \frac{u}{\phi_m}\frac{dC}{dx} + \frac{i}{2F\phi_m\delta_{elec}} \tag{2.1}$$

where J is the molar flux for the species whose concentration is C. The source/sink term represents the creation or destruction rate of species throughout the porous electrode volume (with thickness δ_{elec}) due to chemical reactions. The strength of the source/sink is scaled by the transference number of the active ion, which for the symmetric electrolyte approximation applied, is taken as 0.5. i is current density (A/m^2), F (C/mol) is Faraday's constant, and D (m^2/s) is the diffusivity coefficient. Electroneutrality, along with the approximation of a symmetric electrolyte allows us to consider a single concentration value and eliminate the migration term here [139]. Real solutions will include a mixture of cations and anions for which electromigration must be considered. In this case, the conservation of each species and total charge conservation must be considered simultaneously to obtain solution potential and concentration distributions for each species [140–143].

In experimental implementations, a mesh with porosity, ϕ_m, is placed between the electrodes. Some of the cross-sectional area is thus unavailable for flow. This results in a higher local velocity and affects the strength of the sink/source.

To solve eq. (2.1), we break the solution domain into two regions (Figure 2-2). One region is from the introduction of the flow (center of the cell) to the source/sink, and the other segment is from the source/sink to the outlet. Due to the symmetry of the system, the solution for $\Delta C = C - C_0$ is antisymmetric about the inlet.

2.2.1.2.1 Boundary conditions

Four boundary conditions (BC) are applied to solve eq. (2.1) for both regions simultaneously (Figure 2-2). At the inlet (cell center), the concentration is fixed to the feed concentration (BC. 1), while at the outlets, the gradient of the concentration is zero (BC. 2). At the surfaces between the regions, representing the electrodes, the difference between the fluxes on either side of the electrode is equal to the total strength of the source/sink (BC. 3) (i.e., current over Faraday's constant). Lastly, the concentration is continuous across the electrodes (between the two regions) (BC. 4).

BC. 1 At $x = 0$, $C = C_0$

BC. 2 At $x = \pm\frac{L}{2}$, $\frac{dC}{dx} = 0$

BC. 3 At $x = \pm s$, $J_{out} - J_{in} = \frac{i}{2\emptyset_m F}$

BC. 4 At $x = \pm s$, $C^+ = C^-$

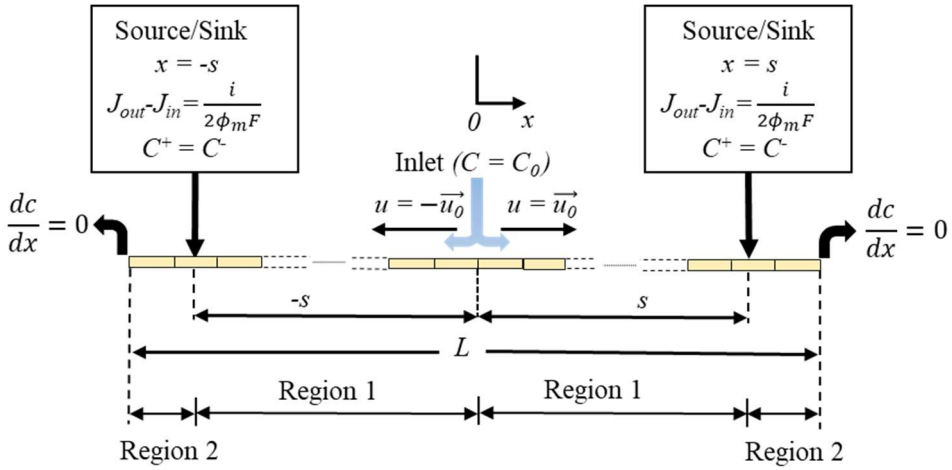

Figure 2-2: Schematic of model domains and boundary conditions

2.2.1.2.2 Model for potential in the system

As stated in 2.2.1.1, the activation and AgCl layer resistance are considered negligible. The total potential across the cell, V, is thus defined in terms of the local equilibrium electrode potential, E_{cell}, and the solution resistance loss, $i * ASR$, which obeys Ohm's law. The cell potential is thus calculated by eq. (2.2). ASR(Ω cm^2) is the cell resistance normalized by its area.

$$V = E_{cell} + i * ASR \tag{2.2}$$

Silver chloride and silver are insoluble and have activity of 1. Therefore, the equilibrium electrode potential is determined by the localized increase or decrease in the chloride concentration at the electrode surface compared to the bulk. E_{cell} is the difference in the equilibrium electrode potential due to the concentration difference between the two symmetric electrodes and is calculated by the Nernst equation, eq. (2.3) [137], where R (J mol^{-1} K^{-1}) is universal gas constant and T (K) is temperature.

$$E_{cell} = \frac{RT}{nF} ln \frac{[Cl^-_{Red}]}{[Cl^-_{Ox}]} \quad (2.3)$$

Solution resistivity is integrated between the electrodes to give total area specific resistance of the cell, as given by eq. (2.4), where Λ is molar conductivity (e.g. S m^2/mol) and ϕ_m is the mesh porosity.

$$ASR = \int \frac{dx}{\Lambda \phi_m C} \quad (2.4)$$

2.2.1.3 Numerical simulation

Eq. (2.1) is readily solvable analytically for steady state conditions, but numerical simulations are useful to understand transient behavior, describing where ions and energy are transferred inside the system for different operating conditions. The Fipy finite volume package in Python [144] is used for this purpose here. An implicit diffusion formulation is used for system stability. The sample domain is divided into 200 elements, and the time step is constant at 4.7 ms. Electrodes are considered as internal sources occupying a single element. Simulations are performed with square wave current or voltage imposed on the cell. For simulations with imposed voltage, the cell resistance is determined from the concentration profile from previous timestep and is used to determine the cell current for the following timestep based on the applied voltage. The cell current then provides the strength of the source/sink corresponding to the electrochemical reaction. More generalized approaches for potentiostatic and galvanostatic simulation are available [145].

2.2.1.4 Solution properties

The diffusion coefficient of the mixture of ions is obtained from eq. (2.5) [146]. D_1 and D_2 are the diffusion coefficients for Na^+ and Cl^- with the values of 1.334*10^{-9} m^2/s and 2.032*10^{-9} m^2/s, respectively [146].

$$D = \frac{2}{\frac{1}{D_1} + \frac{1}{D_2}} \tag{2.5}$$

Molar conductivities of NaCl taken from Lide [146]. The value of molar conductivity for NaCl at 50 mM of $111.01 \times 10^{-4} m^2\ S\ mol^{-1}$ is used for all calculations.

2.2.2 Experimental

2.2.2.1 Cell construction

The cell is constructed with a layered structure as shown schematically in Figure 2-3. The electrodes are separated from each other by a woven polymer mesh. The aperture of the cell (1 cm^2) is defined by silicone and polyester sheets, and all layers of the cell are sandwiched between acrylic caps.

The feed stream enters from the center and flows out through the porous electrodes. Syringe pumps on the inlet and both outlet ports are used to provide an even split of the flow. Dead volume is minimized in cell construction and throughout the flow circuit, which is important to minimize mixing. A schematic of the full experimental setup and photos of component layers are given in supplementary materials.

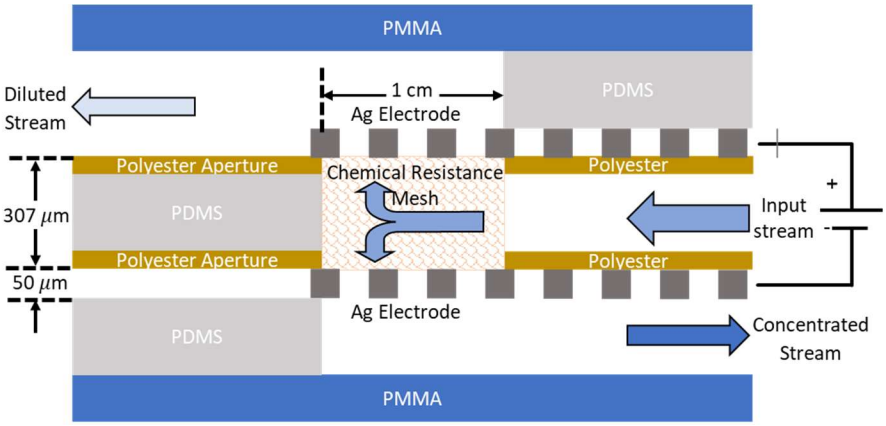

Figure 2-3: Schematic of cell layers

2.2.2.2 Cell materials

The cell electrodes are silver filtration membranes (Sterlitech) with nominal pore size of 0.2 μm and thickness of 50 μm. The porosity of the electrodes is measured to be 23%. For the 1 cm^2 of aperture area, the electrode working surface area is estimated to be 750 cm^2 based on a crude geometrical model described in supplementary materials. All layers of the cell are shown in Figure 2-3 and described in supplementary materials. The space between the electrodes is estimated to have thickness 307 μm with porosity 71%.

2.2.2.3 Conductivity measurement

Two types of conductivity probes are used to characterize effluents of the cell. A flow through conductivity electrode (ET916, eDAQ) with an internal volume of 17 µL is connected to one outlet while a contactless conductivity detector (eDAQ ER825 C4D) is used for the other.

2.2.2.4 Desalination experimental procedure

Before desalination (diluting and enriching cycles), one of the silver membranes must be chlorided (oxidized). The chloriding process was done at constant voltage of 0.9 V using flowing 50 mM sodium chloride (NaCl) solution. During the chloriding, 4 C of charge is stored in the electrode. The

corresponding volume added by silver to silver chloride conversion is about 15% of the pore volume. The amount of initial charge limits the later functioning, as availability of charge to shuttle between the electrodes determines cycle desalination capacity.

During desalination, 50 mM NaCl solution is introduced at the inlet to the system via syringe pump at flowrates between 40-800 µl/min. The cell is flushed with feed solution for 1000 s before operation. Voltage magnitudes of 0.18 V, 0.25 V, and 0.32 V are applied to the cell. Syringe pumps on both cell outlets withdraw depleted and enriched water at equal flowrates. Eventually, there is depletion of the AgCl layer on the reducing electrode. At this point the cell current drops, as further reduction is prevented, and the electrode polarity must be reversed for continued operation. This polarity reversal is triggered once the current drops to 0.3 of the average current for the first 300 s of the half cycle.

2.2.2.5 Experimental data analysis

Conductivity measurements are converted to concentration based on the molar conductivity. Conductivity data was rescaled based on the average of the conductivity values for 50 mM NaCl solution at the beginning and end of every experiment due to the changes of conductivity with temperature during the day. Occasional spurious conductivity readings were removed manually.

2.3 Results and Discussion

2.3.1 Steady state behavior from analytical model

Although the system relies on oscillation of current direction for continuous operation, steady state analysis is still useful for understanding important elements of system performance. Solving eq. (2.1), yields the well-known steady state concentration profile in terms of Peclet number (*Pe*). *Pe* represents the ratio of advection to diffusion in the cell and is expressed by eq. (2.6), where the characteristic length, is chosen as the distance from the center of the cell to the surface of the electrode, *s*.

$$Pe = \frac{su}{D} \tag{2.6}$$

The concentration profile as a function of position from the inlet to the electrodes is given by eq. (2.7), while the concentration from the electrodes to the outlets is uniform and expressed by eq.(2.8).

Between electrodes

$$\begin{aligned} C(x) &= C_0 \pm \frac{i}{2FPe\dfrac{D}{s}e^{\frac{Pe}{\phi_m}}}\left(1 - e^{\frac{Pe}{\phi_m s}x}\right) \\ &= C_0 \pm \frac{i}{2Fue^{\frac{su}{\phi_m D}}}\left(1 - e^{\frac{u}{\phi_m D}x}\right) \end{aligned} \tag{2.7}$$

Outlets

$$\begin{aligned} C(x = \pm s) &= C_0 \pm \frac{i}{2FPe\dfrac{D}{s}}\left(\frac{1}{e^{\frac{Pe}{\phi_m}}} - 1\right) \\ &= C_0 \pm \frac{i}{2Fu}\left(\frac{1}{e^{\frac{su}{\phi_m D}}} - 1\right) \end{aligned} \tag{2.8}$$

$$\Delta C = C(x = \pm s) - C_0 = \pm\frac{i}{2Fu}\left(\frac{1}{e^{\frac{su}{\phi_m D}}} - 1\right)$$

Eq. (2.8) gives the separation performance of the cell. Change in concentration from inlet to outlet, ΔC, is proportional to cell current and inversely proportional to velocity times a term accounting for diffusive remixing. The relationship between $\frac{\Delta C}{i}$ and Pe is shown in Figure 2-4. Higher velocity results in lower mixing as advection overcomes diffusion, carrying away the enriched and depleted solution at the electrodes.

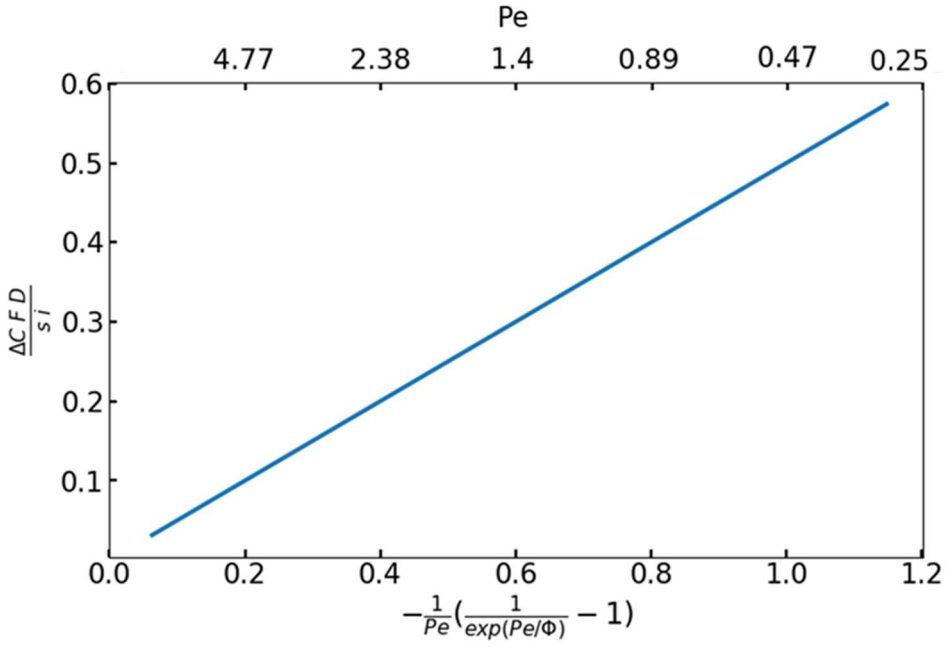

Figure 2-4: Relationship between $\frac{\Delta C}{i}$ and velocity showing competition of advection and diffusion. (Top axis corresponds to porosity of 0.7.)

Cell voltage (eq. (2.2)) can be determined entirely from the concentration profile (eq. (2.7)) and the operating current of the cell. As discussed in 2.2.1.1, solution resistance is the only significant component. Combining eqs. (2.4), and (2.7) yields an expression for the total cell area specific resistance, at steady state:

$$ASR = \frac{D}{\Lambda}\left[\frac{1}{M_1 u_1} ln \frac{C_0 e^{\frac{u_1 s_1}{\phi_m D}}}{C(s_1)} + \frac{1}{M_2 u_2} ln \frac{C(s_2)}{C_0 e^{\frac{u_2 s_2}{\phi_m D}}}\right] \quad (2.9)$$

$u_1 = u$ $\qquad$ $u_2 = -u$

$s_1 = s$ $\qquad$ $s_2 = -s$

$$M_1 = \mathrm{C}_0 - \frac{i}{2Fue^{\frac{us}{\phi_m D}}} \qquad M_2 = \mathrm{C}_0 + \frac{i}{2Fue^{\frac{us}{\phi_m D}}}$$

Cell voltage depends on solute molar conductivity, inlet concentration (C_0), relative concentration change ($\Delta C/C_0$), which we will refer to as degree of separation, and velocity (u). Implications for cell performance in terms of effectiveness of separation based on current flow (charge efficiency) and energy efficiency are discussed below.

2.3.2 Transient simulations

Simulations were performed with both constant current density magnitude of 48 A/m^2 (but alternating direction) and constant cell voltage magnitude of 0.18 V (but alternating polarity) to explore the spatial and time variations of the system characteristics. For all simulations shown here, the following conditions are maintained. The porosity of the space between the electrodes is set to 0.7. The velocity at each electrode is 3.33 μm/s. This corresponds to *Pe* = 0.32, and diffusion is stronger than advection in the region between the electrodes. The inlet feed solution is 50 mM NaCl.

Simulated changes of concentration versus position throughout the cell at various times in the cycle are shown in Figure 2-5 for constant current

magnitude. There is reduction (enrichment) occurring on the left electrode and oxidation (depletion) occurring on the right electrode. The plot shows the evolution of concentration following a polarity switch at 52.23 s. Prior to the switch, the system is at steady state with the left electrode being reduced (Cl^- source) and the right electrode oxidizing (Cl^- sink). At switching, the right electrode, for example changes from a sink to a source and creates a maxima in concentration that diffuses away from the source until a steady state is restored. The discontinuity in the slope at the electrode results from the addition/removal of electrolyte corresponding to the electrochemical reactions.

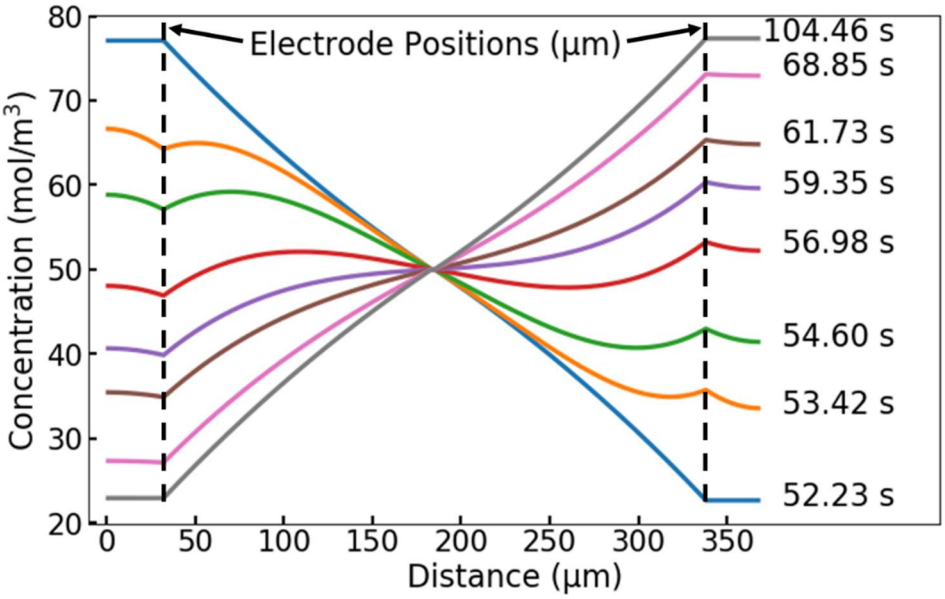

Figure 2-5: Simulated evolution of concentration vs distance for different times following application of step change in current direction (48 A/m^2 magnitude) at 52.23 s (as shown below).

The corresponding cell current and voltage and the concentrations for both diluted and enriched outlets are shown versus time in Figure 2-6.

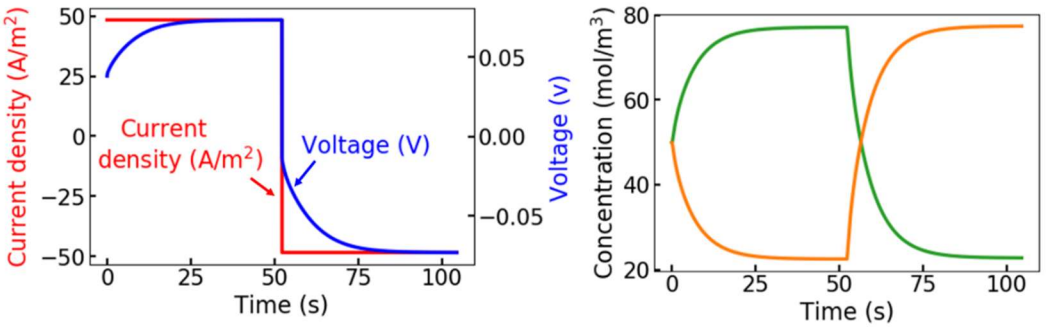

a.) b.)

Figure 2-6: Simulated cell behavior at constant current density (48 A/m^2) a.) Cell current and voltage vs. time b.) Outlet concentrations vs time

At a constant current density of 48 A/m^2, the voltage attains a steady state value of about 74 mV. Once the polarity is flipped, the voltage magnitude decreases and then recovers. After the switch of polarity (at 52.23 s in Figure 2-6), the magnitude of the cell voltage reduces rapidly to ~0.1 mV, then converges back to the steady state value in about 50 s. To physically explain this behavior, we refer to eq. (2.2). At the time of switching, the concentration cannot change instantaneously anywhere, so the equilibrium potential value remains the same. Likewise, the solution resistance which depends on concentration remains unchanged from before the polarity switch. The only change is the direction of the current. Thus, the resistive term changes sign, resulting in a lower voltage magnitude.

Figure 2-6-b shows the simulated change in concentration of the effluents, following changes in polarity. The simulation starts with an oxidation reaction on the electrode corresponding to the orange series producing dilute solution with a concentration of 23 mM. Reduction occurs on the green series electrode, producing solution enriched to 77 mM. As the polarity is flipped at t = 52.23 s, the electrode functions are reversed. The time for recovery to steady state in concentration corresponds closely to the transient in cell voltage and is about 40 s.

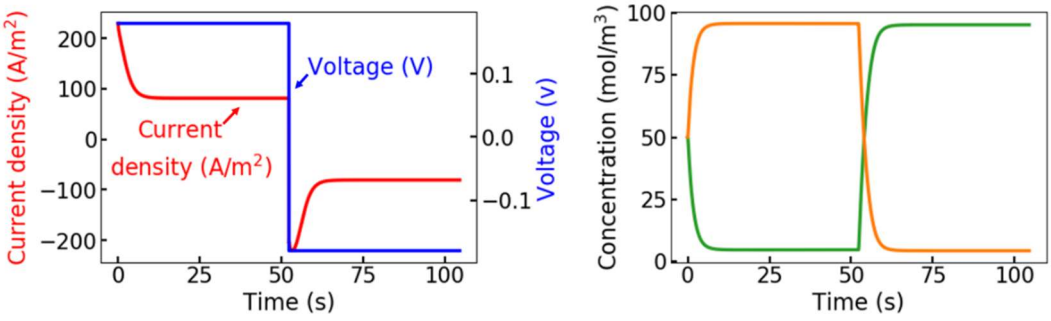

a.) b.)

Figure 2-7: Simulated cell behavior at constant voltage magnitude a.) Current and Voltage vs. time. b.) Outlet concentration vs. time

Operation at fixed cell voltage magnitude results in different behavior as shown in Figure 2-7. When applying a constant voltage magnitude of 0.18 V (with varying polarity), the current density reaches a steady state of 80 A/m^2 in about 5 s. The changes in effluent concentrations with time are shown in Figure 2-7-b. On the enriched side, the effluent concentration is 96 mM, and on the diluted side, the concentration reaches 4 mM. The transients in electrical and concentration are much shorter for the constant voltage magnitude compared to the fixed current magnitude case. The time from polarity switch to steady state in outlet concentration is about 8 s. The rapid concentration change is reflected by the high current density achieved during polarity switching.

The large spikes in current result from changes in voltage polarity. The simulation does not include an electric double layer, so this does not contribute to the simulated spike. Again, the physical mechanism for the spikes originates from the equilibrium potential of the electrodes. When the voltage flips, equilibrium electrode potential now enhances the flow of current resulting in very large values. As the concentration starts to deplete/enrich on the respective electrodes, the equilibrium potential returns to the original situation where it is fighting against the applied voltage. The large current after polarity switch quickly changes effluent concentrations.

2.3.3 Experiments

Desalination experiments use a 50 mM NaCl feed solution at a defined inlet flowrate from the center of the electrochemical cell and a constant voltage magnitude. Figure 2-8 shows the change in measured outlet solution conductivity and calculated concentration for a representative experiment with 12 cycles at an inlet flowrate of 40 μl/min (equal flowrate of 20 μl/min or velocity of 3.33 μm/s at each outlet, Pe = 0.32) and cell voltage of 0.18 V. On the enriched stream, the mean concentration value is about 76 mM, and on the dilute stream the mean concentration reaches 13 mM. The difference in concentration from inlet should be symmetric on both sides, but this is not observed. One possible reason for this difference is non-uniformity in the flow produced by compliance in the system (e.g., air bubbles) along with the change in flow resistance of the electrodes as they are corroded and stripped.

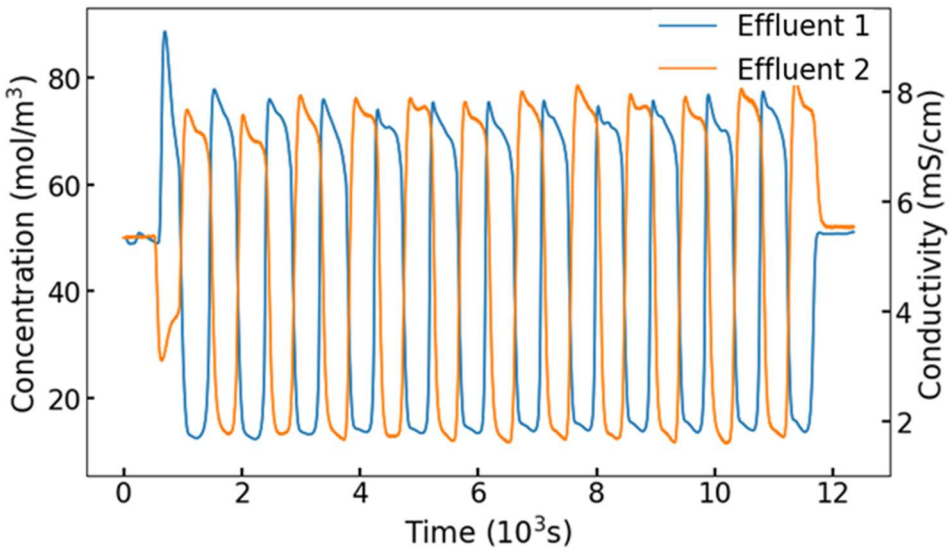

Figure 2-8: Measured outlet solution concentration for experiment with 50 mM NaCl inlet concentration and 0.18 V cell voltage magnitude.

Figure 2-9 shows the current density measured through the cell as a function of time for a voltage magnitude of 0.18 V (with alternating polarity). Each half cycle is about 400 s to 500 s long, and the length of cycle is set by the decay in current corresponding to the depletion of AgCl on one electrode, as discussed above. The average of the current density magnitude during each half cycle is

about 50 A/m^2. The experimental current is highest after switching, drops rapidly, then stabilizes somewhat before again decreasing at an accelerating rate and eventually reaching the cut off level (0.3 of initial average). We believe that the silver chloride available for reduction limits the charge capacity of the electrode.

However, the amount of charge moved back and forth between the electrodes is about 2.5 C for each half cycle (corresponding to ~3.6 mg of silver chloride). This is less than the initial charge of 4 C added in the chloriding process. We hypothesize that some of the corroded electrode may not be accessed based on the current cutoff criteria for switching. Additionally, the accumulating AgCl on the oxidizing electrode can impede further oxidation either by passivating the surface or clogging the pores. For uniform silver chloride growth over the entire surface, the layer resistance would be negligible, but the buildup may not be uniform. Some parts of the membrane may corrode faster and become clogged. Such a mechanism may invalidate our assumption of negligible AgCl layer resistance.

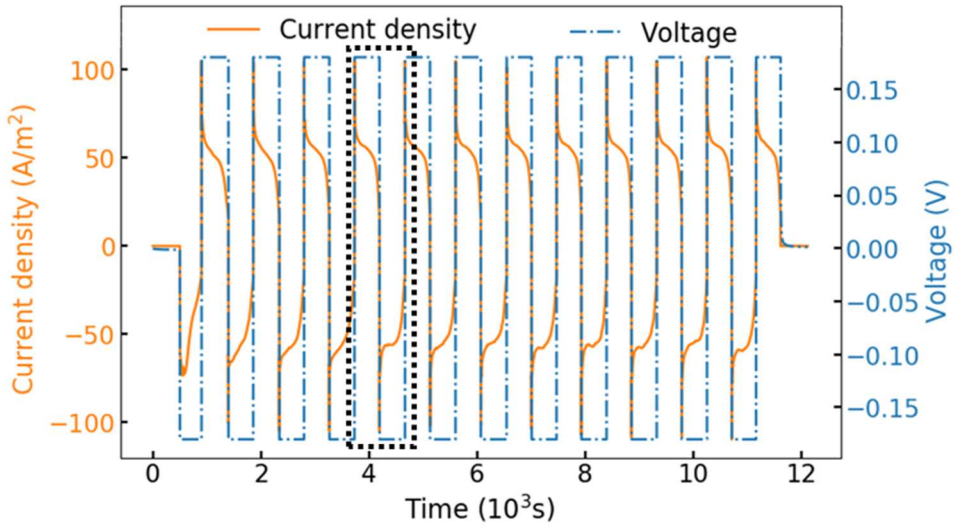

Figure 2-9: Measured cell current and voltage for experiment with constant cell voltage magnitude but alternating polarity. The outlined cycle is considered in detail below.

2.3.4 Comparison of experimental and simulation data at constant voltage

Experimental and simulation results at constant voltage magnitude and similar conditions are compared here, and differences in current and concentration response are discussed. The 8^{th} and 9^{th} half cycles from Figure 2-9 are expanded in Figure 2-10 along with the simulation data form Figure 2-7.

Each half cycle in the simulation is performed for about 52 seconds until the system approaches a steady state. However, the simulation has no inherent limitation on electrode capacity, and this is an arbitrary time for polarity switching. The experimental half cycle is longer, and the simulation data is therefore split and aligned with the experimental polarity switch in Figure 2-10.

At steady state, the current densities are quite similar for simulation and experiment. The initial current spikes in the experimental data are, however, of significantly smaller magnitude, and the experimental current time trace shows more complexity than simulations, with a slight rise and longer time scale decay following the initial spike. We hypothesize that the difference between the simulation and the experimental data results primarily from the 1-D nature of the simulation. In reality, the electrodes are certainly not uniformly active, and the flow does not evenly distribute across the electrode aperture. In the experiment, there is likely a concentration gradient across the electrodes between areas closer to and further from the inlet. Longer term relaxation processes associated with lateral concentration gradients may explain the slower current decay. The finite thickness of the electrodes in experiment may also contribute to the discrepancy with the simulated current spike.

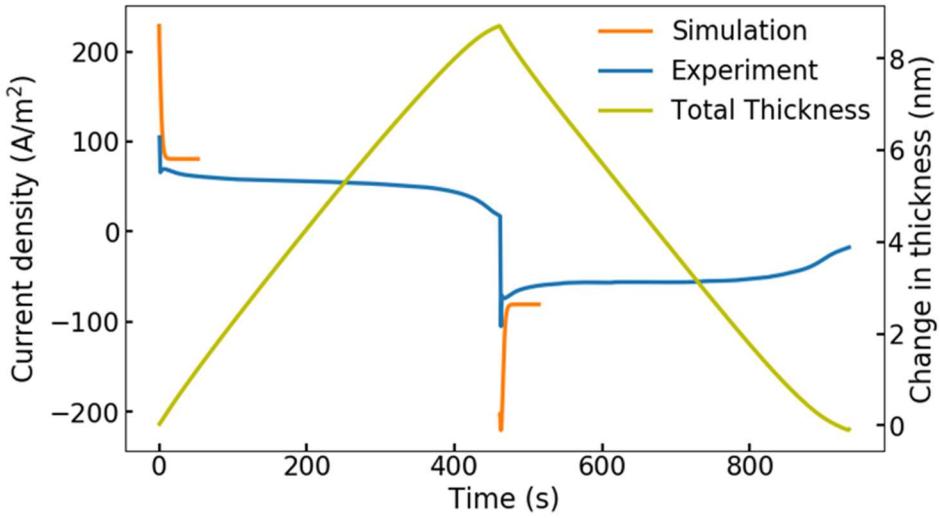

a.)

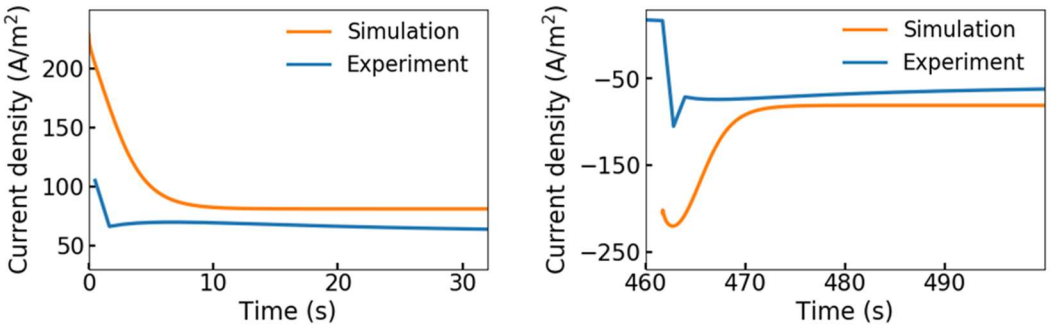

b.)

Figure 2-10: a.) Comparison of experimental and simulated current density and changes in the thickness of AgCl layer at constant voltage magnitude b.) Short time scale transients in current for experimental and simulation

Neglecting any electrochemical reaction other than silver oxidation and reduction, the current can be converted to AgCl volume accumulation on the oxidizing electrode for each cycle. Treating the AgCl volume as uniformly distributed over the electrode surface area yields an estimate for thickness. Based on the estimated electrode surface area (supplementary materials), the change in

thickness is about 9 nm, which is small compared to the nominal pore size of 200 nm. The accumulation of silver chloride, however, is undoubtedly non-uniform. Some pores may be filled, while others are still available. We note that the non-uniform reaction can have a self-regulating effect. As the corrosion layer thickness increases, the reaction will be preferentially shifted to less corroded areas. Likewise, localized depletion in volumes of the electrode will tend to shift current to less depleted volumes. A full consideration of these effects requires detailed 3D simulation of flow and electrochemical transport [147].

Figure 2-11 shows the changes in the effluent concentrations for both simulation and experiment. For the experimental results, the concentration has a 52% average increase on the enriching side and a 74% average decrease on the removal side (compared to the inlet concentration), though the concentration change would be expected to be symmetric. As discussed above, a possible reason for this difference is non-uniformity in the flow. In the simulation, the change in the concentration is 92% in both enriched and dilute streams, showing substantially more effective separation. Again, a likely important factor in this discrepancy is the assumption of 1-D flow. This is discussed in more detail with regard to charge efficiency below.

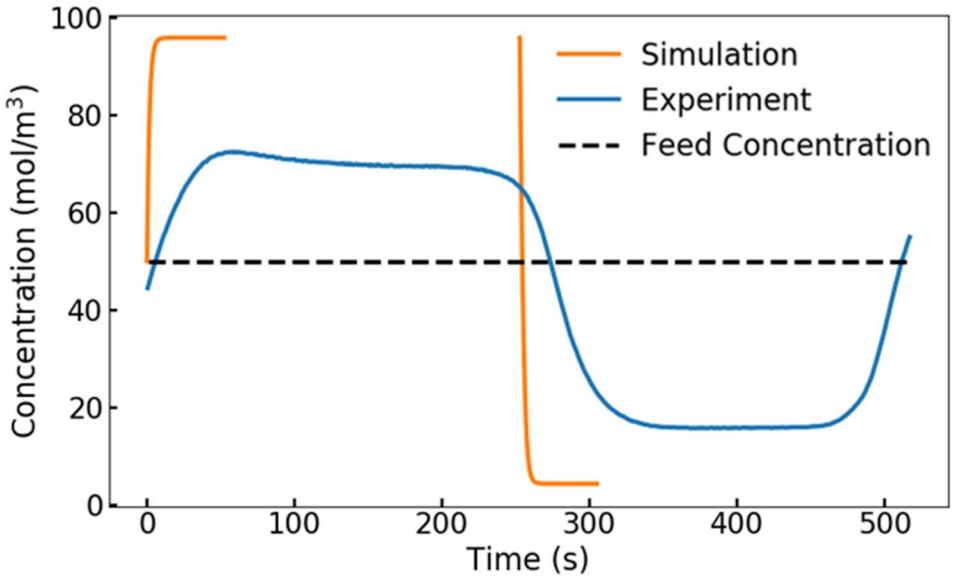

Figure 2-11: Comparison of the effluent concentrations for simulation and experiment for constant voltage magnitude of 0.18 V. Dashed line represents the inlet concentration.

2.3.5 Charge efficiency

Charge efficiency (η) is an important parameter describing the effectiveness of electrochemical desalination. It is defined by the number of salt ions removed from solution divided by the number of unit charges passed through the cell, as given by eq. (2.10) [32], in which ΔC is the difference between the outlet and inlet concentrations. In the system considered, solute ion removal occurs due to the capture of Cl^- ions during electrode oxidation and the corresponding conduction of Na^+ ions toward the opposite electrode. For this symmetric electrode case, the charge efficiency is scaled by the transference number of the active ion [44], 0.5 for the symmetric electrolyte approximation applied in the model

$$\eta = \frac{2u\Delta CF}{i} \tag{2.10}$$

The most important factor lowering charge efficiency is diffusion in the system, acting against the outward flow carrying the dilute and enriched streams away. Charge efficiency must be zero when no solution flows from the cell.

From the analytical solution for steady state outlet concentration, eq (2.8), ΔC is proportional to current density and inversely proportional to flow velocity. The charge efficiency at steady state then only depends on *Pe*.

$$\eta = \left(1 - \frac{1}{e^{\frac{Pe}{\Phi_m}}}\right) \tag{2.11}$$

Charge efficiency versus *Pe* for the steady state analytical model is shown in Figure 2-12. Since diffusivity is considered constant, *Pe* and η only depend on

velocity for a fixed electrode spacing. The yellow data points in Figure 2-12 show the experimentally measured charge efficiencies (using an average of outlet ΔC values).

The model shows good correspondence to the experimental data, but there are several effects not captured in the model which may influence charge efficiency. The analytical solution applies to steady state while the experiments include transient conditions. There is some loss of charge efficiency due to polarity switching, in which concentration gradients that were built up at the expense of passed charge are destroyed without being conveyed to the outlets. Complex flow may also affect transient response. The concentration response in experiment is indeed slower than the simulation. Taylor dispersion in the tubes leading to the conductivity probes and dispersion in the porous media may also contribute to the slower response in experiment. In application, the relative significance of the transient portion of the response would depend on the capacity of the electrode. For high-capacity electrodes, switching is infrequent, and the transient is relatively unimportant. The model is derived for a symmetric electrolyte, whereas Cl^- in the solutions considered here has a transference number closer to 0.6. The 1-D flow assumed in the model fails to account for the more complex 3-D flow likely produced in experiments, which allows for additional mixing and stagnation. The assumption of thin electrodes in the model may also affect calculated charge efficiency. This effect might be expected to lead to underestimation of charge efficiency by the model due to the closer effective electrode spacing.

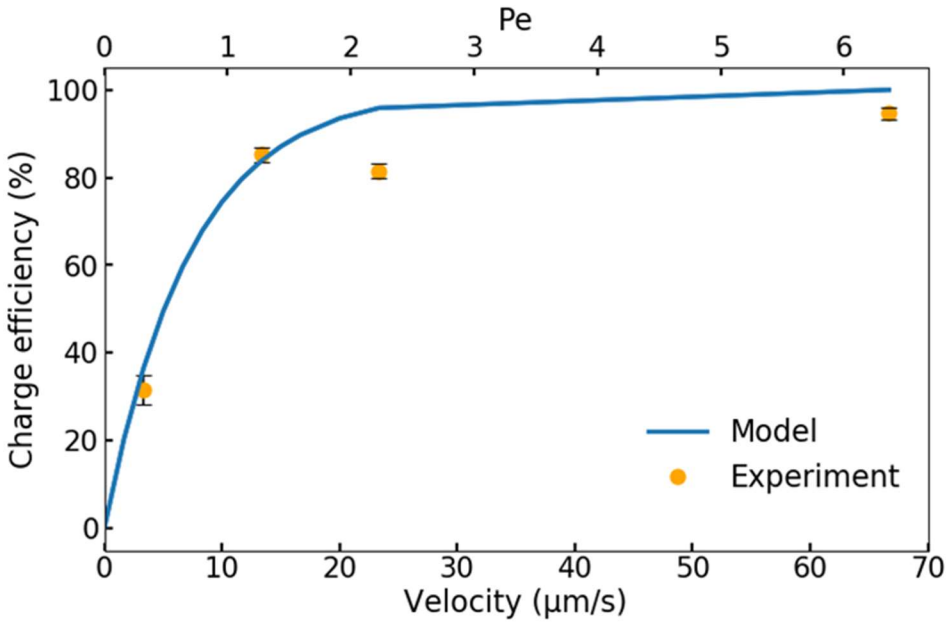

Figure 2-12: Charge efficiency vs velocity and equivalent *Pe* number. Blue, solid series corresponds to analytical solution at an electrode spacing of 307 μm. Yellow data points shows the experimentally measured efficiency.

Charge efficiency can be improved by a variety of approaches. As shown by eq. (2.11), charge efficiency depends on *Pe* which itself depends on the distance between electrodes. Therefore, at a constant velocity, by increasing the spacing between electrodes, the *Pe* would increase and result in a higher charge efficiency. Charge efficiency can also be improved by limiting the cell dead volume and minimizing mixing. As discussed, high capacity electrodes that minimize switching frequency improve charge efficiency.

2.3.6 Cell voltage

As shown in eqs. (2.2) (2.3), and (2.9), cell voltage increases with increasing degree of separation ($\Delta C/C_0$) and flow velocity. Figure 2-13 shows the required voltage for cells operating at different flow velocities while producing a desired change in concentration, ΔC, based on the steady state solution (eq. (2.9)), with inlet concentration C_0 = 50 mM.

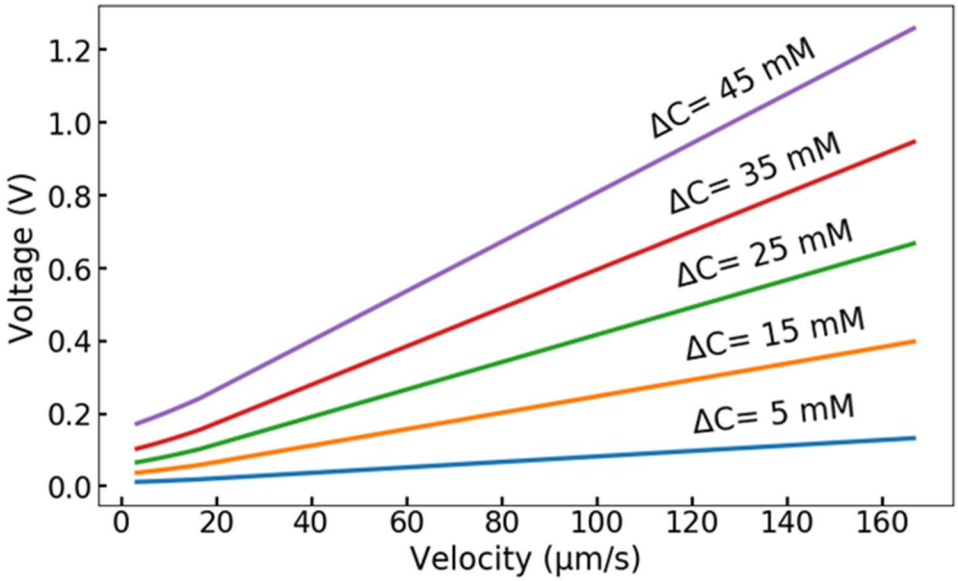

Figure 2-13: Cell voltage vs velocity at inlet concentration of 50 mM for different ΔC values as modeled analytically at steady state.

For a fixed cell voltage, the change in concentration achievable is thus limited by flowrate. Higher flowrate leads to better charge efficiency but lower desalination degree. Figure 2-14 shows the degree of separation, $\Delta C/C_o$, from 50 mM feed solution, predicted by the steady state analytical model versus velocity for two cell voltages and measured experimentally at a number of voltages and velocities.

The cell voltage behavior also depends on electrode spacing. (All results show here are for electrode spacing of 307 μm.) The assumption of thin electrodes in the model may underestimate the solution loss somewhat due to the additional average ionic conduction distance in the electrode pore space in experiments.

We note that the increase in voltage with flowrate at constant degree of separation is due entirely to the solution Ohmic loss. The equilibrium potential for each electrode is fixed for a given degree of separation. For all practical Cl^- concentrations and pH values, the equilibrium potentials for both electrodes are within the stability window for water [148]. Electrolyte stability is discussed in supplementary materials.

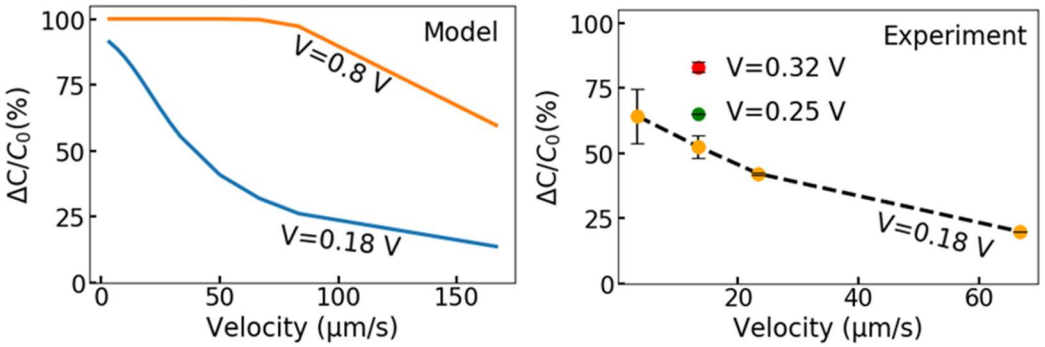

a.) b.)

Figure 2-14: Degree of separation ($\Delta C/C_0$) vs. velocity a.) calculated with analytical model and b.) measured experimentally (red: cell voltage of 0.32 V, green: cell voltage of 0.25 V, and yellow points with dashed line: cell voltage of 0.18 V).

2.3.7 Energy efficiency

We evaluate energy efficiency based on energy expended per ion separated from the inlet stream, expressed in eq. (2.12) in terms of cell operational parameters and charge efficiency.

$$\text{Energy per ion} = \frac{Cell\ Power}{Separation\ rate} = \frac{Vi}{u\Delta C} = \frac{VF}{\eta} \tag{2.12}$$

An important result from consideration of eqs. (2.8) and (2.9) is that the energy per ion is dependent on the relative degree of separation ($\Delta C/C_0$), feed concentration (C_0) and flow velocity (u) for the steady-state analytical model. Pumping power is not considered in eq. (2.12) or the following analyses. As discussed in the next section, its contributions to energy consumption are small compared to the de-mixing and Ohmic components.

As shown in Figure 2-15, the required energy to separate ions at very low flowrate is large, due to high back diffusion (lower *Pe*) and poor charge efficiency. By increasing the flowrate, advection overcomes the back diffusion (higher *Pe*) and the energy per ion decreases. However, as discussed above, higher velocity requires

higher cell voltage to drive the required current for a given degree of separation ($\Delta C/C_0$), thus increasing energy usage. The competition between these two effects (diffusion versus resistive loss) results in an optimum velocity for minimum energy usage, as seen in Figure 2-15. At higher flowrates, the throughput of the system improves at the expense of increased energy consumption.

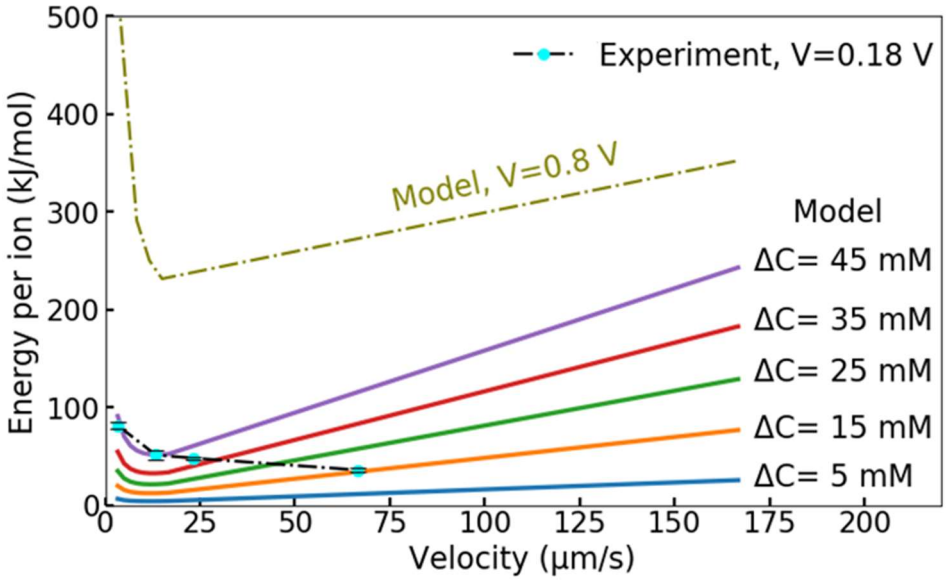

Figure 2-15: Changes in energy per ion vs velocity as a function of ΔC and cell voltage for C_0 = 50 mM calculated with analytical model and measured experimentally. Note that degree of separation in experiment varies with velocity for constant voltage and is smaller than predacity by the model (see Figure 2-14).

In Table 2-1, the energy per ion for similar degree of separation is compared for experiment and steady-state model solutions at two flowrates in this study, and for an RO system analysis from literature considering similar inlet concentration and blending for similar degree of separation [149]. From Figure 2-15, to achieve the lowest energy per ion at a 65% degree of separation, the flowrate should be 70 ml/min. Energy per ion for the experiment here is approximated 1.7x higher than that predicted from the steady state model. However, the predicted energy consumption for the 1D flow with optimized velocity (11.7 μm/s) is similar to the example reverse osmosis application with similar salt removal (applying permeate and input blending) reported in literature [149], and 16.5x the thermodynamic minimum [150].

Table 2-1: Comparison of energy per ion removed for similar ΔC and $C_0 \cong 50$ mM

Method	Superficial Velocity (μm/s)	$\Delta C/C_0$	Energy per ion (kJ/mol)
This study – Experiment	3.33	64.1%	81.43
This study - Steady state model	3.33	65%	48.91
This study - Steady state model, ideal velocity	11.67	65%	29.37
Reverse osmosis [149]	5.56*	65%**	27.27

* - effective velocity for blended output –

** - portion of input stream mixed with permeate to adjust salt removal

2.3.8 Throughput and scale-up

The outflow geometry reduces electrolyte depletion between the electrodes that exists in traditional flow-by geometries due to slow diffusion across the relatively large boundary layer. Flow from the center of the cell replenishes the electrolyte at the electrodes. This mechanism has two benefits. It reduces the solution resistance corresponding to large, heavily depleted regions, and it reduces the equilibrium potential of the electrodes by reducing concentration polarization. These effects have significant influence on cell throughput, allowing operation at high superficial velocities compared to competing technologies like RO. Due to both membrane

hydraulic resistance and concentration polarization, RO systems are commonly limited to low membrane permeate velocities. For example, an RO system tailored for brackish water is likely limited to permeate fluxes of less than 10 μm/s, even for high quality sources [151].

As shown in the previous section, for the outflow electrochemical system, above an optimum velocity, there is a tradeoff between increasing the throughput and the energy required for a fixed degree of separation. However, this is a gradual trade and high throughputs are possible at acceptable energy efficiencies. As an example, based on model predictions, removal of ΔC = 32.5 mM from inlet concentration C_0 = 50 mM at the optimum superficial velocity of 11.67 μm/s requires 29.37 kJ/mol of separated ions, but the flowrate can be increased 10x (116.67 μm/s) while increasing the energy only 4.1x (121.27 kJ/mol). RO membranes incur much larger increases in energy loss with increased permeate flux due to the high pressures required to drive flow. For example, a representative brackish water RO membrane might require ~1 bar of pressure per μm/s of superficial velocity increase [152].

We note that pumping power has been neglected in the previous analyses for the outflow electrochemical system. This is due to the relatively low hydrodynamic resistance of the electrode. The pore sizes of interest for the porous electrode (e.g., ~200 nm in the experimental cell) are dramatically larger than those relevant for traditional membrane approaches. Based on the simple geometrical model presented for the membrane in supplementary information (Figure S1), the hydrodynamic resistance of the electrode predicted from the Hagen- Poiseuille equation would be ~0.2 kPa/(μm/s), more than 100x smaller than the resistance of brackish water RO membranes considered above. The actual flow resistance will depend on the specific configuration of the porosity in the electrode and, importantly, whether any gas is trapped in the pores, as the relative permeability for multiphase flow can be dramatically lower than the intrinsic single phase value [153]. For these low values of hydraulic resistance, pumping power is small compared to Ohmic loss and de-mixing energy. For example, the hydraulic power for the electrochemical system at a velocity of ~100 μm/s would be ~4 W/m^2 for the predicted flow resistance compared to a modeled electrical power of ~400 W/m^2 for 70% removal from 50 mM NaCl feed. Furthermore, we note that larger electrode pore sizes (e.g., 1 μm) are viable and would dramatically reduce hydraulic resistance (proportional to

inverse of pore size squared) while not severely impacting internal surface area (proportional to inverse of pore size).

Given the gradual increase in energy consumption with cell throughput, other limitations of superficial velocity are of interest. As discussed above, oxidation and reduction of the electrodes is thermodynamically favored to electrolysis of water for all practical conditions. Therefore, throughput is not specifically limited by cell voltage. Although not expected to be a significant contribution to energy consumption, pressure drop still presents practical limitations. A primary advantage of the electrochemical desalination approaches is the system simplicity and freedom from high pressure components. High electrode pressure drop may reduce such an advantage. Perhaps the most essential constraint on throughput is polarity switching frequency. In a usable system, the effluent streams from each electrode must be redirected to different outlets to accommodate the change from depletion to enrichment. During the switch, depleted solution is lost both in the cell volume itself and any "dead" volume beyond the electrode which is alternatively occupied by dilute and enriched effluent. For fixed electrode capacity, switching frequency is proportional to throughput. At sufficiently high switching frequencies, losses associated with mixing will be significant, thus limiting throughput.

Practical desalination systems will require much larger electrodes that the 1 cm^2 considered in the current experiments. However, the flow of the feed solution within the plane of the electrodes prior to its flow through the electrodes themselves (Figure 1), puts severe limitations on the width that is practical for a single electrode. Scale-up of the system to larger sizes will require uniform distribution of feed solution through the electrodes. One solution to this challenge is to divide the electrode into a large number of smaller electrodes resulting in smaller aspect ratios for the active solution volumes. Implementing this solution will require a manifold capable of supplying feed solution to and extracting effluent from each of the individual electrodes. The design of these manifolds is a focus of ongoing work.

Finally, we consider the operation of the outflow electrochemical system with higher feed concentrations. The two primary effects of increase in feed concentration are an increase in polarity switching frequency and a reduction in solution resistance. As discussed above, switching frequency likely poses a primary limit on throughput. Therefore, increased inlet concentrations will likely require increased electrode capacity via thicker electrodes or reduced superficial velocity.

2.4 Conclusions

Here we introduce an electrochemical deionization system utilizing a novel outflow geometry. The system is analyzed using steady-state analytical and transient numerical models and characterized with experiments on a small (1 cm^2 active area) system. Cell behavior is studied in terms of cell electrical characteristics and separation action. Overall desalination performance is also characterized in terms of degree of separation, throughput, charge efficiency, and energy usage.

The advection imposed through the porous electrodes in the novel flow geometry, colinear with the motion of the ions, greatly alleviates electrolyte depletion that occurs in other electrochemical deionization approaches, which predominantly apply flow perpendicular to the motion of ions. The reduced depletion has significant effects for the system kinetics and energy consumption. Advection acts to lower the degree of concentration polarization at the electrodes and decreases the electrolyte resistance associated with depletion. These phenomena act to reduce energy loss at a given flow rate or conversely allow higher flowrate for a given energy consumption or cell voltage drop. This approach offers potential for superficial membrane velocities more than 20x those of RO (e.g., >100 μm/s for the outflow cell compared to ~5 μm/s for RO [154]). As the system introduced here also has no requirement to handle high pressure flow, it may offer a compact and convenient alternative for high efficiency desalination, for example, in mobile contexts. The selective nature of the Ag/AgCl electrodes applied here may also make the system beneficial for selective separations[124,155].

2.5Appendix

2.5.1 Electrode properties and behavior

The cell electrodes are formed from porous silver filtration membranes (Sterlitech) with a nominal pore size of 0.2 µm. Relevant characteristics of the electrodes are discussed below.

2.5.1.1 Ag/AgCl electrode resistance components

The accumulation of charge considered in this study corresponds to a small thickness of AgCl on the porous electrode surface. Likewise, the current density at the electrode surface (assuming uniform distribution throughout the porous structure) is very low, minimizing the contribution of activation resistance. Based on linear interpolation of results from Ha and Payer [137], the resulting area specific resistance (*ASR*) for these two components is negligible compared to solution resistance. For example, the solution resistance for the cell design and operational parameters considered here is ~10^6 times larger than the maximum uniform silver chloride layer resistance. Likewise, at the maximum pore surface current density considered here, the activation overpotential is only about 1-2 mV which is less than 1% of the total potential drop in the system. However, non-uniform reaction rates throughout the electrode may hinder the validity of this approximation. The resistance of the silver matrix is also considered negligible.

2.5.1.2 Electrode porosity

Electrode porosity was determined from measurement of sample mass and thickness for membranes of defined area. Table 2-2 provides information for membranes used in experiments.

Table 2-2: Specifications of 0.2 μm silver filtration membranes (Sterlitech).

Thickness (μm)	Area (cm^2)	Mass (g)	Membrane density (g/cm^3)	Areal density (g/cm^2)	Silver density (g/cm^3)	Solid fraction	Porosity
40	10.75	0.3502	8.14	0.814	10.49	0.77	23%

2.5.1.3 Membrane microstructure model

The surface area of the electrodes is approximated by a simple geometric model as shown in the Figure 2-16. The silver membrane is modeled as a sheet with cylindrical holes through it having diameter equal to the nominal pore size of 0.2 μm and length equal to the membrane thickness of 50 μm. The measured membrane porosity is ~23%. Using the above geometric model, the ratio of the total surface area (A_{surf}) to the projected area (A_{proj}) is approximately 260.

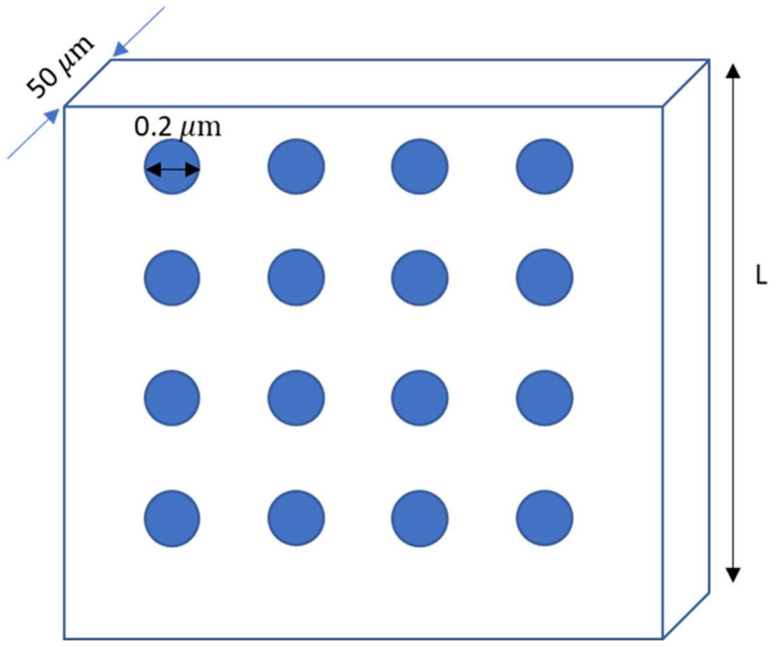

Figure 2-16: Membrane microstructure model

2.5.1.4 Electrolyte stability relative to electrode.

A key characteristic of the electrode is its potential with respect to reactions involving the solvent. The equilibrium potential for electrode reaction ($Ag + Cl^- \rightarrow AgCl + e^-$) depends on the concentration of chloride in solution. Likewise, the evolution of hydrogen or oxygen gas by electrolysis, depends on the pH of the solution. However, for all reasonable values of chloride concentration and pH, the electrode potential remains in the stability window of water [148]. A Pourbaix diagram for silver in the presence of Cl^- is shown in Figure 2-17 for some example values of chloride concentration.

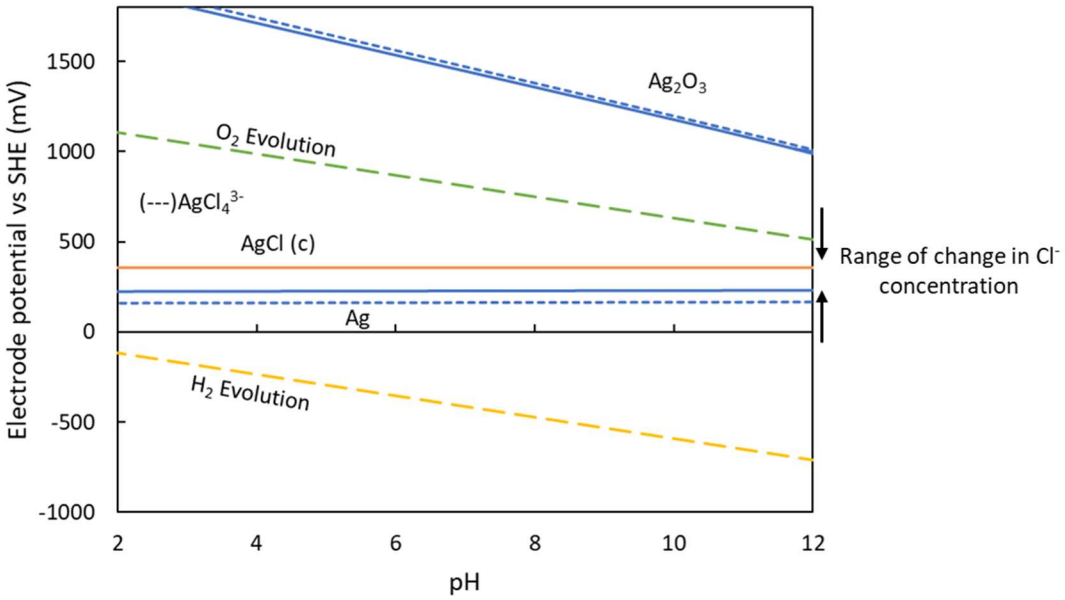

Figure 2-17: Pourbaix diagram for an Ag-Cl-H_2O system at 25°C for blue solid line Ccl^- = 1 M, blue dashed line Ccl^- = 2 M, orange solid line Ccl^- = 5 mM

2.5.2 Detailed cell construction

Figure 2-18 shows an exploded schematic of the desalination cell construction. NaCl solution is introduced by using a syringe pump to the center of the cell. Depleted and enriched water outlets are collected at a flowrate equal to half the inlet flow by syringe pumps. Conductivity probes are used to measure the conductivity of two effluents of the cell.

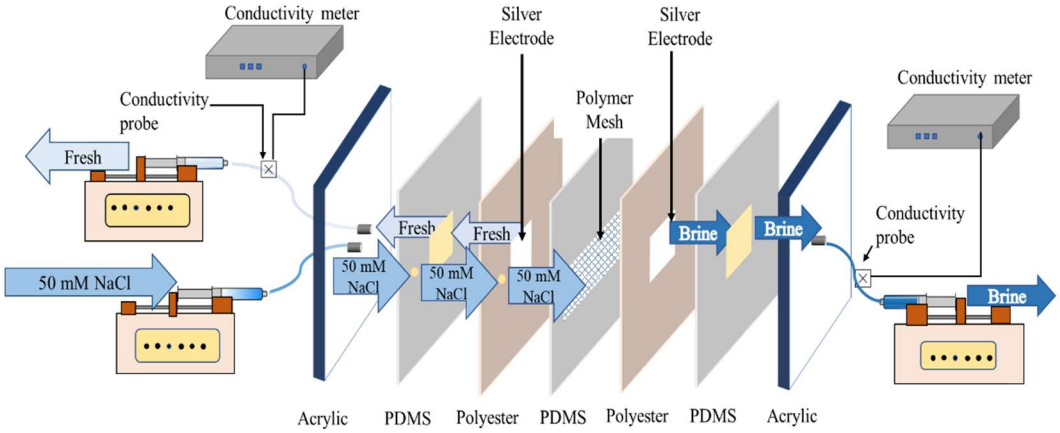

Figure 2-18: Exploded cell schematic.

Figure 2-19 shows a photograph of the cell's component layers. The electrodes are 200 nm membranes with a thickness of 50 μm and active projected area of 1 cm^2. They are separated from each other by a woven polymer mesh. The initial thickness of the mesh separating the electrodes is 322 μm. Due to the compressibility of the mesh, the final thickness of the mesh in the assembled cell is considered to be 307 μm (based on the sum of supporting layers) in both the simulation and the analytical models. The porosity of the mesh is measured based on areal density and thickness as approximately 71%. Silicone and polyester sheets are used to define the cell aperture and finally acrylic caps are used to sandwich all the layers and provide support. The active volume of the cell is defined by the PDMS and polyester layers. PDMS gasket thickness is 0.259 mm, and the polyester sheet thickness is 0.024 mm. Acrylic caps are used to sandwich different layers of the cell and provide robust construction. A laser cutter was used to pattern different layers of the cell.

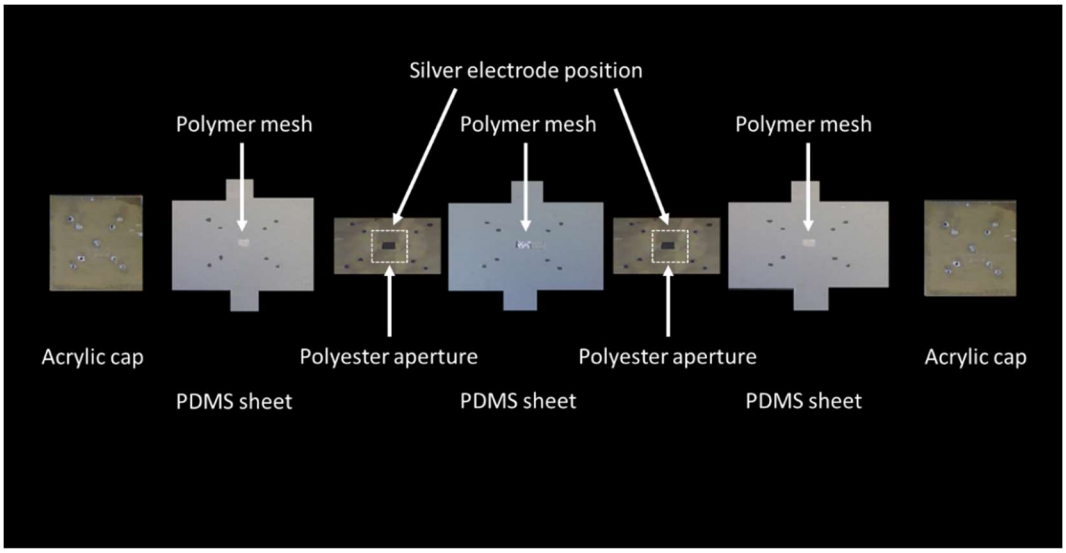

Figure 2-19: Photograph of component layers

2.5.3 Analytical solution

The comprehensive derivation of the analytical solution is presented here.

$$\frac{\partial C}{\partial t} = -\nabla \cdot \vec{J} + Source/-Sink = -D\frac{d^2C}{dx^2} + \frac{u}{\phi_m}\frac{dC}{dx} + \frac{i}{2F\phi_m\delta_{elec}}$$

Boundary conditions:

1. At the inlet (cell center), the concentration is fixed to the feed concentration (BC 1)

   BC. 1 At $x = 0$, $C = C_0$

2. At the outlets, the gradient of the concentration is zero (BC. 2)

   BC. 2 At $x = \pm\frac{L}{2}, \frac{dC}{dx} = 0$

3. At the surfaces between the regions, representing the electrodes, the difference between the fluxes on either side of the electrode is equal to the total strength of the source/sink (BC. 3) (i.e., current over Faraday's constant).

BC. 3 At $x = \pm s$, $J_{out} - J_{in} = \frac{i}{2\emptyset_m F}$

4. The concentration is continuous across the electrodes (between the two regions) (Continuity equation) (BC. 4).

BC. 4 At $x = \pm s$, $C^+ = C^-$

The ODE

$$ay'' + by' + cy = 0$$

where a, b, c are constants (with $a \neq 0$) always has a solution of the following form:

$$y = e^{\lambda t}$$

where λ is a constant (which may be real or complex), to be determined. Making this substitution in the ODE, it is found that λ must satisfy the auxiliary equation $a\lambda^2 + b\lambda + c = 0$

The real solution for this equation is:

$$y = Ae^{\lambda_1 x} + Be^{\lambda_2 x}$$

At sink/source =0

$$D\lambda^2 - \frac{u}{\emptyset}\lambda = 0 \rightarrow \lambda_{1,2} = \frac{-b \pm \sqrt{b^2 - 4ac}}{2a}$$

From the equation, $c = 0$

$$\lambda_1 = -b + b = 0$$

$$\lambda_2 = \frac{-b}{a} = \frac{u}{\emptyset D}$$

The concentration profile would be:

$$C = Ae^{\lambda_1 x} + Be^{\lambda_2 x}$$

By substituting λ_1 and λ_2, the concentration profile would be:

$$C = A + Be^{\frac{u}{\emptyset D}x}$$

Now we need to apply the boundary conditions to the concentration profile:

Domain 1:

Applying the BC 1:

$$at\ x = 0, C = C_0$$

$$C_0 = A + B \rightarrow A = C_0 - B \qquad *$$

Applying the BC 3:

$$at\ x = x_s^-, J_{out} - J_{in} = S_{sink}$$

$$\left[\frac{D(C_2 - C_1)}{l} + uC_0\right]_{out} - \left[\frac{D(C_2 - C_1)}{l} + uC_0\right]_{in} = S_{sink}$$

$$\left[\frac{D(C_2 - C_1)}{l} + uC_0\right]_{out} - \left[\frac{D(C_2 - C_1)}{l} + uC_0\right]_{in} = \frac{i}{2\emptyset F} \qquad **$$

The advection term cancels out due to the continuity boundary condition, leaving us with only the diffusion term.

Applying BC 2:

$$\frac{dC}{dx} = B\frac{u}{\emptyset D}e^{\frac{u}{\emptyset D}x}$$

From BC 4:

$$at\ x = x_s^-, C = A + Be^{\frac{u}{\emptyset D}s-} = M + Ne^{\frac{u}{\emptyset D}s} \qquad ***$$

Domain 2:

$$C = M + Ne^{\frac{u}{\emptyset D}x}$$

$$at\ z = 0, C = C^+ = M+N$$

$$\frac{dC}{dz} = N\frac{u}{\emptyset D}e^{\frac{u}{\emptyset D}z}$$

$$at\ z = \frac{L}{2}, \frac{dC}{dz} = N\frac{u}{\emptyset D}e^{\frac{u}{\emptyset D}\frac{L}{2}} = 0 \rightarrow N = 0$$

From **, on the source and sink side, the B would be:

Source: $-N\frac{u}{\emptyset D}-(-DB\frac{u}{\emptyset D}e^{\frac{u}{\emptyset D}s})=\frac{i}{2\emptyset F}\rightarrow B=\frac{i}{2\emptyset F}*\frac{1}{D\lambda_2 e^{\lambda_2 s}}=\frac{i}{2Fue^{\frac{us}{\emptyset D}}}$

Sink: $N\frac{u}{\emptyset D}-DB\frac{u}{\emptyset D}e^{\frac{u}{\emptyset D}s}=\frac{i}{2\emptyset F}\rightarrow B=-\frac{i}{2\emptyset Fdx}*\frac{1}{D\lambda_2 e^{\lambda_2 s}}=\frac{-i}{2Fue^{\frac{us}{\emptyset D}}}$

Constant A would be calculated from *:

Source: A= $C_0-\frac{i}{2Fue^{\frac{us}{\emptyset D}}}$ sink: A=$C_0+\frac{i}{2Fue^{\frac{us}{\emptyset D}}}$

From***:

$$C^+=C^-\rightarrow M=A+Be^{\frac{u}{\emptyset D}s}$$

Source $$M=C_0-\frac{i}{2Fue^{\frac{us}{\emptyset D}}}+\frac{i}{2F}$$

Sink $$M=C_0+\frac{i}{2Fue^{\frac{us}{\emptyset D}}}-\frac{i}{2Fu}$$

Concentration profile in domain 1:

$$C=A+Be^{\frac{u}{\emptyset D}x}$$

Concentration profile in domain 2:

$$C=M$$

Ultimately, the concentration profiles for the first and second domains are as follows:

For the first domain, between the electrodes:

$$C(x)=C_0\pm\frac{i}{2FPe\frac{D}{s}e^{\frac{Pe}{\phi_m}}}\left(1-e^{\frac{Pe}{\phi_m s}x}\right)=C_0\pm\frac{i}{2Fue^{\frac{su}{\phi_m D}}}\left(1-e^{\frac{u}{\phi_m D}x}\right)$$

For the second domain, at the outlets:

$$C(x=\pm s)=C_0\pm\frac{i}{2FPe\frac{D}{s}}\left(\frac{1}{e^{\frac{Pe}{\phi_m}}}-1\right)=C_0\pm\frac{i}{2Fu}\left(\frac{1}{e^{\frac{su}{\phi_m D}}}-1\right)$$

From eq (2.4), the ASR can be calculated from the following equation:

$$ASR = \frac{D}{\Lambda}\left[\frac{1}{M_1 u_1} ln \frac{C_0 e^{\frac{u_1 s_1}{\phi_m D}}}{C(s_1)} + \frac{1}{M_2 u_2} ln \frac{C(s_2)}{C_0 e^{\frac{u_2 s_2}{\phi_m D}}}\right]$$

$u_1 = u$ $\qquad$ $u_2 = -u$

$s_1 = s$ $\qquad$ $s_2 = -s$

$M_1 = \mathrm{C}_0 - \frac{i}{2Fue^{\frac{us}{\phi_m D}}}$ $\qquad$ $M_2 = \mathrm{C}_0 + \frac{i}{2Fue^{\frac{us}{\phi_m D}}}$

Outflow Geometry for Electrochemical Separation

3.1Introduction

Managing large volumes of wastewater containing salt and organic compounds presents a significant environmental challenge, posing threats to soil, surface water, and groundwater quality. To mitigate these concerns, governments and organizations have established strict regulations to promote responsible management and treatment of salty wastewater. Industries like food processing, leather production, and petroleum manufacturing are now obligated to adhere to these rules, enhancing their commitment to environmental protection. Furthermore, addressing heavy metal contamination in subsurface soils and groundwaters caused by various human activities demands specialized techniques like chemical precipitation, coagulation, ion exchange, and solvent extraction, which have been explored in previous chapters. These methods play a vital role in efficiently separating and eliminating heavy metals from the environment, ensuring the well-being of ecosystems and human health [156].

The presence of sulfate ions (SO_4^{2-}) in water and wastewater can have detrimental effects on water quality, leading to issues like mineralization, corrosion, scaling, and the generation of corrosive hydrogen sulfide. Environmental regulations have imposed limits on sulfate concentrations in wastewater to mitigate these problems. Recently, innovative processes have been developed to selectively separate ions, both desirable and undesirable, from wastewater, groundwater, and seawater. Industries often employ these selective separation techniques to isolate Cl^- and SO_4^{2-} ions, reducing water pollution. Additionally, the separation of these ions allows for the production of valuable products such as NaCl and Na_2SO_4, which can be used in the manufacturing of substances like HCl, H_2SO_4, NaOH, and salt crystals, adding value and sustainability to the industrial processes [156,157].

Approaches like ion exchange, membrane filtrations, chemical participation and electrodialysis are methods that have specifically been reported to treat wastewaters containing Cl^- and SO_4^{2-}.

Among the membrane techniques, nanofiltration has been studied for its potential to separate monovalent and multivalent ions. In a study by Yan et al, nanofiltration was used to separate chloride and sulfate. It was reported that an increase in total salt concentration decreased the rejection of chloride and sulfate, while higher applied pressure increased rejection [156].

In ion exchange, the selective separation of chloride and sulfate was investigated by researchers with different anion exchange resins [63,158]. In a study by Hilal et al, it was reported that the chloride and sulfate separation depend on salt content in the feed. They also found higher hydrogen atoms in amine functional group of the resin lead to the higher ratio of the chloride selectivity to sulfate [158].

Chemical precipitation was also used for the separation of chloride and sulfate in the presence of precipitation agents like isopropylamine, diisopropylamine, and ethylamine [65,159]. pH, temperature, and contact time are important factors that should be considered to get high recovery efficiency [159].

Studies indicated that it is possible to separate chloride and sulfate ions by incorporating a monovalent selective anion exchange membrane [64,160,161]. Reig et al, reported the implementation of selectrodialysis (SED) and electrodialysis with bipolar membranes (EDBM). They successfully achieved purities of more than 90% SO_4^{2-} in the divalent-rich stream and about 90 % Cl^- in the monovalent-rich stream [160].

3.1.1 Symmetric selective redox electrodes

As discussed in the previous chapter, the cell applied in this study uses symmetric, regenerable porous silver electrodes. The operation is similar to that discussed earlier in 2.1.1 and 2.1.2. However, in this case we are interested in the selectivity of the electrode's electrochemical interactions with the multiple anions in the solution. Mobility of ions also plays an important role in the selectivity of the separation of the ions. The objective of this study is to understand the effect of electrode selectivity, ion mobility, and flow geometry on the separation of ions in electrochemical separation systems. This leads to the development of a novel method for ionic separation. It holds potential to reduce soil, surface, and ground water contamination.

In an electrochemical cell, the separation of Cl^- and SO_4^{2-} ions can involve a complex interplay of four key mechanisms: electrode selectivity, diffusion, electromigration, and advection. The mechanisms involved in electrochemical separation share similarities with those used in desalination processes. However, in desalination processes that use a symmetric electrolyte, it's possible to work with a single concentration value and eliminate the migration term, making the calculations simpler. In cases where different ions with varying mobilities are present, the influence of electromigration cannot be overlooked. Each ion's distinct mobility plays a crucial role in its behavior within the electrochemical cell, necessitating a more intricate consideration of the electromigration term to achieve effective ion separation.

When voltage is applied to a mixture of Cl^- and SO_4^{2-} ions, both ions are attracted to the positively charged electrode because of their opposite charges. However, due to differences in their mobility, SO_4^{2-} ions migrate more quickly in response to the electric field. As the chloride ions move toward the anode, they lose their charge and form solid silver chloride. On the other hand, SO_4^{2-} ions tend to accumulate near the anode but do not participate in electrochemical reactions. Therefore, they are pushed through the membrane due to advection, driven by the flow of the solution. This process is illustrated schematically in Figure 3-1.

$$J = (D\nabla C) - z\mu \boldsymbol{E}C + \boldsymbol{u}C$$

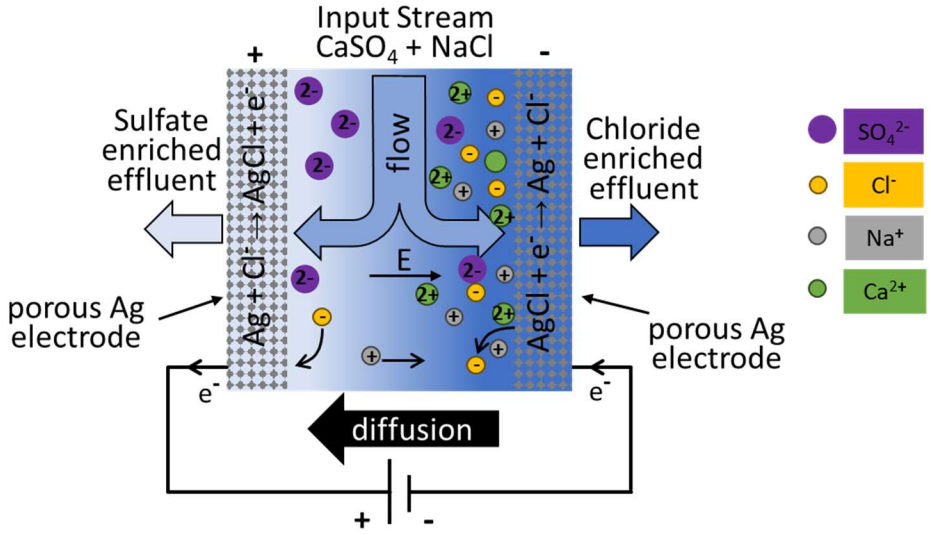

Figure 3-1: Schematic of Ag/AgCl electrochemical separation cell with outflow through electrodes

3.2Experimental procedures

A mixture of NaCl and $CaSO_4.2H_2O$ is introduced to the cell at an inlet flowrate of 40 µl/min. The separation process is performed at a constant voltage magnitude. The samples are collected at both outlets for ionic chromatography study to determine the value of the present ions in the samples.

3.2.1 Mixture components

The feed solution for the experiments consists of 50 mM NaCl and 17.5 mM $CaSO_4.2H_2O$. Gypsum ($CaSO_4.2H_2O$) added at 90% of the saturation concentration to 50 mM NaCl solution. The solubility of $CaSO_4.2H_2O$ depends on NaCl solution concentration. The solubility of $CaSO_4$ and $CaSO_4.2H_2O$ increases with increasing NaCl concentration in the range of 0 – 2 M. The solubility then declines at higher concentration of NaCl. At 50 mM NaCl concentration (by extrapolation from Marshall and Slusher), the solubility of $CaSO_4.2H_2O$ is 19.3 mM [162,163].

3.2.2 Separation experiment

As is discussed earlier in 2.2.2.4, one of the silver electrodes should be chlorided before running the experiment. 50 mM NaCl solution is used in the chloriding process at a constant voltage of 0.9 V. The final amount of the charge that is placed on the silver membrane is about 4 C.

After charging the electrode, a separation experiment is performed for an input mixture of 50 mM NaCl and 17.5 mM $CaSO_4.2H_2O$ with an inlet flowrate of 40 µl/min. This flow splits into two equal outlet streams with a flowrate of 20 µl/min. The cell was cycled at a constant voltage magnitude of 0.18 V with alternating polarity as described in the previous chapter. A multi-channel contactless conductivity detector (eDAQ ER825 C4D) was used for conductivity measurement on both outlets. By the depletion of AgCl layer on the reducing electrode, the cell current will drop. At this point the polarity should be switched. This happened at 0.3 of the initial current. Four-way valves alternatively direct the effluent from each electrode to the purified or enriched streams, depending on the bias of the electrode. A schematic of the cell with four-way valve is shown in Figure 3-2.

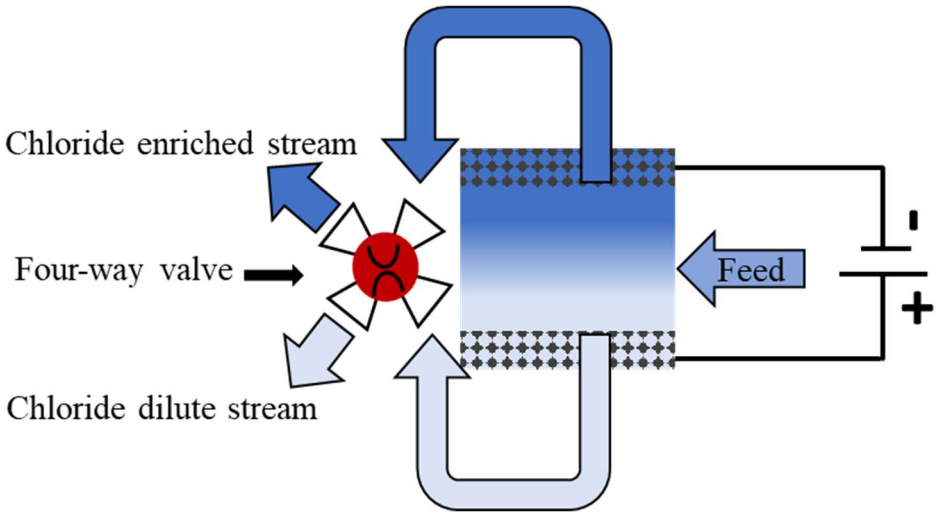

Figure 3-2: Schematic of the cell with a four-way valve

3.2.3 Ion chromatography

Implementation of ion chromatography in this study provides the concentration values of the ions present in the effluents. Since the concentration of ions in the effluents are high for ion chromatography, deionized water is used to dilute the samples to less than 100 mg/L. Deionized water samples are used as control samples. Before loading the samples, the ion chromatography columns should be calibrated by standard solution. The standard solutions are prepared for Na^+, Ca^{2+}, Cl^-, and SO_4^{2-} at 1, 10, 25, 50, 100 ppm. The concentration of the ions in the samples can be determined by comparing the data obtained for the sample to the known standard.

3.3 Results and Discussion

In the results and discussion section, we will delve into various aspects of our study. These include the examination of experimental results, analysis of concentration values obtained through ion chromatography, detailed characterization of the electrodes, evaluation of charge efficiency, assessment of energy efficiency, and a comprehensive exploration of the impact of varying operating conditions.

3.3.1 Basic cell operation

Symmetric, regenerable porous silver electrodes have the potential to separate chloride ions from other present anions in the solution. The electrodes selectively pick up chloride ions through electrochemical silver oxidation to insoluble silver chloride and release chloride ions in a reduction reaction to the solution. The selectivity of the ions also depends on their mobility.

3.3.2 Conductivity and IV

Selectivity of the silver electrodes of the cell leads to the separation of chloride ions from other present anions in the system. In this case, mobility is an important parameter that influences this behavior. Ions with slower mobility compared to chloride, have less chance to be separated from the solution. The mobility of Cl^-

and SO_4^{2-}ions are very close, but selectivity would be different for ions with lower mobility compared to chloride.

The separation process was started by introducing a mixture of 50 mM NaCl solution and 17.5 mM $CaSO_4$ at an inlet flowrate of 40 µl/min from the center of a symmetric electrochemical cell at a constant voltage magnitude of 0.18 V. The inlet stream splits into two equal flowrates of 20 µl/min. During the separation process, the silver anode combines with Cl^- ions from the solution in an oxidation reaction while the silver cathode releases Cl^- ions through a reduction reaction. The electrode functions are switched once a reverse polarity is applied.

Figure 3-3 shows the corresponding change in measured outlet solution conductivity. The conductivity on the enriched side is about 10 mS/cm while the conductivity on the dilute side is about 5 mS/cm. Unlike the calculation of the concentration of NaCl solution from a linear approximation of conductivity in desalination, the conductivity data of this experiment cannot be converted to concentration, as the conductivity of $CaSO_4$ cannot be neglected.

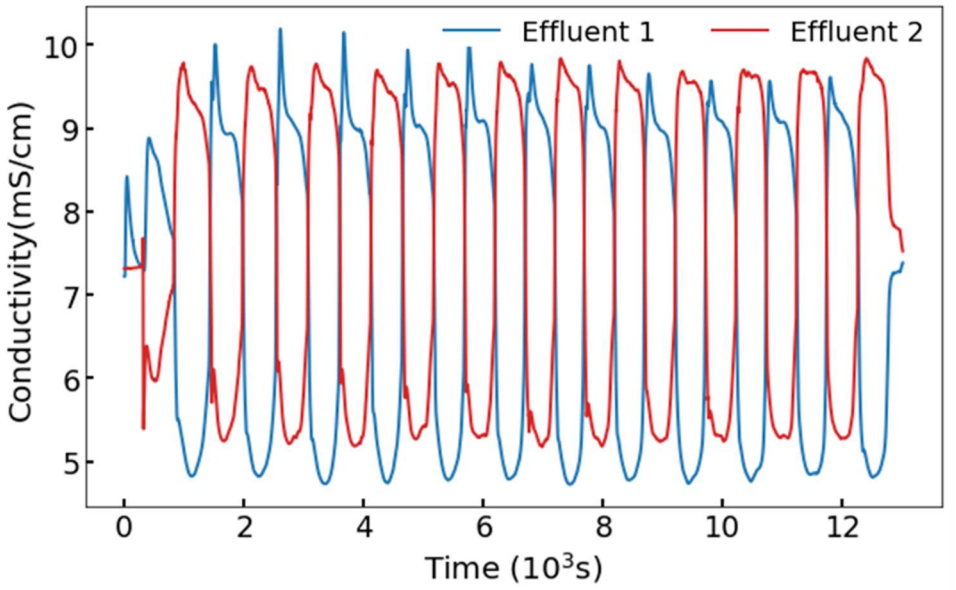

Figure 3-3: Changes in outlet solution conductivity for the mixture of 50 mM NaCl and 17.5 mM $CaSO_4$

Figure 3-4 shows the current flow through the cell for a voltage of 0.18 V (with alternating polarity). Each half cycle is about 400 s to 500 s long, and the length of cycle is set by the drop off in current. The average of the current density magnitude is about 40 A/m^2. Comparing the results of the mixture of the ions with pure NaCl solution shows that at the same voltage magnitude, the average current density is lower for the mixture of ions. This is something that needs to be investigated and addressed in further modeling.

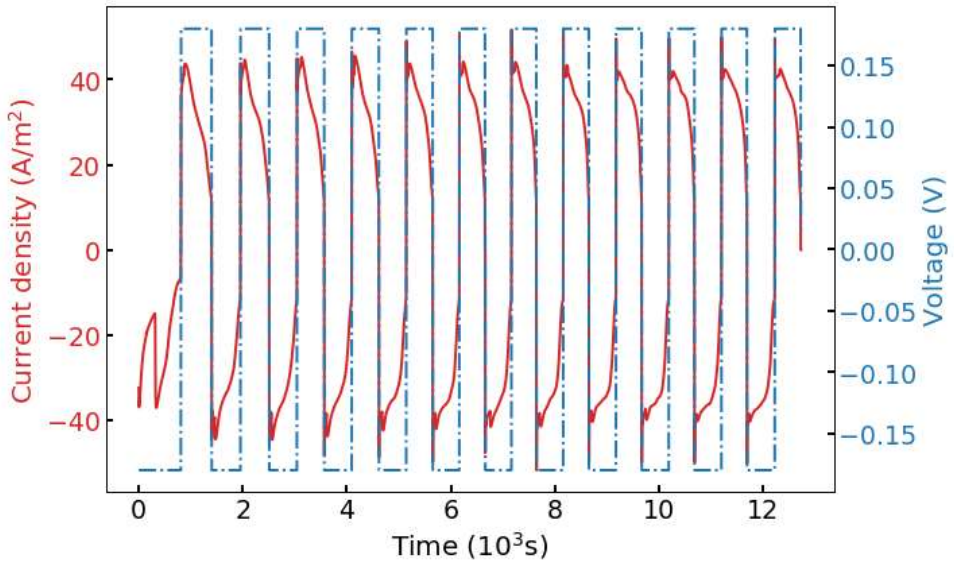

Figure 3-4: Changes in current and voltage vs time with alternating polarity

3.3.3 Concentration measurements

Ion chromatography works based on ion affinity to the ion exchanger in the column and provides concentration for each ion to indicate how efficient the electrochemical system is in ion separation. Ionic chromatography is applied to measure the composition of the outlet streams. The concentration of ions in the feed stream, sulfate enriched effluent, and chloride enriched effluent are shown in Figure 3-5. The amount of Cl^- decreased by half from the feed stream to the sulfate enriched effluent, while there is an increase in sulfate concentration in the sulfate enriched effluent. On the other hand, the amount of Cl^- increased from the feed stream to the chloride enriched effluent, while there is a decrease in sulfate concentration. The selectivity of the oxidation electrode leads to removal of the

chloride ions while the sulfate ions pass by. Chloride and sulfate have similar mobilities but for ions with lower mobility compared to chloride, electromigration would be slower.

In summary, Figure 3-5 reveals that, with the exception of sulfate, all other ions become concentrated in the chloride-enriched stream and are diluted in the sulfate-enriched stream.

The change in concentration for present ions in both effluents are given in Table 3-1. The increases for the anions, from input to enriched streams, of Cl^- and SO_4^{2-} ions are 43% and 22%, respectively. The increases for the Na^+ and Ca^{2+}, from input to enriched stream of Cl^- are 23% and 9%, respectively. Mass balance is somewhat violated based on these results. The discrepancy might be due to uneven flowrate of the pumps and/or the limited precision of the ionic chromatography.

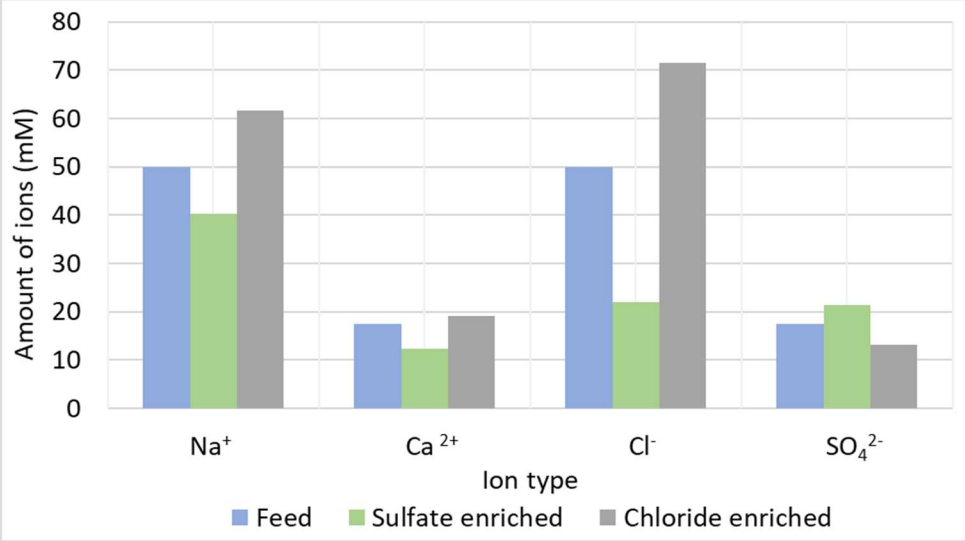

Figure 3-5: Ionic chromatography results for Na^+, Ca^{2+}, Cl^-, SO_4^{2-} in input, enriched and diluted effluents for 50 mM NaCl and 17.5 mM $CaSO_4$

Table 3-1: Percentage change in ions in outlet effluents by ionic chromatography

Ion type	Effluent	Concentration (mM)	Change in amount (%)
Cl^-	Chloride enriched	71.39	42.79 ⇧
	Sulfate enriched	21.91	56.16 ⇩
SO_4^{2-}	Sulfate enriched	21.32	24.38 ⇧
	Chloride enriched	13.23	21.84 ⇩
Na^+	Chloride enriched	61.57	23.15 ⇧
	Sulfate enriched	40.26	19.46 ⇩
Ca^{2+}	Chloride enriched	19.09	9.12 ⇧
	Sulfate enriched	12.43	28.93 ⇩

3.3.4 Characterization of the electrodes

The surface morphology of the electrodes was characterized by scanning electron microscopy (Zeiss Gemini SEM 500). The SEM images of the silver electrode illustrate the alterations occurring during the electrochemical reaction. The electrodes were used in experiments conducted at room temperature and maintained at a constant voltage of 0.18 V.

Figure 3-6 is an SEM image of the pristine silver. Figure 3-7 shows the changes of the reduced electrode, demonstrating the aggregation of Ag particles as they undergo conversion to AgCl. The change in oxidizing electrode is also shown in Figure 3-8.

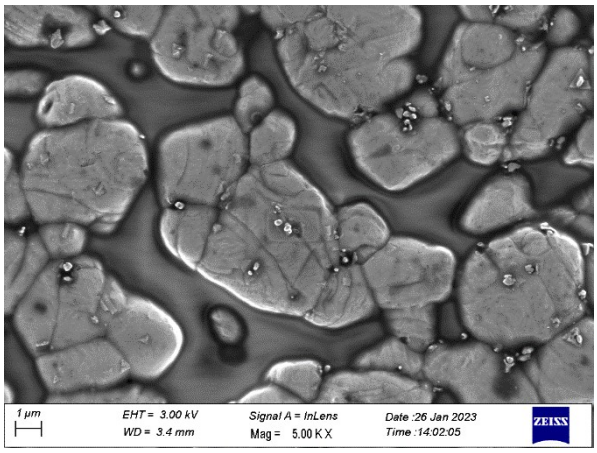

Figure 3-6: SEM image of pristine silver

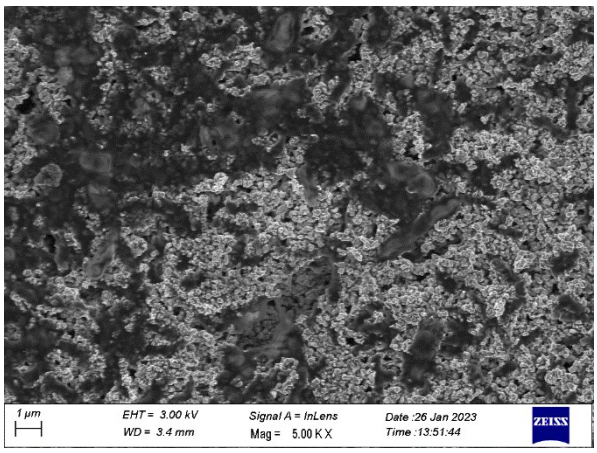

Figure 3-7: SEM image of silver electrode, showing the changes in the morphology of the electrode due to a reduction reaction and formation of AgCl.

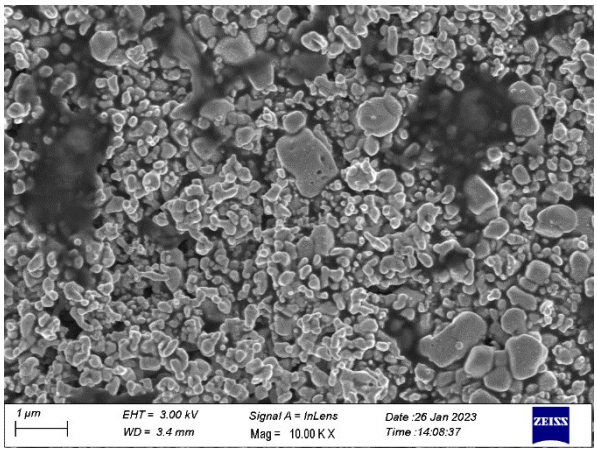

Figure 3-8: SEM image of silver electrode, showing the changes in the morphology of the electrode due to an oxidation reaction.

3.3.5 Charge efficiency

The charge efficiency of this system is calculated separately for different ions. The value for each anion is shown in Table 3-2. Here charge efficiency is defined using eq. 3-1, and the concentration measurements from ionic chromatography. ΔC is the difference between the feed and the final concentrations of the outlets. The charge efficiency of Cl^- in the mixture is 19.89% and this is similar to its value in pure NaCl.

$$\eta = \frac{u\Delta CF}{i} \tag{3.1}$$

Table 3-2: Charge efficiency of the present anions in the separation

Ion type	Charge efficiency
Cl^-	19.89%
SO_4^{2-}	3.25%

3.3.6 Energy efficiency

Energy per ion of the separation experiment is calculated using eq. 3-2, and the concentration measurements from ionic chromatography for the ions present in the mixture. The results are shown in Table 3-3.

$$\text{Energy per ion} = \frac{\text{Cell Power}}{\text{Separation rate}} = \frac{Vi}{u\Delta C} = \frac{VF}{\eta} \tag{3.2}$$

Table 3-3: Energy efficiency of the present anions in the separation

Ion type	Energy per ion (kJ/mol)
Cl^-	88.935
SO_4^{2-}	535.511

3.3.7 Effect of operating condition

According to the model, as velocity increases, the initial energy required for ion separation decreases. This reduction occurs because at very low velocities, diffusion is the dominant factor. However, as velocity increases further, the presence of advection becomes more significant and overcomes diffusion, resulting in decreased energy requirements for ion separation. Subsequently, the energy needed for ion separation increases again, mainly because the role of advection becomes more crucial, potentially demanding additional energy to maintain a same level of separation . So, at higher velocities, the system's throughput increases, but it comes at the cost of higher energy consumption. In other words, the velocity influences the balance between diffusion and advection, and the optimal velocity for ion separation depends on achieving the desired separation efficiency. Also,

increasing the advection velocity at a constant current reduces ohmic resistance by enhancing mass transport and promoting faster reaction rates. This reduction is attributed to more effective ion movement between the electrodes, alleviating concentration polarization and decreasing overall resistance. Nevertheless, resistance does not continuously decrease, as the rates of reactant delivery and consumption reach a balance, leading to a steady state resistance where further increases in advection velocity result in a decreasing influence on resistance reduction.

Electric fields can be adjusted to selectively separate specific ions of interest. By controlling the electric field, we can optimize the separation process to achieve higher selectivity for particular ions. The electric field's effect on chloride ions is generally less than on sulfate ions due to sulfate's mobility. Sulfate ions have higher mobility compared to chloride ions. This means that, under the same conditions, sulfate ions will migrate more quickly in response to the electric field.

When an electric field is applied across the cell, both Cl^- and SO_4^{2-} are drawn toward the positively charged electrode (anode) due to their negative charges. Chloride ions migrate towards the anode, where they combine with silver and form into AgCl. On the other hand, sulfate ions, which move at a faster pace, tend to accumulate near the anode. Eventually, they are driven through the membrane as there are no electrochemical reactions for them to participate in.

At a constant voltage, lower velocity allows the ions sufficient time to engage in electrochemical processes resulting in more effective separation While at higher velocity the separation is getting worse due to lack of time for the ions to undergo the electrochemical reactions.

At a consistent velocity, an increase in voltage intensifies the attraction for Cl^- ions, drawing more of them into the electrochemical reaction. Consequently, this increased electrochemical activity leads to better separation of Cl^- and SO_4^{2-}.

3.4Conclusion

The reduction of saline water discharge is a critical concern to prevent harm to soil, groundwater, and the environment. In this study, a selective electrochemical deionization cell with an outflow geometry was used to separate Cl^- and SO_4^{2-} ions. By adjusting electric fields and controlling velocity, specific ions can be selectively separated. SO_4^{2-} ions are more responsive to electric fields than Cl^- ions due to

their higher mobility. So, they can migrate towards the anode faster. Indeed, a stronger electric field and lower velocity can lead to better ion separation. A higher electric field enhances the attraction for chloride ions, creating a more effective "sink" for them, while lower velocity provides the ions with sufficient time to engage in the electrochemical separation processes. This combination of factors can significantly improve the efficiency of the separation.

Chapter 4

Outflow Geometry for Power Generation

4.1Introduction

The need for clean, renewable energy is more critical than ever to combat pollution, reduce carbon emissions, and move away from fossil fuels. While solar, wind, and geothermal power are well-known clean energy sources, there's growing interest in something new: “salinity energy” or “blue energy”. This idea harnesses the energy from the contrast between salty seawater and freshwater, providing a potential power source. When river water meets the sea, a mixing process happens, and we can use this to turn heat into electricity. Theoretical non-expansion work produced by mixing concentrated saltwater and dilute river water at a constant pressure and temperature to create a brackish solution is determined by the Gibbs energy of mixing [73].

This energy can come from natural processes like when river water mixes with seawater, or it can be generated by combining desalination brine with low-salinity wastewater [86,164].

We have different ways to harness the blue energy, including methods like pressure retarded osmosis, reverse electrodialysis, capacitive mixing and battery mixing which they are already discussed in 1.3.2. In all blue energy technologies, understanding and optimizing the Gibbs free energy of mixing is essential for improving the efficiency of the processes and maximizing the electrical power output.

What's unique about blue energy is that it's the opposite of desalination as it was comprehensively studied in 2, where we use energy to extract freshwater from seawater. It's incredibly eco-friendly, with no harm to the environment and no added heat or harmful substances. As the world gets better at capturing this energy, it could become an ideal source for a greener and more sustainable future.

4.2Methods

The cell consists of porous silver electrodes that absorb or emit negative chlorine ions. Freshwater and saltwater will be introduced as two separate inlets. When these two streams with different salt concentrations mix together, the Gibbs free energy of mixing can be converted to electrical energy. The Gibbs free energy of mixing per mole for the system can be calculated from eq. (4.1):

$$-\Delta G_{mix} = G_{total} - (\phi_{fresh} G_{fre} \quad + \phi_{salt} G_{salt}) \tag{4.1}$$

ϕ_{fres} and ϕ_{salt} are the ratios of the total moles of freshwater and saltwater, respectively, to the total moles in the system ($\phi_{fresh} + \phi_{salt} = 1$). G_{fresh} and G_{salt} are the initial Gibbs free energy for freshwater and saltwater and G_{total} is the Gibbs free energy for the final mixture. The equation essentially states that the Gibbs free energy change for the mixture is equal to the difference between the total Gibbs free energy of the system and the sum of the Gibbs free energies of the individual components (freshwater and saltwater) weighted by their volume fractions [82,86].

4.2.1 Governing equation

An analytical solution is employed to analyze the power generation process. The mass conservation equation is utilized to solve for a symmetric binary electrolyte, and the expression for it is provided in the eq. (4.2)

$$\frac{\partial C}{\partial t} = -\nabla \cdot \vec{J} + Source/-Sink = -D\frac{d^2C}{dx^2} + \frac{u}{\phi_m}\frac{dC}{dx} + \frac{i}{2F\phi_m\delta_{elec}} \tag{4.2}$$

To solve eq. (4.2), we partition the solution domain into two segments. The first segment spans from the flow inlets to the source/sink, while the second

segment covers the region from the source/sink to the center of the cell. We apply the boundary conditions outlined in the following section to solve the eq. (4.2.

4.2.2 Boundary conditions

Four boundary conditions (BC) are used to solve eq. (4.2) simultaneously for both regions (Figure 4-1). At the center of the cell (outlet), the concentration is held constant and equals the average of the feed concentrations (BC. 1). At the electrodes, the concentration remains fixed and matches the inlet concentrations ($C_{low} \neq C_{high}$) (BC. 2). Along the surfaces representing the electrodes, the difference between the fluxes on either side of the electrode is equal to the total strength of the source/sink (BC. 3), which is essentially the current over Faraday's constant. Lastly, there is continuity in concentration across the electrodes, ensuring a smooth transition between the two regions (BC. 4).

BC. 1 At $x = 0,\ C = C_M$

BC. 2 At $x = \pm L, C = C_{low} \& C_{high}$

BC. 3 At $x = \pm s$, $J_{out} - J_{in} = \frac{i}{2\phi_m F dx}$

BC. 4 At $x = \pm s,\ C^+ = C^-$

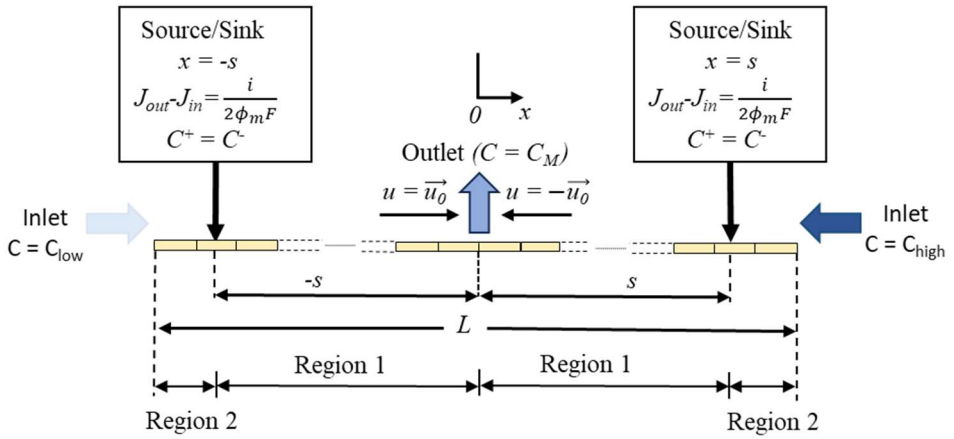

Figure 4-1 Schematic of model domains and boundary conditions in power generation

4.2.3 Model for potential in the system

As it was already stated in 2.2.1.1 the activation and AgCl layer resistance are insignificant. Consequently, the total potential across the cell, denoted as V, is expressed in relation to the local equilibrium electrode potential, E_{cell}, and the solution resistance loss, denoted as $i*ASR$ as demonstrated in eq (4.3). The current is flowing in the opposite direction. The situation in this case has similarities to the transients which occur during switching of the polarity for desalination at constant voltage magnitude, which lead to a high current at low voltage. E_{eq} and i*ASR have different signs. E.g., the current would be negative while E_{eq} would be positive. Power generated by the flow of current between the electrodes at different concentrations is partly dissipated by the solution loss.

$$V = E\_cell - i * ASR \tag{4.3}$$

The equilibrium electrode potential depends on the logarithm of the ratio of the concentrations, as illustrated in eq. (4.4) and solution resistance follows Ohm's law. The cell potential is therefore calculated using eq. (4.3), where ASR (Ω cm^2) represents the cell resistance normalized by its area and can be achieved by eq. (4.5).

$$E_{cell} = \frac{RT}{nF}\, ln \frac{[Cl^-_{Red}]}{[Cl^-_{Ox}]} \tag{4.4}$$

$$ASR = \int \frac{dx}{\Lambda \phi_m C} \tag{4.5}$$

4.3Results and discussion

4.3.1 Steady state behavior from analytical model

A steady-state analysis can indeed provide valuable insights into the performance of a system. Eqs.(4.6) and (4.7) detail the concentration profile as a function of position from the center to the electrodes, whereas eq. (4.8) and (4.9) depict the uniform concentration from the electrodes to the inlets.

Concentration between the electrodes:

$$C(x) = C_M + \left[C_{high} - C_M + \frac{i}{2uF}(e^{\frac{u(l-s)}{\phi_m D}} - 1)\right] \frac{(e^{\frac{u}{\phi_m D}x} - 1)}{e^{\frac{ul}{\phi_m D}} - 1} \tag{4.6}$$

$$C(x) = C_M + \left[C_{low} - C_M + \frac{i}{2uF}(1 - e^{\frac{u(l-s)}{\phi_m D}})\right] \frac{(e^{\frac{u}{\phi_m D}x} - 1)}{e^{\frac{ul}{\phi_m D}} - 1} \tag{4.7}$$

Concentration at the electrodes:

$$C = C_{high} + \left[\frac{e^{\frac{us}{\phi_m D}}\left(C_{high} - C_M\right) - \frac{i}{2uF}\left(e^{\frac{us}{\phi_m D}} - 1\right)}{e^{\frac{us}{\phi_m D}}\left(e^{\frac{ul}{\phi_m D}} - 1\right)}\right] * \left(e^{\frac{ux}{\phi_m D}} - e^{\frac{ul}{\phi_m D}}\right) \quad (4.8)$$

$$C = C_{low} + \left[\frac{e^{\frac{us}{\phi_m D}}\left(C_{low} - C_M\right) + \frac{i}{2uF}\left(e^{\frac{us}{\phi_m D}} - 1\right)}{e^{\frac{us}{\phi_m D}}\left(e^{\frac{ul}{\phi_m D}} - 1\right)}\right] * \left(e^{\frac{ux}{\phi_m D}} - e^{\frac{ul}{\phi_m D}}\right) \quad (4.9)$$

The cell voltage, as defined in eq.(4.3), can be calculated solely based on the concentration profile given in eqs. (4.6) and (4.7) and the operational current of the cell. The solution resistance is the predominant component as it was already discussed in 2.2.1.1. By combining eqs. (4.5), (4.6) and (4.7), we derive an expression for the steady-state total cell area-specific resistance as follows:

$$ASR = \frac{D}{\Lambda}\left[\frac{1}{A_1 u_1}\, ln\frac{C_M e^{\frac{u_1 S_1}{\phi_m D}}}{A_1 + B_1 e^{\frac{u_1 S_1}{\phi_m D}}} + \frac{1}{A_2 u_2}\, ln\frac{A_2 + B_2 e^{\frac{u_2 S_2}{\phi_m D}}}{C_M e^{\frac{u_2 S_2}{\phi_m D}}}\right] \quad (4.10)$$

$u_1 = -u$ $\qquad$ $u_2 = u$

$s_1 = s$ $\qquad$ $s_2 = -s$

$$N_1 = \frac{(C_{low} - C_M) + \frac{i}{2uF}\left(1 - \frac{1}{e^{\frac{us}{\phi_m D}}}\right)}{\left(e^{\frac{ul}{\phi_m D}} - 1\right)} \qquad N_2 = \frac{-\left(C_{high} - C_M\right) + \frac{i}{2uF}\left(1 - \frac{1}{e^{\frac{us}{\phi_m D}}}\right)}{-\left(e^{\frac{ul}{\phi_m D}} - 1\right)}$$

$$M_1 = C_{low} - N_1 * e^{\frac{ul}{\phi_m D}} \qquad M_2 = C_{high} - N_2 * e^{\frac{ul}{\phi_m D}}$$

$$B_1 = \frac{C_{low} - C_M - N_1 * \left(e^{\frac{ul}{\phi_m D}} - e^{\frac{us}{\phi_m D}}\right)}{e^{\frac{us}{\phi_m D}} - 1} \qquad B_2 = \frac{C_{high} - C_M - N_2 * \left(e^{\frac{ul}{\phi_m D}} - e^{\frac{us}{\phi_m D}}\right)}{e^{\frac{us}{\phi_m D}} - 1}$$

$$A_1 = C_M - B_1 \qquad A_2 = C_M - B_2$$

4.3.2 Impact of velocity on concentration profile

According to the concentration profiles provided in eqs. (4.6) and (4.7), the concentration values are influenced by the velocity. When the current remains constant and the flow rate increases, the disparity in concentration between the electrodes widens. This increased difference in concentration results in elevated resistance between the electrodes and a higher equilibrium potential. Consequently, the total voltage of the cell rises as a result.

The concentration variations with respect to distance are depicted in Figure 4-2. The current remains nearly constant at approximately 0.011 A, while the velocity spans a range from 3.33 to 8.33, 16.67, and 166.67 μm/s. At 166.67 μm/s, the advection term exerts a substantial influence, resulting in minimal changes in the inlet concentrations. Conversely, at 3.33 μm/s, the role of diffusion becomes more pronounced, leading to more noticeable concentration changes.

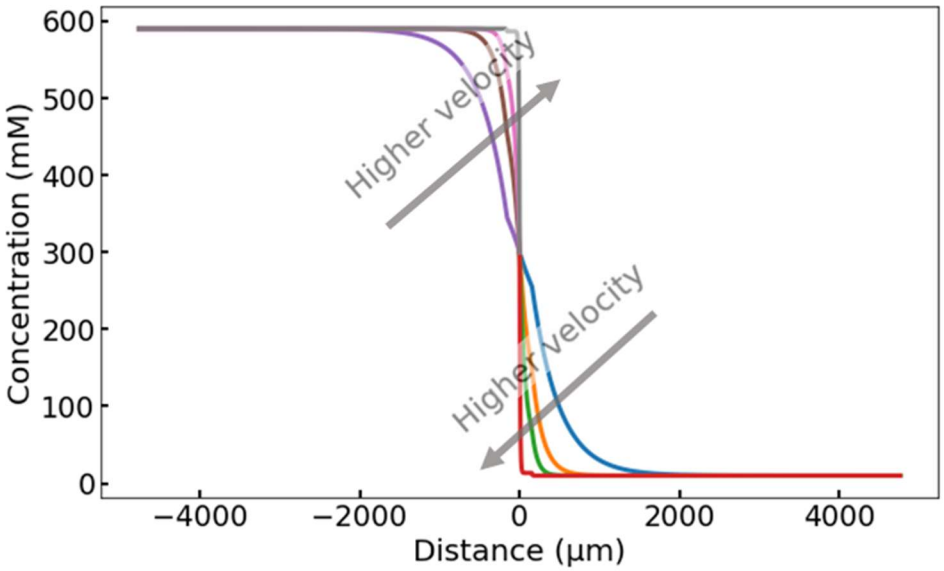

Figure 4-2: Effect of different velocities on concentration profile

Figure 4-3 provides a detailed examination of the alterations in the concentrations of the inlet solutions and illustrates how advection and diffusion can impact the concentration of Cl^- at the electrode surfaces. The dashed lines in the figure indicate the positions of the electrodes.

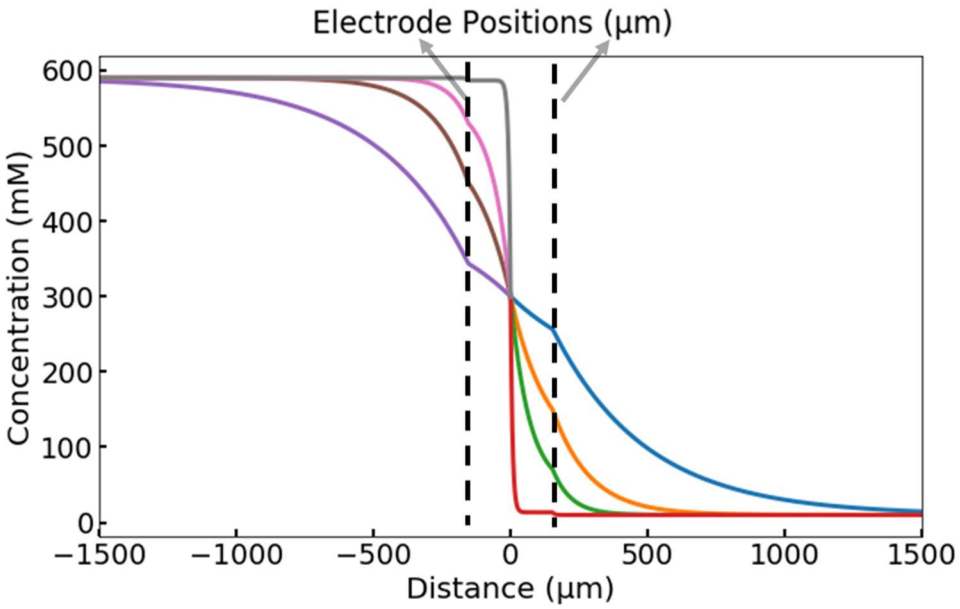

Figure 4-3: Closer look on the changes in concentration profile due to variation in velocity up to the steady state condition

4.3.3 Effect of current on concentration profile

Current is another significant factor that influences the concentration values within the concentration profile. When the velocity remains constant, an increase in current leads to a convergence of concentrations at the surface of the electrodes. This convergence narrows the gap in concentration, thereby lowering the equilibrium potential. Simultaneously, the resistance between the electrodes decreases as the concentrations become more similar, resulting in a reduction in the total voltage.

Figure 4-4, displays the alterations in concentration vs distance. This data is provided for a velocity of 33.33 μm/s and for a range of current values spanning from 0 to 0.009 A. When the current is zero, there is no apparent change in the concentration at the electrode. However, at higher current values, the electrodes function as a sink/source of chloride ions. The presence of the sink and source causes a reduction in the ΔC between the electrodes, which subsequently leads to a decrease in the overall resistance between the electrodes.

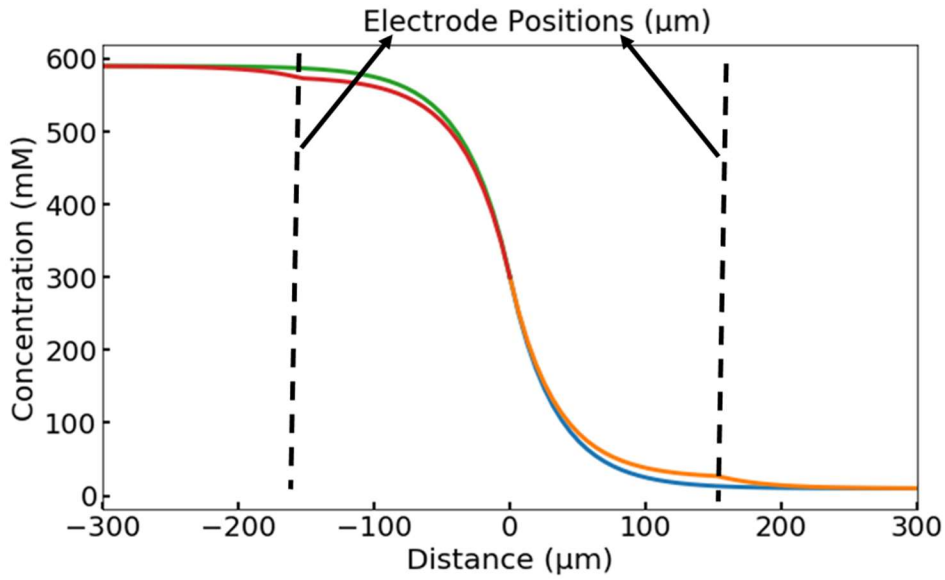

Figure 4-4: Impact of varied current levels on concentration profile

4.3.4 Cell IV curve

IV curves offer valuable insights into the efficiency, performance, and optimization of a system. By analyzing IV curves, we can assess the relationship between electrical current and voltage, helping to pinpoint the optimal operating conditions for maximum power output.

In Figure 4-5-a, the IV curves are presented, illustrating a broad range of velocities, spanning from 1.67 µm/s to 166.67 µm/s. When maintaining a constant velocity, an increase in current has the effect of bringing the concentrations of the electrodes at the surface closer together, thereby decreasing the equilibrium potential. Simultaneously, the resistance between the electrodes decreases as the concentrations become more similar, resulting in a reduction in the total voltage.

At a constant current, as the velocity increases, we observe an initial increase in voltage followed by a subsequent decline. When the current remains constant and the velocity rate increases, there is a widening difference in concentration between the electrodes, which leads to an increase in resistance between them and an elevated equilibrium potential. Consequently, this results

in an overall increase in the total voltage of the cell. This effect is visually represented in Figure 4-5-b.

In this system, the electrodes don't function as ideal voltage sources that can always maintain a consistent voltage. They require a chloride ion for every electron to facilitate the electrochemical reaction. At sufficiently high velocities, the concentration at the electrode surfaces closely match the inlet concentration. Consequently, the voltage between the electrodes becomes fixed. Therefore, as the velocity increases beyond a certain point, it no longer leads to a rise in voltage, and the open circuit voltage (OCV) stabilizes at an almost constant value. This behavior is clearly depicted in Figure 4-5-c and Figure 4-7. Nevertheless, this phenomenon does impact the resistance of the system since ΔC varies with different velocities. At higher velocities, ΔC is more significant, resulting in elevated resistance. This, in turn, causes a reduction in current, as visually represented in Figure 4-5-c and Figure 4-7.

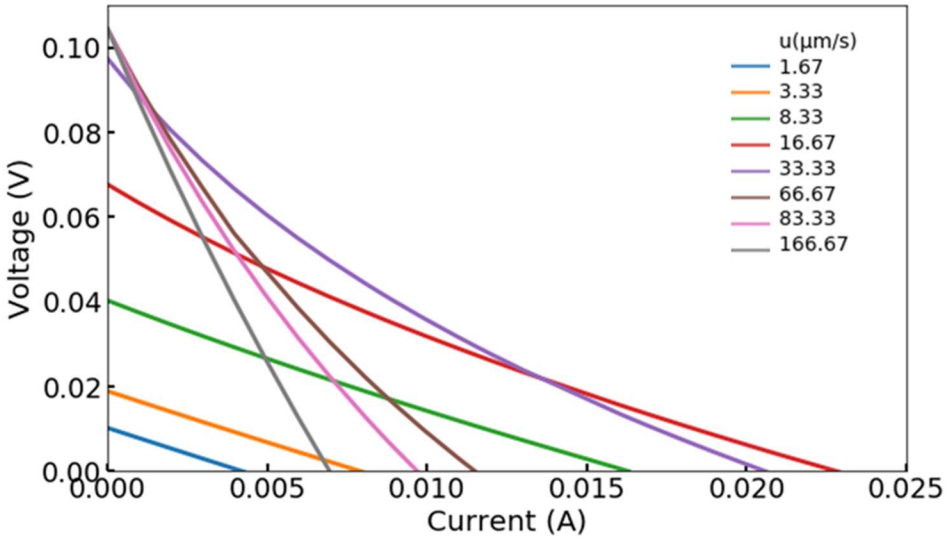

a.)

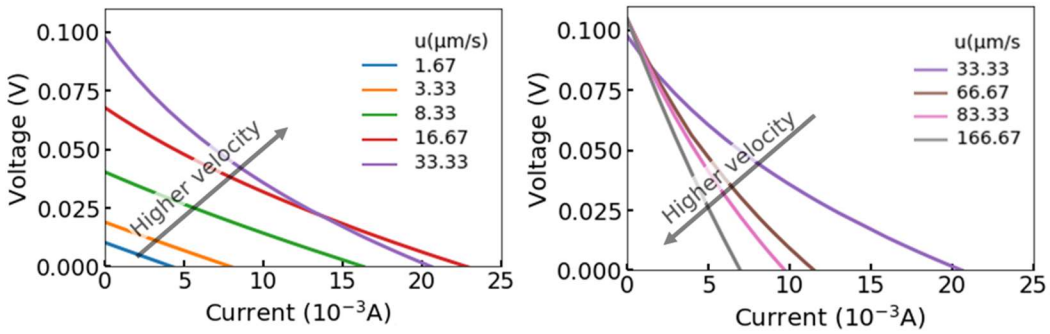

b.) c.)

Figure 4-5: a.) Correlation between cell current and voltage as a function of velocity b.) Increase in cell current with velocity up to 33.33 μm/s c.) Reduction in cell current with velocities greater than 33.33 μm/s

Figure 4-6 depicts the relationship between resistance and current, illustrating the change in resistance with respect to current up to the point where the voltage reaches a negative value. The dashed line represents the specific current, with concentration profiles displayed on the right.

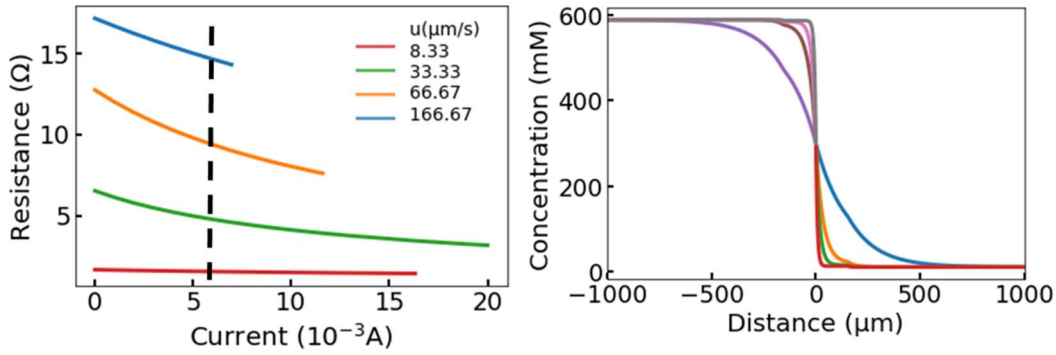

Figure 4-6: Relationship between resistance and current, demonstrating resistance changes with respect to current up to negative voltage. The dashed line represents an arbitrary current, with corresponding concentration profile shown on the right.

IV curves provide essential information for calculating the OCV and the short-circuit current. These parameters are fundamental for assessing the performance and behavior of electrical devices and systems. The OCV and short-circuit current

are determined by analyzing the IV curve and are visually represented in Figure 4-7.

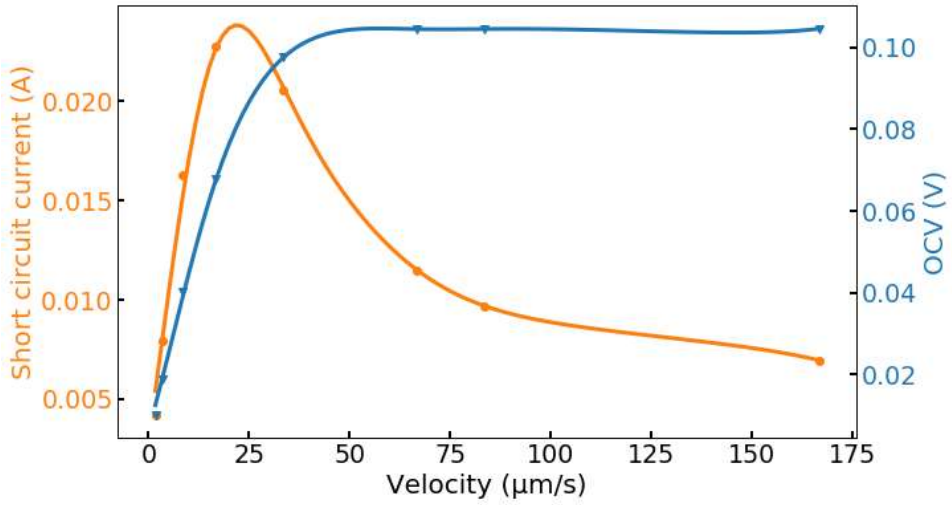

Figure 4-7: Variation of short-circuit current and OCV with respect to velocities.

4.3.5 Cell power

The power that could be generated from natural salinity gradients can be harnessed through the Gibbs energy of mixing. The free energy of mixing represents the maximum amount of energy available for performing useful work in a reversible thermodynamic process, without accounting for thermodynamic losses.

The Gibbs energy of a mixture, denoted as M, in a binary system containing species A and B of a strong electrolyte solution is the difference in Gibbs free energy between the final mixture (G_{Mix}) and initial solutions A and B (4.1).

The total molar Gibbs free energy of the solution, labeled as G, is an expression of the system's thermodynamic potential and can be determined using eq. (4.11)

$$G = \sum x_i G_i + RT \sum x_i \, ln \, \gamma_i \, x_i \tag{4.11}$$

G_i is the molar Gibbs energy of pure species i at temperature T and pressure P. R is the gas constant and x_i is the mole fraction of species i in the solution. γ_i is the activity coefficient, representing how the behavior of the solution deviates from an ideal solution.

By substituting eq. (4.11) into equation (4.1) the Gibbs energy of mixing is reduced to the eq. (4.12):

$$-\Delta G_{mix} = RT\left\{\left[\sum x_i\, ln(\gamma_i\, x_i)\right]_M - \phi_{fresh}\left[\sum x_i\, ln(\gamma_i\, x_i)\right]_{fresh} - \phi_{salt}\left[\sum x_i\, ln(\gamma_i\, x_i)\right]_{salt}\right\} \tag{4.12}$$

For low salt concentrations, the value of the salt activity in logarithmic terms is negligible compared to the mole fraction of salt. Therefore, the effects of activity coefficients are neglected, and eq. (4.12) can be simplified to eq. (4.13) where ν is the number of ions into which each electrolyte molecule dissociates.

$$-\Delta G_{mix} = \nu RT\left[\frac{C_M}{\phi} ln\, C_M - C_{fresh}\, ln\, C_{fresh} - \frac{(1-\phi)}{\phi} C_{salt}\, ln\, C_{salt}\right] \tag{4.13}$$

Figure 4-8-a provides predictions for cell power generation as a function of current at various velocities. Maintaining a fixed electrode spacing and Δc, the figure illustrates that power progressively escalates with increasing velocity, reaching a peak at 33.33 μm/s (Figure 4-8:-b). However, beyond this threshold, power output starts to diminish. This decline in power is due to a reduction in current, as previously explained in 4.3.4, impacting the power, which is a

product of voltage and current. This trend is visually represented in Figure 4-8-c.

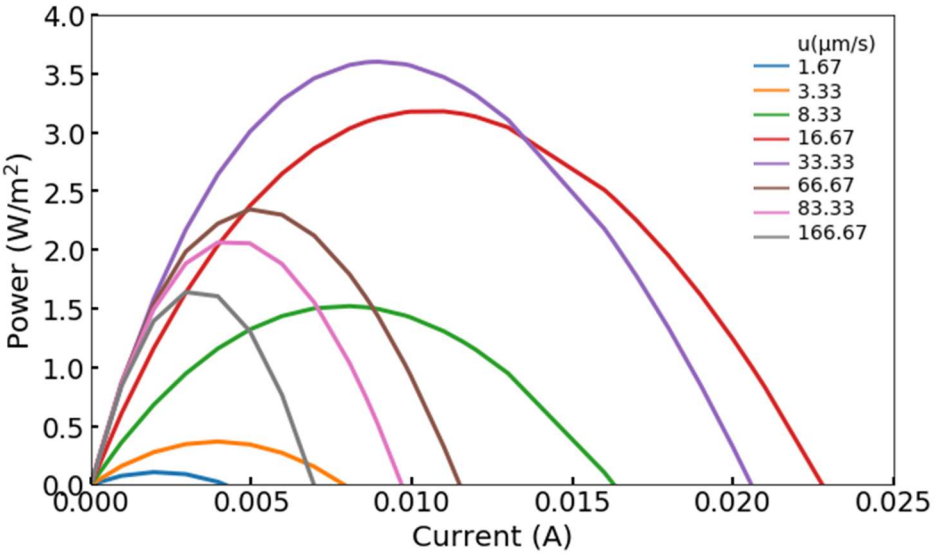

a.)

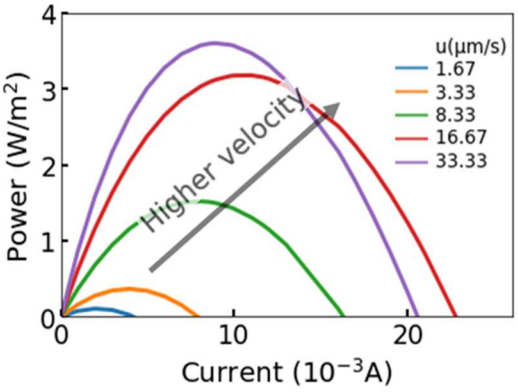

b.)

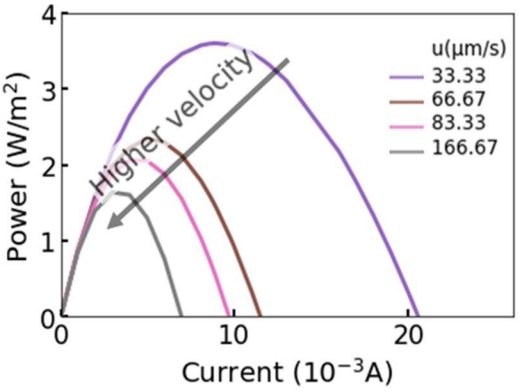

c.)

Figure 4-8: a.) Power generation predictions vs. current at different velocities b.) Increase in power generation with velocity up to 33.33 μm/s c.) Reduction in power generation with velocities greater than 33.33 μm/s

4.3.6 Effect of different initial concentration difference

The power obtainable from the cell significantly relies on the concentrations of the inlet solutions. A greater disparity between the inlet concentrations leads to higher power output, primarily due to the increased driving force available for electrical energy conversion. Conversely, as the difference between the inlet concentrations decreases, the power output diminishes. Figure 4-9 provides a visual representation of this relationship.

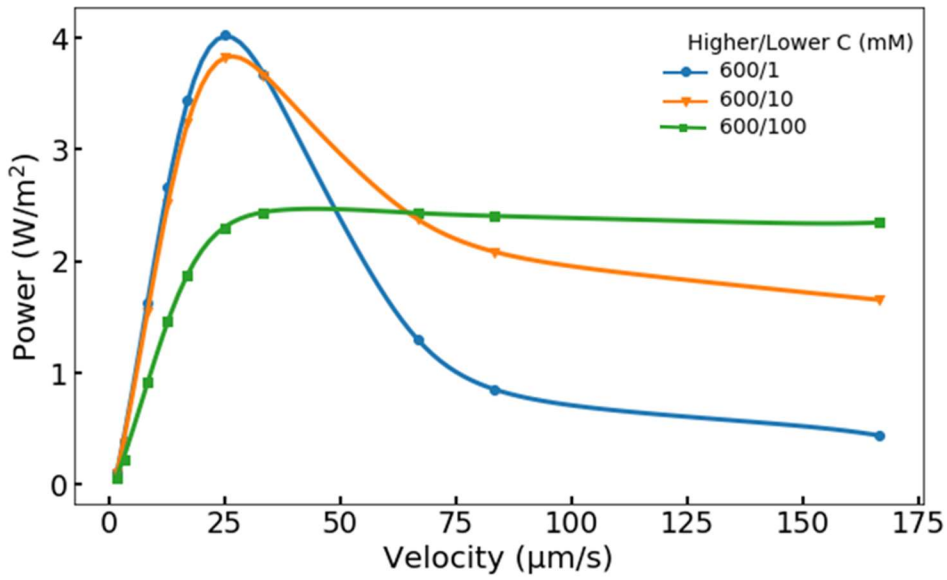

Figure 4-9: Effect of different initial concentration difference on power

4.3.7 Effect of electrodes spacing on maximum power for different velocities

The power that can be extracted from the cell is strongly dependent on the electrodes spacing. When the distance between the electrodes is decreased, the reduced inter-electrode distance results in lower resistance between them, yielding a lower voltage at a constant current. This adjustment allows the cell to operate at higher currents, leading to an increase in power generation. This behavior is visually illustrated in Figure 4-10. Specifically, at an electrode spacing of 100 μm, the cell is capable of generating a maximum power of

approximately 11.6 W/m², representing a notable increase compared to the cells with electrode spacings of 200 and 300 μm.

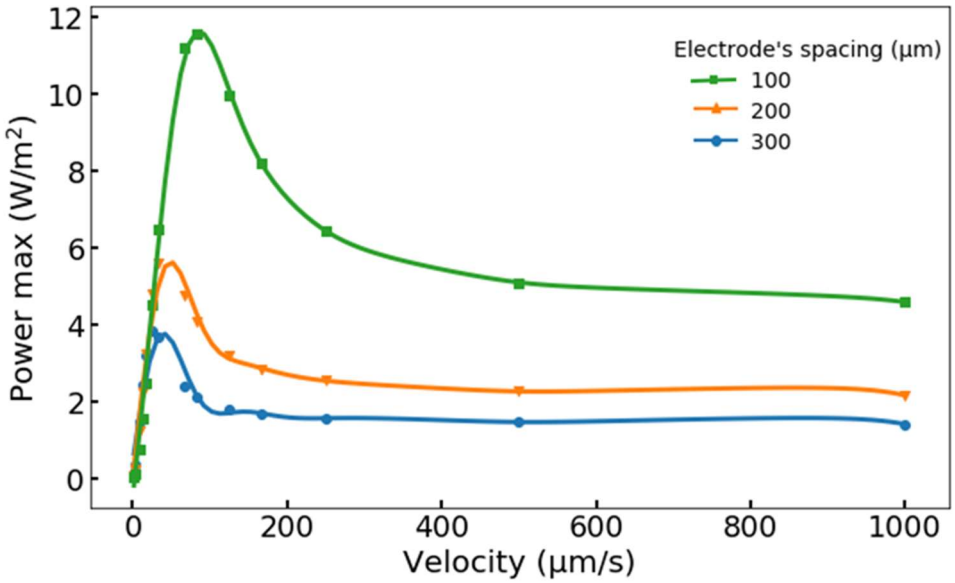

Figure 4-10: Effect of electrode spacing on maximum power for different velocities.

4.3.8 Comparison of the system energy efficiency vs thermodynamic energy for mixing

The thermodynamic energy of mixing is calculated using eq. (4.13) for a mixture with a concentration of 300 mM and inlet concentrations of 1 and 590 mM, with a water recovery of 0.5. In Figure 4-11, orange circle symbols represent the thermodynamic minimum energy, expressed as the energy released per unit area of the electrodes, as a function of the velocity of the inlet solutions. Additionally, orange triangle symbols illustrate the maximum power generated by the cell as a function of the velocity of the inlet solutions. The blue curve represents the cell's efficiency, with its peak efficiency occurring at a velocity of 12.5 μm/s.

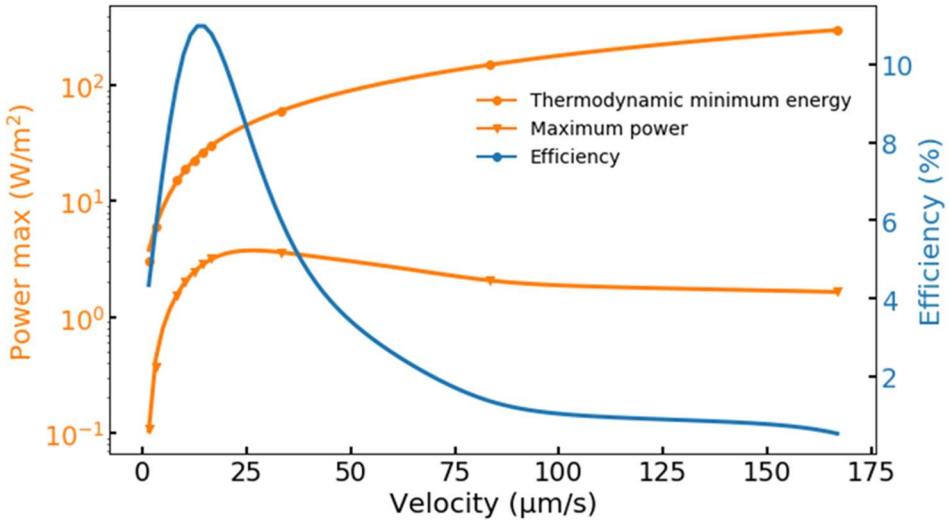

Figure 4-11: Comparison of the system energy vs thermodynamic energy of mixing

4.3.9 Comparison of power density to other blue energy approaches

Power density is a crucial factor for comparing blue energy technologies. Pressure retarded osmosis and reverse electrodialysis are indeed two environmentally friendly methods for generating power. The power density can vary depending on various factors, including the salinity gradient, the properties of the membranes and materials used, and the specific design of the systems.

Careful selection of operating parameters, a seawater-river water reverse electrodialysis system can potentially achieve a maximum gross power density of 3.5 W/m^2. This level of performance is attainable when employing low-resistance ion exchange membranes (0.5 Ω cm^2) and maintaining very small spacing intervals (50 μm) [165]. A study by Vermaas et al report on RED suggests that achieving a net power density of approximately 20 W/m2 is feasible when the membrane resistance is decreased to 0.1 Ω cm², coupled with a cell length of 1mm. It's important to note that a design with such a small cell length has not been tested and obtaining a membrane resistance as low as 0.1 Ω cm² is yet to be achieved. Nevertheless, this research highlights the effectiveness of the strategy to simultaneously reduce both the cell length and membrane resistance in enhancing the net power density in reverse electrodialysis [106].

In the case of pressure retarded osmosis, the maximum power densities were documented at 2.7 W/m² for 35 g/L NaCl draw solutions and 5.1 W/m² for 60 g/L NaCl draw solutions when operating at a hydraulic pressure of 970 kPa [84]. Fouling is a significant problem in PRO as it leads to reduced productivity by causing flux decline and a shorter lifespan for the membrane [166].

The power density of the electrochemical cell in this study, with inlet solutions of 0.58 g/L for river water and 34.45 g/L for salty water, an electrode spacing of 100 μm, and an inlet velocity of 83 μm/s is approximately 12 W/m^2. Unlike PRO, which faces issues like fouling, or RED with membrane resistance problems, this cell operates without a membrane. Nevertheless, it introduces a unique challenge related to the flow of the feed solution within the electrode plane before passing through the electrodes. This challenge imposes restrictions on the feasible width for a single electrode. To scale up the system for larger applications, ensuring the even distribution of the feed solution throughout the electrodes becomes essential.

4.4Conclusion

In this study, we've introduced a novel electrochemical cell that harnesses unique outflow geometry to create power from salinity gradients. We have examined this system using steady-state analytical models. Our focus has been on optimizing the overall power generation performance by fine-tuning various parameters, including inlet velocities, imposed current, inlet concentrations and electrode spacing. In our research, we evaluated key metrics such as power density and efficiency, which are crucial for comparing our blue energy technology with others in the field.

Increasing the difference in inlet concentrations, reducing electrode spacing, and applying higher current can enhance the power generation performance. The velocity also plays a vital role in the cell's performance. As the velocity increases, so does the cell's power density. However, beyond a certain velocity, there is a decline in power density. This decrease signals a high resistance between the electrodes, which requires a higher voltage to overcome.

The unique outflow geometry of the cell provides a continuous supply of electrolyte to the electrodes, offering two distinct advantages. Firstly, it lowers the solution resistance in areas with substantial depletion, and secondly, it diminishes the equilibrium potential of the electrodes by mitigating concentration polarization. These effects exert a substantial impact on the cell's throughput, enabling it to

operate at higher superficial velocities in comparison to competing technologies such as PRO and RED.

4.5Appendix

4.5.1 Analytical solution

The comprehensive derivation of the analytical solution is presented here.

$$\frac{\partial C}{\partial t} = -\nabla \cdot \vec{J} + Source/-Sink = -D\frac{d^2C}{dx^2} + \frac{u}{\phi_m}\frac{dC}{dx} + \frac{i}{2F\phi_m\delta_{elec}}$$

Boundary conditions:

5. At the inlet (cell center), the concentration is fixed to the feed concentration (BC 1)

BC. 1 At $x = 0$, $C = C_M$

6. At the outlets, the gradient of the concentration is zero (BC. 2)

BC. 2 At $x = \pm L, C = C_{low}$ & C_{high}

7. At the surfaces between the regions, representing the electrodes, the difference between the fluxes on either side of the electrode is equal to the total strength of the source/sink (BC. 3) (i.e., current over Faraday's constant).

BC. 3 At $x = \pm s$, $J_{out} - J_{in} = \frac{i}{2\phi_m F}$

8. The concentration is continuous across the electrodes (between the two regions) (Continuity equation) (BC. 4).

BC. 4 At $x = \pm s$, $C^+ = C^-$

The ODE

$$ay'' + by' + cy = 0$$

where a, b, c are constants (with $a \neq 0$) always has a solution of the following form:

$$y = e^{\lambda t}$$

where λ is a constant (which may be real or complex), to be determined. Making this substitution in the ODE, it is found that λ must satisfy the auxiliary equation $a\lambda^2 + b\lambda + c = 0$

The real solution for this equation is:

$$y = Ae^{\lambda_1 x} + Be^{\lambda_2 x}$$

At sink/source =0

$$D\lambda^2 - \frac{u}{\emptyset}\lambda = 0 \rightarrow \lambda_{1,2} = \frac{-b \pm \sqrt{b^2 - 4ac}}{2a}$$

From the equation, $c = 0$

$$\lambda_1 = -b + b = 0$$

$$\lambda_2 = \frac{-b}{a} = \frac{u}{\emptyset D}$$

The concentration profile would be:

$$C = Ae^{\lambda_1 x} + Be^{\lambda_2 x}$$

By substituting λ_1 and λ_2, the concentration profile would be:

$$C = A + Be^{\frac{u}{\emptyset D}x}$$

$$\frac{dC}{dx} = B\frac{u}{\emptyset D}e^{\frac{u}{\emptyset D}x}$$

$$C = M + Ne^{\frac{u}{\emptyset D}x}$$

$$\frac{dC}{dx} = N\frac{u}{\emptyset D}e^{\frac{u}{\emptyset D}x}$$

Now we need to apply the boundary conditions to the concentration profile:

Domain 1:

Applying the BC 1:

$$at\ x = 0, C = C_M$$

$$C_M = A + B \rightarrow A = C_M - B$$

Applying the BC 3 and BC 4:

$$at\ x = x_s^-, J_{out} - J_{in} = S_{sink}$$

$$\left[\frac{D(C_2 - C_1)}{l} + uC_0\right]_{out} - \left[\frac{D(C_2 - C_1)}{l} + uC_0\right]_{in} = S_{sink}$$

$$\left[\frac{D(C_2 - C_1)}{l} + uC_0\right]_{out} - \left[\frac{D(C_2 - C_1)}{l} + uC_0\right]_{in} = \frac{i}{2\emptyset F}$$

The advection term cancels out due to the continuity boundary condition, leaving us with only the diffusion term.

Source: $D(-N\frac{u}{\emptyset D} + B\frac{u}{\emptyset D}e^{\frac{u}{\emptyset D}s}) = \frac{i}{2\emptyset F}$

Sink: $D\left(N\frac{u}{\emptyset D} - B\frac{u}{\emptyset D}e^{\frac{u}{\emptyset D}s}\right) = \frac{i}{2\emptyset F}$

From BC 2:

$$C_{low} = M + Ne^{\lambda_2 l}$$

From BC 4:

$$at\ x = s, C^+ = C^- \rightarrow A + Be^{\lambda_2 s} = M + Ne^{\lambda_2 s}$$

Calculation of the constants:

Source side

$$N = \frac{\lambda De^{\lambda s}(C_{low} - C_M) + \frac{i}{2\varphi F}(e^{\lambda s} - 1)}{\lambda De^{\lambda s}(e^{\lambda l} - 1)}$$

$$M = C_{low} - N * e^{\lambda l} = C_{low} - [\frac{\lambda De^{\lambda s}(C_{low} - C_M) + \frac{i}{2\varphi F}\left(e^{\lambda s} - 1\right)}{\lambda De^{\lambda s}(e^{\lambda l} - 1)} * e^{\lambda l}]$$

$$B = \frac{M + N * e^{\lambda s} - C_M}{e^{\lambda s} - 1} = \frac{C_{low} - C_M - N * (e^{\lambda l} - e^{\lambda s})}{e^{\lambda s} - 1}$$

$$= \frac{C_{low} - C_M - [\dfrac{\lambda D e^{\lambda s}(C_{low} - C_M) + \dfrac{i}{2\varphi F}\left(e^{\lambda s} - 1\right)}{\lambda D e^{\lambda s}(e^{\lambda l} - 1)}] * (e^{\lambda l} - e^{\lambda s})}{e^{\lambda s} - 1}$$

$$A = C_M - B = C_M$$

$$- \frac{C_{low - C_M} - [\dfrac{\lambda D e^{\lambda s}(C_{low} - C_M) + \dfrac{i}{2\varphi F}\left(e^{\lambda s} - 1\right)}{\lambda D e^{\lambda s}(e^{\lambda l} - 1)} * (e^{\lambda l} - e^{\lambda s})}{e^{\lambda s} - 1}]$$

Sink side

$$N = \frac{-\lambda D e^{\lambda s}\left(C_{high} - C_M\right) + \dfrac{i}{2\varphi F}(e^{\lambda s} - 1)}{-\lambda D e^{\lambda s}(e^{\lambda l} - 1)}$$

$$M = C_{high} - N * e^{\lambda l} = C_{high} - \frac{\lambda D e^{\lambda s}\left(C_{high} - C_M\right) + \dfrac{i}{2\varphi F}(e^{\lambda s} - 1)}{\lambda D e^{\lambda s}(e^{\lambda l} - 1)} * e^{\lambda l}$$

$$B = \frac{C_{high - C_M} - N * (e^{\lambda l} - e^{\lambda s})}{e^{\lambda s} - 1}$$

$$= \frac{C_{high - C_M} - \dfrac{\lambda D e^{\lambda s}\left(C_{high} - C_M\right) + \dfrac{i}{2\varphi F}(e^{\lambda s} - 1)}{\lambda D e^{\lambda s}(e^{\lambda l} - 1)} * (e^{\lambda l} - e^{\lambda s})}{e^{\lambda s} - 1}$$

$$A = C_M - B = C_M$$

$$- \frac{C_{high - C_M} - \dfrac{\lambda D e^{\lambda s}\left(C_{high} - C_M\right) + \dfrac{i}{2\varphi F}(e^{\lambda s} - 1)}{\lambda D e^{\lambda s}(e^{\lambda l} - 1)} * (e^{\lambda l} - e^{\lambda s})}{e^{\lambda s} - 1}$$

Concentration between the electrodes:

$$C(x) = C_M + \left[C_{high} - C_M + \frac{i}{2uF}(e^{\frac{u(l-s)}{\varphi D}} - 1)\right] \frac{(e^{\frac{u}{\varphi D}x} - 1)}{e^{\frac{ul}{\varphi D}} - 1}$$

$$C(x) = C_M + \left[C_{low} - C_M + \frac{i}{2uF}(1 - e^{\frac{u(l-s)}{\varphi D}})\right] \frac{(e^{\frac{u}{\varphi D}x} - 1)}{e^{\frac{ul}{\varphi D}} - 1}$$

Concentration at the electrodes:

$$C = C_{high} + \left[\frac{e^{\frac{us}{\varphi D}}(C_{high} - C_M) - \frac{i}{2uF}(e^{\frac{us}{\varphi D}} - 1)}{e^{\frac{us}{\varphi D}}(e^{\frac{ul}{\varphi D}} - 1)}\right] * (e^{\frac{ux}{\emptyset D}} - e^{\frac{ul}{\varphi D}})$$

$$C = C_{low} + \left[\frac{e^{\frac{us}{\varphi D}}(C_{low} - C_M) + \frac{i}{2uF}(e^{\frac{us}{\varphi D}} - 1)}{e^{\frac{us}{\varphi D}}(e^{\frac{ul}{\varphi D}} - 1)}\right] * \left(e^{\frac{ux}{\varphi D}} - e^{\frac{ul}{\emptyset D}}\right)$$

From eq (4.5), the ASR can be calculated from the following equation:

$$ASR = \frac{D}{\Lambda}\left[\frac{1}{A_1 u_1}\ ln\frac{C_M e^{\frac{u_1 S_1}{\varphi D}}}{A_1 + B_1 e^{\frac{u_1 S_1}{\varphi D}}} + \frac{1}{A_2 u_2}\ ln\frac{A_2 + B_2 e^{\frac{u_2 S_2}{\varphi D}}}{C_M e^{\frac{u_2 S_2}{\varphi D}}}\right]$$

$$u_1 = -u \qquad u_2 = u$$

$$s_1 = s \qquad s_2 = -s$$

$$N_1 = \frac{(C_{low} - C_M) + \frac{i}{2uF}(1 - \frac{1}{e^{\frac{us}{\varphi D}}})}{(e^{\frac{ul}{\varphi D}} - 1)} \qquad N_2 = \frac{-(C_{high} - C_M) + \frac{i}{2uF}(1 - \frac{1}{e^{\frac{us}{\varphi D}}})}{-(e^{\frac{ul}{\varphi D}} - 1)}$$

$$M_1 = C_{low} - N_1 * e^{\frac{ul}{\varphi D}} \qquad M_2 = C_{high} - N_2 * e^{\frac{ul}{\varphi D}}$$

$$B_1 = \frac{C_{low} - C_M - N_1 * (e^{\frac{ul}{\varphi D}} - e^{\frac{us}{\varphi D}})}{e^{\frac{us}{\varphi D}} - 1} \qquad B_2 = \frac{C_{high} - C_M - N_2 * (e^{\frac{ul}{\varphi D}} - e^{\frac{us}{\varphi D}})}{e^{\frac{us}{\varphi D}} - 1}$$

$A_1 = C_M - B_1$ $A_2 = C_M - B_2$

Chapter 5

Conclusion and Future Work

5.1 Conclusion

The pressing issues of clean power generation and global water scarcity have become inextricably linked challenges in our increasingly complex world. There is an urgent need for innovative, sustainable energy sources that can meet our growing needs while safeguarding the environment from the adverse impacts of traditional energy generation methods. Electrochemical approaches are proving to be powerful tools in addressing environmental concerns, particularly in the domains of desalination, wastewater treatment, and power generation.

The electrochemical cell investigated in this study emerges as a promising solution, spanning three critical domains: desalination, separation processes, and power generation. This cell's core functionality relies on the utilization of regenerable porous silver electrodes, which can selectively attract chloride ions through an electrochemical reaction involving silver and chloride. The use of symmetric silver/silver chloride porous electrodes alternately captures Cl^- ions. Here, the silver anode undergoes oxidation and reacts with Cl^- ions from the solution to produce insoluble AgCl, while the silver cathode releases Cl^- ions. What sets this system apart is its novel geometry, allowing the inlet flow to extend outward through the porous electrodes. This innovative feature significantly reduces energy consumption by mitigating concentration polarization through advection, a primary contributor to energy loss in electrochemical processes.

In desalination, we employed analytical, simulation, and experimental methods to assess desalination performance based on separation degree, throughput, charge efficiency, and energy usage. The novel outflow geometry using advection along the ion motion path significantly reduces electrolyte depletion compared to conventional electrochemical deionization methods. This reduction has profound effects on system kinetics and energy consumption. Advection minimizes concentration polarization at the electrodes and lowers electrolyte resistance due to depletion, reducing energy loss at a given flow rate or allowing higher flow rates for a given energy consumption or cell voltage drop. The approach enables superficial membrane velocities over 20 times higher than reverse osmosis (e.g.,

>100 µm/s for the outflow cell compared to ~5 µm/s for RO), making it a compact and practical choice for efficient desalination, particularly in mobile applications.

In the case of electrochemical separation and to address concerns regarding saline water discharge, this study employed a selective electrochemical deionization cell with an outflow geometry to separate Cl^- and SO_4^{2-} ions. By controlling electric fields and velocity, the cell can selectively separate ions, with Cl^- ions responding more quickly due to their higher mobility. A stronger electric field and lower velocity enhance ion separation. The higher electric field attracts chloride ions effectively, while lower velocity allows ions to engage in electrochemical separation processes. Together, these factors substantially improve the separation efficiency, addressing environmental concerns related to saline water discharge.

Lastly, in power generation this study presents an innovative electrochemical cell that utilizes a unique outflow geometry for power generation from salinity gradients. The research involved analyzing the system through steady-state analytical models, focusing on optimizing power generation performance by adjusting parameters like inlet velocities, imposed current, inlet concentrations, and electrode spacing. Enhancing power generation involves increasing the difference in inlet concentrations, reducing electrode spacing, and applying higher current. The velocity also influences performance, with higher velocity leading to increased power density, although there's a decline beyond a certain point due to higher electrode resistance requiring a greater voltage.

The novel outflow geometry of the cell offers continuous electrolyte supply to the electrodes, reducing solution resistance in depleted areas and mitigating concentration polarization. This design enables the cell to operate at higher superficial velocities compared to technologies like PRO and RED, making it a promising solution for harnessing salinity gradient power.

In conclusion, this innovative electrochemical cell presents a multifaceted solution that aligns with the critical need for sustainable energy sources and efficient environmental management.

5.2 Future Work

Future work related to the new outflow geometry of electrochemical cells can be organized into three distinct sections, each with a specific focus on applications

and areas of improvement. These three sections encompass desalination, electrochemical separation, and power generation.

5.2.1 Desalination

The continued pursuit of optimization and innovation within the domain of desalination techniques remains a fundamental endeavor, particularly considering the escalating global demand for freshwater resources.

Future advancements in desalination using outflow electrochemical cells should center on optimization strategies aimed at enhancing the process's overall efficiency, throughput, and sustainability. This involves conducting further research to refine key parameters, including porosity, pore size, the distance between electrodes, and the active area within the desalination system. Moreover, investigating alternative materials like carbon electrodes integrated into the outflow geometry holds the promise of substantial enhancements in desalination effectiveness.

A study by Macías-García et al indicates that lower electrode porosity enhances electrical conductivity and reduces circuit resistance [167]. Conversely, higher electrode porosity creates more electrochemical reaction sites, reducing polarization but resulting in lower electrical conductivity [168,169]. So, the need for lower porosity conditions to minimize both circuit resistance and polarization presents a challenge in enhancing the electrochemical oxidation performance through electrode porosity adjustments. Further research is needed to determine the ideal porosity level that balances these factors for improved desalination performance.

A smaller pore size allows for a higher rate of charge transfer and faster ion transportation through the membrane [170]. However, increasing the pore size of the membrane can be an effective solution to reduce the common problem of clogging in desalination processes. Therefore, it is essential to study and determine the optimal pore size of the membrane for efficient desalination.

The spacing between electrodes plays a crucial role in the efficiency of an electrochemical cell. When the electrode spacing increases, it also increases the system's resistance, leading to decreased energy efficiency [171,172]. On the other hand, a wider spacing allows more time for ions to participate in the electrochemical reaction instead of simply passing through the membrane due to advection flow. This creates a trade-off between the level of desalination achieved and the energy efficiency of the process. Depending on the specific application of

the desalination plant, the electrode spacing can be optimized to achieve the right balance between these factors.

The outflow geometry approach is versatile and can be applied to any porous electrode chemistry. This means it's suitable for desalination batteries with nanoporous carbon electrodes, Faradaic electrodes, or hybrid cells that combine a nanoporous carbon electrode with a Faradaic electrode. The exploration of electrode materials allows for the selection of the most effective materials and configurations, optimizing the cell's performance for a wide array of applications.

5.2.2 Electrochemical Separation

In the field of electrochemical separation, future research should focus on improving the selectivity and efficiency of outflow electrochemical cells in separating various ions. To do this, we must carefully study how these cells can more effectively separate the specific ions we're interested in. This is important for various industries like chemicals and wastewater treatment. The capacity to selectively remove specific ions from complex solutions has broad applications and environmental benefits, making it a key research area in this field.

Conducting simulations will provide insights into how the cell's separation behavior depends on the properties of individual ions and operational factors. These simulations will enable us to predict how other ions can be separated from chloride solutions.

As previously mentioned in Chapter 2 the Fipy package is employed to simulate the desalination process within the cell. In the case of straightforward NaCl desalination, the mass conservation equation for chloride ions is addressed using the discussed boundary conditions. To make this simulation relevant for ion mixtures that go beyond a basic binary electrolyte, it is necessary to solve separate mass conservation equations for all the ions present in the mixture. This expansion of the simulation is essential to handle more complex ion combinations effectively.

The Fipy package will be used to solve the general conservation equations for four different ion species within the system. This will be done in a 1-D setting, considering oscillating polarity but with a constant magnitude of current or voltage conditions at the source and sink. Consequently, we will have four separate mass conservation equations for each of the ions. Additionally, there's a fifth equation that accounts for charge neutrality, and it must be solved alongside the other four mass conservation equations to determine the fifth unknown, which is the electric field (E). Another approach is to estimate the electric field using Ohm's law. By

simultaneously solving these five equations, we can determine both the concentrations of the ions and the value of the electric field. It's important to note that, unlike the simulation in Chapter 2, we can't remove the migration term from the transport equation in this case due to differences in ion mobility values. Consequently, the electric field's determination becomes crucial.

These simulations will offer comprehensive insights into how the mobility of anions influences the separation process. Theoretical analysis suggests that improved separation is achieved for anions with higher mobility values, especially those comparable to or greater than chloride. Conversely, if anions have slower mobility compared to chloride, achieving separation becomes more challenging. In such cases, the lower mobility anions tend to be carried along by the advective current instead of migrating due to the electric field. To thoroughly understand this phenomenon, simulations should be conducted using a range of anions with varying mobility values. Moreover, the simulations will cover cells operating at different current densities and flow rates, providing a comprehensive view of the process under various conditions.

Simulation plays a crucial role in optimizing the design and operational parameters of the cell for chloride and sulfate separations. This optimization is valuable because it helps determine the maximum achievable separation efficiency or the minimum energy needed to reduce the concentration of one of the constituents to a specific level. By fine-tuning the cell's design and operational factors through simulation, we can achieve the most efficient and cost-effective separation process, thus addressing the environmental and economic challenges associated with wastewater treatment and ion separation.

In the electrochemical separation experiments, I only used a mixture of sulfate and chloride ions. However, real-world wastewaters contain a wide variety of different ions. Therefore, it is essential to study how the outflow electrochemical cell behaves when it encounters these diverse ions commonly found in wastewater. This investigation is necessary to ensure the effectiveness of the cell in practical scenarios where multiple types of ions are present.

5.2.3 Power Generation

In the field of power generation, the goal is to enhance the efficiency and applicability of these cells for producing green energy.

Experimental validation of the model in chapter 4 will help us to understand the effect of non-idealities in power generation. Various saline solutions with

different concentrations will be introduced into the existing system through syringe pumps. During experiments, we will measure the current and cell voltage at different flow rates and concentration variations while applying various constraints like fixed current magnitude, fixed voltage magnitude, and fixed load resistance. We will explore different cell designs in this process. The model described in Chapter 4 will serve as a reference to optimize for maximum power density and cell efficiency.

Exploring factors such as porosity, pore size, and electrode materials can provide valuable insights into improving the efficiency and performance of the power generation process. These investigations contribute to the development of more effective and sustainable energy generation methods.

Bibliography

[1] N. Seyedhassantehrani, J. Palko, Outflow geometry for electrochemical desalination cells, Electrochim. Acta. 449 (2023) 142180. https://doi.org/10.1016/J.ELECTACTA.2023.142180.

[2] A.D. Khawaji, I.K. Kutubkhanah, J.-M. Wie, Advances in seawater desalination technologies, Desalination. 221 (2008) 47–69. https://doi.org/10.1016/j.desal.2007.01.067.

[3] C. Fritzmann, J. Löwenberg, T. Wintgens, T. Melin, State-of-the-art of reverse osmosis desalination, Desalination. 216 (2007) 1–76. https://doi.org/10.1016/J.DESAL.2006.12.009.

[4] A.H. Galama, G. Daubaras, O.S. Burheim, H.H.M. Rijnaarts, J.W. Post, Fractioning electrodialysis: a current induced ion exchange process, Electrochim. Acta. 136 (2014) 257–265. https://doi.org/10.1016/J.ELECTACTA.2014.05.104.

[5] A.H. Galama, M. Saakes, H. Bruning, H.H.M. Rijnaarts, J.W. Post, Seawater predesalination with electrodialysis, Desalination. 342 (2014) 61–69. https://doi.org/10.1016/J.DESAL.2013.07.012.

[6] T. Mezher, H. Fath, Z. Abbas, A. Khaled, Techno-economic assessment and environmental impacts of desalination technologies, Desalination. 266 (2011) 263–273. https://doi.org/10.1016/J.DESAL.2010.08.035.

[7] D.A. Roberts, E.L. Johnston, N.A. Knott, Impacts of desalination plant discharges on the marine environment: A critical review of published studies, Water Res. 44 (2010) 5117–5128. https://doi.org/10.1016/J.WATRES.2010.04.036.

[8] S. Lattemann, T. Höpner, Environmental impact and impact assessment of seawater desalination, Desalination. 220 (2008) 1–15. https://doi.org/10.1016/J.DESAL.2007.03.009.

[9] Y. Oren, E. Korngold, N. Daltrophe, R. Messalem, Y. Volkman, L. Aronov, M. Weismann, N. Bouriakov, P. Glueckstern, J. Gilron, Pilot studies on high recovery BWRO-EDR for near zero liquid discharge approach, Desalination. 261 (2010) 321–330. https://doi.org/10.1016/J.DESAL.2010.06.010.

[10] S.G.J. Heijman, H. Guo, S. Li, J.C. van Dijk, L.P. Wessels, Zero liquid discharge: Heading for 99% recovery in nanofiltration and reverse osmosis, Desalination. 236 (2009) 357–362. https://doi.org/10.1016/J.DESAL.2007.10.087.

[11] A. Pérez-González, A.M. Urtiaga, R. Ibáñez, I. Ortiz, State of the art and review on the treatment technologies of water reverse osmosis concentrates, Water Res. 46 (2012) 267–283. https://doi.org/10.1016/j.watres.2011.10.046.

[12] M. Petersková, C. Valderrama, O. Gibert, J.L. Cortina, Extraction of valuable metal ions (Cs, Rb, Li, U) from reverse osmosis concentrate using selective sorbents, Desalination. 286 (2012) 316–323. https://doi.org/10.1016/J.DESAL.2011.11.042.

[13] T. Jeppesen, L. Shu, G. Keir, V. Jegatheesan, Metal recovery from reverse osmosis concentrate, J. Clean. Prod. 17 (2009) 703–707. https://doi.org/10.1016/J.JCLEPRO.2008.11.013.

[14] Y. Tanaka, R. Ehara, S. Itoi, T. Goto, Ion-exchange membrane electrodialytic salt production using brine discharged from a reverse osmosis seawater desalination plant, J. Memb. Sci. 222 (2003) 71–86. https://doi.org/10.1016/S0376-7388(03)00217-5.

[15] M. Turek, Dual-purpose desalination-salt production electrodialysis, Desalination. 153 (2003) 377–381. https://doi.org/10.1016/S0011-9164(02)01131-1.

[16] C. Charcosset, A review of membrane processes and renewable energies for desalination, Desalination. 245 (2009) 214–231. https://doi.org/10.1016/J.DESAL.2008.06.020.

[17] A. Al-Karaghouli, D. Renne, L.L. Kazmerski, Technical and economic assessment of photovoltaic-driven desalination systems, Renew. Energy. 35 (2010) 323–328. https://doi.org/10.1016/J.RENENE.2009.05.018.

[18] S.A. Kalogirou, Seawater desalination using renewable energy sources, Prog. Energy Combust. Sci. 31 (2005) 242–281. https://doi.org/10.1016/J.PECS.2005.03.001.

[19] A. Subramani, M. Badruzzaman, J. Oppenheimer, J.G. Jacangelo, Energy minimization strategies and renewable energy utilization for desalination: A review, Water Res. 45 (2011) 1907–1920. https://doi.org/10.1016/J.WATRES.2010.12.032.

[20] M. Shatat, M. Worall, S. Riffat, Opportunities for solar water desalination worldwide: Review, Sustain. Cities Soc. 9 (2013) 67–80. https://doi.org/10.1016/J.SCS.2013.03.004.

[21] V.G. Gude, N. Nirmalakhandan, S. Deng, Renewable and sustainable approaches for desalination, Renew. Sustain. Energy Rev. 14 (2010) 2641–2654. https://doi.org/10.1016/J.RSER.2010.06.008.

[22] A.M. Helal, Hybridization-a new trend in desalination, Desalin. Water Treat. 3 (2009) 120–135. https://doi.org/10.5004/dwt.2009.263.

[23] A. Zapata-Sierra, M. Cascajares, A. Alcayde, F. Manzano-Agugliaro, Worldwide research trends on desalination, Desalination. 519 (2021) 115305. https://doi.org/10.1016/J.DESAL.2021.115305.

[24] A. Alkaisi, R. Mossad, A. Sharifian-Barforoush, A Review of the Water Desalination Systems Integrated with Renewable Energy, Energy Procedia. 110 (2017) 268–274. https://doi.org/10.1016/j.egypro.2017.03.138.

[25] N. Heck, A. Paytan, D.C. Potts, B. Haddad, Coastal residents' literacy about seawater desalination and its impacts on marine ecosystems in California, Mar. Policy. 68 (2016) 178–186. https://doi.org/10.1016/J.MARPOL.2016.03.004.

[26] A. Panagopoulos, K.J. Haralambous, M. Loizidou, Desalination brine disposal methods and treatment technologies - A review, Sci. Total Environ. 693 (2019) 133545. https://doi.org/10.1016/j.scitotenv.2019.07.351.

[27] E.O. Ezugbe, S. Rathilal, Membrane technologies in wastewater treatment: A review, Membranes (Basel). 10 (2020). https://doi.org/10.3390/membranes10050089.

[28] S. Al-Amshawee, M.Y.B.M. Yunus, A.A.M. Azoddein, D.G. Hassell, I.H. Dakhil, H.A. Hasan, Electrodialysis desalination for water and wastewater: A review, Chem. Eng. J. 380 (2020) 122231.

https://doi.org/10.1016/j.cej.2019.122231.

[29] W.E. Katz, The electrodialysis reversal (EDR) process, Desalination. 28 (1979) 31–40. https://doi.org/10.1016/S0011-9164(00)88124-2.

[30] E. Altıok, T.Z. Kaya, E. Güler, N. Kabay, M. Bryjak, Performance of reverse electrodialysis system for salinity gradient energy generation by using a commercial ion exchange membrane pair with homogeneous bulk structure, Water (Switzerland). 13 (2021). https://doi.org/10.3390/w13060814.

[31] M. Akhter, G. Habib, S.U. Qamar, Application of Electrodialysis in Waste Water Treatment and Impact of Fouling on Process Performance, J. Membr. Sci. Technol. 08 (2018) 182. https://doi.org/10.4172/2155-9589.1000182.

[32] M.E. Suss, S. Porada, X. Sun, P.M. Biesheuvel, J. Yoon, V. Presser, Water desalination via capacitive deionization: What is it and what can we expect from it?, Energy Environ. Sci. 8 (2015) 2296–2319. https://doi.org/10.1039/c5ee00519a.

[33] H. Li, L. Zou, Ion-exchange membrane capacitive deionization: A new strategy for brackish water desalination, Desalination. 275 (2011) 62–66. https://doi.org/10.1016/j.desal.2011.02.027.

[34] J. Lee, S. Kim, C. Kim, J. Yoon, Hybrid capacitive deionization to enhance the desalination performance of capacitive techniques, Energy Environ. Sci. 7 (2014) 3683–3689. https://doi.org/10.1039/c4ee02378a.

[35] M.E. Suss, T.F. Baumann, W.L. Bourcier, C.M. Spadaccini, K.A. Rose, J.G. Santiago, M. Stadermann, Capacitive desalination with flow-through electrodes, Energy Environ. Sci. 5 (2012) 9511. https://doi.org/10.1039/c2ee21498a.

[36] Y. Oren, Capacitive deionization (CDI) for desalination and water treatment - past, present and future (a review), Desalination. 228 (2008) 10–29. https://doi.org/10.1016/j.desal.2007.08.005.

[37] F.A. AlMarzooqi, A.A. Al Ghaferi, I. Saadat, N. Hilal, Application of Capacitive Deionisation in water desalination: A review, Desalination. 342 (2014) 3–15. https://doi.org/10.1016/j.desal.2014.02.031.

[38] T. Kim, C.A. Gorski, B.E. Logan, Low Energy Desalination Using Battery Electrode Deionization, Environ. Sci. Technol. Lett. 4 (2017) 444–449. https://doi.org/10.1021/acs.estlett.7b00392.

[39] M. Pasta, C.D. Wessells, Y. Cui, F. La Mantia, A desalination battery, Nano Lett. 12 (2012) 839–843. https://doi.org/10.1021/nl203889e.

[40] B. Shapira, I. Cohen, T.R. Penki, E. Avraham, D. Aurbach, Energy extraction and water treatment in one system: The idea of using a desalination battery in a cooling tower, J. Power Sources. 378 (2018) 146–152. https://doi.org/10.1016/j.jpowsour.2017.12.039.

[41] K.C. Smith, R. Dmello, Na-Ion Desalination (NID) Enabled by Na-Blocking Membranes and Symmetric Na-Intercalation: Porous-Electrode Modeling, J. Electrochem. Soc. 163 (2016) A530–A539. https://doi.org/10.1149/2.0761603jes.

[42] M. Son, K.H. Cho, K. Jeong, J. Park, Membrane and electrochemical processes for water desalination: A short perspective and the role of nanotechnology, Membranes (Basel). 10 (2020) 1–17. https://doi.org/10.3390/membranes10100280.

[43] D.H. Nam, K.S. Choi, Electrochemical Desalination Using Bi/BiOCl Electrodialysis Cells, ACS Sustain. Chem. Eng. 6 (2018) 15455–15462. https://doi.org/10.1021/acssuschemeng.8b03906.

[44] S. Liu, K.C. Smith, Quantifying the trade-offs between energy consumption and salt removal rate in membrane-free cation intercalation desalination, Electrochim. Acta. 271 (2018) 652–665. https://doi.org/10.1016/j.electacta.2018.03.065.

[45] K.C. Smith, Theoretical evaluation of electrochemical cell architectures using cation intercalation electrodes for desalination, Electrochim. Acta. 230 (2017) 333–341. https://doi.org/10.1016/j.electacta.2017.02.006.

[46] R.W. Peters, L. Shem, Separation of Heavy metals: Removal from Industrial Wastewaters and Contaminated Soil, Symp. Emerg. Sep. Technol. Met. Fuels. (1993) 64.

[47] S. Mandal, B.D. Kulkarni, Separation strategies for processing of dilute

liquid streams, Int. J. Chem. Eng. (2011). https://doi.org/10.1155/2011/659012.

[48] R.W. Baker, MEMBRANE TECHNOLOGY AND APPLICATIONS, 2004. https://doi.org/10.1016/C2009-0-19129-8.

[49] N.K.S. Lawrence K. Wang, Jiaping Paul Chen, Yung-Tse Hung, Membrane and Desalination Technologies, Membr. Desalin. Technol. (2010). https://doi.org/10.1007/978-1-59745-278-6.

[50] H. Strathmann, Membrane separation processes, J. Memb. Sci. 9 (1981) 121–189. https://doi.org/10.1016/S0376-7388(00)85121-2.

[51] C.Y. Chang, I.O.F. Nanofiltration, Chapter 4 Nanofiltration membranes and nanofilters, 2010.

[52] C. Bellona, Nanofiltration – Theory and Application, (n.d.).

[53] M.A. Hafiz, A.H. Hawari, R. Alfahel, M.K. Hassan, A. Altaee, Comparison of nanofiltration with reverse osmosis in reclaiming tertiary treated municipal wastewater for irrigation purposes, Membranes (Basel). 11 (2021) 1–13. https://doi.org/10.3390/membranes11010032.

[54] A.H. Galama, Ion exchange membranes in seawater applications. Processes and characteristics, 2015.

[55] D. Li, Y. Yan, H. Wang, Recent advances in polymer and polymer composite membranes for reverse and forward osmosis processes, Prog. Polym. Sci. 61 (2016) 104–155. https://doi.org/10.1016/j.progpolymsci.2016.03.003.

[56] S. Vara, M. Konni, M.K. Karnena, Membrane technology for treatment of pharmaceutical wastewaters: A novel approach, Handb. Res. Resour. Manag. Pollut. Waste Treat. (2019) 502–530. https://doi.org/10.4018/978-1-7998-0369-0.ch021.

[57] D.W. Green, Perry's Chemical Engineers' Handbook, (2008).

[58] B. Peñate, L. García-Rodríguez, Current trends and future prospects in the design of seawater reverse osmosis desalination technology, Desalination.

284 (2012) 1–8. https://doi.org/10.1016/J.DESAL.2011.09.010.

[59] L.F. Greenlee, D.F. Lawler, B.D. Freeman, B. Marrot, P. Moulin, Reverse osmosis desalination: Water sources, technology, and today's challenges, Water Res. 43 (2009) 2317–2348. https://doi.org/10.1016/j.watres.2009.03.010.

[60] M.M. Pendergast, E.M.V. Hoek, A review of water treatment membrane nanotechnologies, Energy Environ. Sci. 4 (2011) 1946–1971. https://doi.org/10.1039/C0EE00541J.

[61] N. Kansara, Wastewater treatment by ion exchange method: a review of past and recent researches, 2016.

[62] C.J. Gabelich, M.D. Williams, A. Rahardianto, J.C. Franklin, Y. Cohen, High-recovery reverse osmosis desalination using intermediate chemical demineralization, J. Memb. Sci. 301 (2007) 131–141. https://doi.org/10.1016/j.memsci.2007.06.007.

[63] R.S. Gärtner, F.G. Wilhelm, G.J. Witkamp, M. Wessling, Regeneration of mixed solvent by electrodialysis: Selective removal of chloride and sulfate, J. Memb. Sci. 250 (2005) 113–133. https://doi.org/10.1016/j.memsci.2004.10.022.

[64] C. Tang, M.L. Bruening, Ion separations with membranes, J. Polym. Sci. 58 (2020) 2831–2856. https://doi.org/10.1002/pol.20200500.

[65] M.S.H. Bader, Precipitation and Separation of Chloride and Sulfate Ions from Aqueous Solutions: Basic Experimental Performance and Modelling, Environ. Prog. 17 (1998) 126–135. https://doi.org/10.1002/ep.670170220.

[66] Z. Zhou, M. Benbouzid, J. Frédéric Charpentier, F. Scuiller, T. Tang, A review of energy storage technologies for marine current energy systems, Renew. Sustain. Energy Rev. 18 (2013) 390–400. https://doi.org/10.1016/J.RSER.2012.10.006.

[67] D. Lindley, The energy should always work twice, Nature. (2009).

[68] S. Pacala, R. Socolow, Stabilization wedges: solving the climate problem for the next 50 years with current technologies, Science. 305 (2004) 968–972.

https://doi.org/10.1126/SCIENCE.1100103.

[69] B.E. Logan, M. Elimelech, Membrane-based processes for sustainable power generation using water, Nat. 2012 4887411. 488 (2012) 313–319. https://doi.org/10.1038/nature11477.

[70] E. Brauns, Towards a worldwide sustainable and simultaneous large-scale production of renewable energy and potable water through salinity gradient power by combining reversed electrodialysis and solar power?, Desalination. 219 (2008) 312–323. https://doi.org/10.1016/J.DESAL.2007.04.056.

[71] D. Brogioli, R. Zhao, P.M. Biesheuvel, A prototype cell for extracting energy from a water salinity difference by means of double layer expansion in nanoporous carbon electrodes, Energy Environ. Sci. 4 (2011) 772–777. https://doi.org/10.1039/C0EE00524J.

[72] J.W. Post, H.V.M. Hamelers, C.J.N. Buisman, Energy recovery from controlled mixing salt and fresh water with a reverse electrodialysis system, Environ. Sci. Technol. 42 (2008) 5785–5790. https://doi.org/10.1021/ES8004317/ASSET/IMAGES/LARGE/ES-2008-004317_0005.JPEG.

[73] Z. Jia, B. Wang, S. Song, Y. Fan, Blue energy: Current technologies for sustainable power generation from water salinity gradient, Renew. Sustain. Energy Rev. 31 (2014) 91–100. https://doi.org/10.1016/J.RSER.2013.11.049.

[74] B.B. Sales, M. Saakes, J.W. Post, C.J.N. Buisman, P.M. Biesheuvel, H.V.M. Hamelers, Direct power production from a water salinity difference in a membrane-modified supercapacitor flow cell, Environ. Sci. Technol. 44 (2010) 5661–5665. https://doi.org/10.1021/ES100852A/ASSET/IMAGES/LARGE/ES-2010-00852A_0002.JPEG.

[75] L. S, N. RS, Osmotic power plants, Science. 189 (1975) 654. https://doi.org/10.1126/SCIENCE.189.4203.654.

[76] R.S. Norman, Water salination: A source of energy, Science (80-.). 186 (1974) 350–352. https://doi.org/10.1126/SCIENCE.186.4161.350.

[77] R.E. Pattle, Production of Electric Power by mixing Fresh and Salt Water in the Hydroelectric Pile, Nat. 1954 1744431. 174 (1954) 660–660. https://doi.org/10.1038/174660a0.

[78] J. Kuleszo, C. Kroeze, J. Post, B.M. Fekete, The potential of blue energy for reducing emissions of CO2 and non-CO2 greenhouse gases, J. Integr. Environ. Sci. 7 (2010) 89–96. https://doi.org/10.1080/19438151003680850.

[79] S.E. Skilhagen, J.E. Dugstad, R.J. Aaberg, Osmotic power — power production based on the osmotic pressure difference between waters with varying salt gradients, Desalination. 220 (2008) 476–482. https://doi.org/10.1016/J.DESAL.2007.02.045.

[80] R.J. Aaberg, Osmotic power: A new and powerful renewable energy source?, Refocus. 4 (2003) 48–50. https://doi.org/10.1016/S1471-0846(04)00045-9.

[81] K. Nijmeijer, S. Metz, Chapter 5 Salinity Gradient Energy, Sustain. Sci. Eng. 2 (2010) 95–139. https://doi.org/10.1016/S1871-2711(09)00205-0.

[82] G. Micale, A. Cipollina, A. Tamburini, Salinity gradient energy, Sustain. Energy from Salin. Gradients. (2016) 1–17. https://doi.org/10.1016/B978-0-08-100312-1.00001-8.

[83] K. Saito, M. Irie, S. Zaitsu, H. Sakai, H. Hayashi, A. Tanioka, Power generation with salinity gradient by pressure retarded osmosis using concentrated brine from SWRO system and treated sewage as pure water, Desalin. Water Treat. 41 (2012) 114–121. https://doi.org/10.1080/19443994.2012.664696.

[84] A. Achilli, T.Y. Cath, A.E. Childress, Power generation with pressure retarded osmosis: An experimental and theoretical investigation, J. Memb. Sci. 343 (2009) 42–52. https://doi.org/10.1016/J.MEMSCI.2009.07.006.

[85] J. Jagur-Grodzinskr, R. Kramer, Novel Process for Direct Conversion of Free Energy of Mixing into Electric Power, Ind. Eng. Chem. Process Des. Dev. 25 (1986) 443–449. https://doi.org/10.1021/I200033A016/ASSET/I200033A016.FP.PNG_V03.

[86] N.Y. Yip, D. Brogioli, H.V.M. Hamelers, K. Nijmeijer, Salinity gradients

for sustainable energy: Primer, progress, and prospects, Environ. Sci. Technol. 50 (2016) 12072–12094. https://doi.org/10.1021/acs.est.6b03448.

[87] S. Zhang, G. Han, X. Li, C. Wan, T.S. Chung, Pressure retarded osmosis: Fundamentals, Sustain. Energy from Salin. Gradients. (2016) 19–53. https://doi.org/10.1016/B978-0-08-100312-1.00002-X.

[88] A. Achilli, A.E. Childress, Pressure retarded osmosis: From the vision of Sidney Loeb to the first prototype installation — Review, Desalination. 261 (2010) 205–211. https://doi.org/10.1016/J.DESAL.2010.06.017.

[89] F. Helfer, C. Lemckert, Y.G. Anissimov, Osmotic power with Pressure Retarded Osmosis: Theory, performance and trends – A review, J. Memb. Sci. 453 (2014) 337–358. https://doi.org/10.1016/J.MEMSCI.2013.10.053.

[90] J. Veerman, D.A. Vermaas, Reverse electrodialysis: Fundamentals, Sustain. Energy from Salin. Gradients. (2016) 77–133. https://doi.org/10.1016/B978-0-08-100312-1.00004-3.

[91] R.A. Rica, R. Ziano, D. Salerno, F. Mantegazza, R. van Roij, D. Brogioli, Capacitive mixing for harvesting the free energy of solutions at different concentrations, Entropy. 15 (2014) 1388–1407. https://doi.org/10.3390/e15041388.

[92] F. La Mantia, M. Pasta, H.D. Deshazer, B.E. Logan, Y. Cui, Batteries for efficient energy extraction from a water salinity difference, Nano Lett. 11 (2011) 1810–1813. https://doi.org/10.1021/nl200500s.

[93] D. Brogioli, Extracting renewable energy from a salinity difference using a capacitor, Phys. Rev. Lett. 103 (2009) 058501. https://doi.org/10.1103/PHYSREVLETT.103.058501/FIGURES/4/MEDIUM.

[94] W. Guo, L. Cao, J. Xia, F.Q. Nie, M. Wen, J. Xue, Y. Song, D. Zhu, Y. Wang, L. Jiang, Energy Harvesting with Single-Ion-Selective Nanopores: A Concentration-Gradient-Driven Nanofluidic Power Source, Adv. Funct. Mater. 20 (2010) 1339–1344. https://doi.org/10.1002/ADFM.200902312.

[95] M. Olsson, G.L. Wick, J.D. Isaacs, Salinity Gradient Power: Utilizing Vapor Pressure Differences, Science (80-.). 206 (1979) 452–454.

https://doi.org/10.1126/SCIENCE.206.4417.452.

[96] S. van der Zwan, I.W.M. Pothof, B. Blankert, J.I. Bara, Feasibility of osmotic power from a hydrodynamic analysis at module and plant scale, J. Memb. Sci. 389 (2012) 324–333. https://doi.org/10.1016/J.MEMSCI.2011.10.044.

[97] J.W. Post, J. Veerman, H.V.M. Hamelers, G.J.W. Euverink, S.J. Metz, K. Nymeijer, C.J.N. Buisman, Salinity-gradient power: Evaluation of pressure-retarded osmosis and reverse electrodialysis, J. Memb. Sci. 288 (2007) 218–230. https://doi.org/10.1016/J.MEMSCI.2006.11.018.

[98] O. Levenspiel, N. De Nevers, The osmotic pump, Science (80-.). 183 (1974) 157. https://doi.org/10.1126/SCIENCE.183.4121.157.

[99] Z.R. Xu, C.G. Yang, C.H. Liu, Z. Zhou, J. Fang, J.H. Wang, An osmotic micro-pump integrated on a microfluidic chip for perfusion cell culture, Talanta. 80 (2010) 1088–1093. https://doi.org/10.1016/J.TALANTA.2009.08.031.

[100] Q. She, X. Jin, C.Y. Tang, Osmotic power production from salinity gradient resource by pressure retarded osmosis: Effects of operating conditions and reverse solute diffusion, J. Memb. Sci. 401–402 (2012) 262–273. https://doi.org/10.1016/J.MEMSCI.2012.02.014.

[101] E. Sivertsen, T. Holt, W. Thelin, G. Brekke, Modelling mass transport in hollow fibre membranes used for pressure retarded osmosis, J. Memb. Sci. 417–418 (2012) 69–79. https://doi.org/10.1016/J.MEMSCI.2012.06.014.

[102] R.L. McGinnis, M. Elimelech, Global challenges in energy and water supply: The promise of engineered osmosis, Environ. Sci. Technol. 42 (2008) 8625–8629. https://doi.org/10.1021/ES800812M/ASSET/IMAGES/LARGE/ES-2008-00812M_0004.JPEG.

[103] R.L. McGinnis, M. Elimelech, Energy requirements of ammonia–carbon dioxide forward osmosis desalination, Desalination. 207 (2007) 370–382. https://doi.org/10.1016/J.DESAL.2006.08.012.

[104] T. Thorsen, T. Holt, The potential for power production from salinity gradients by pressure retarded osmosis, J. Memb. Sci. 335 (2009) 103–110.

https://doi.org/10.1016/J.MEMSCI.2009.03.003.

[105] J.N. Weinstein, F.B. Leitz, Electric Power from Differences in Salinity: The Dialytic Battery, Science (80-.). 191 (1976) 557–559. https://doi.org/10.1126/SCIENCE.191.4227.557.

[106] D.A. Vermaas, E. Guler, M. Saakes, K. Nijmeijer, Theoretical power density from salinity gradients using reverse electrodialysis, Energy Procedia. 20 (2012) 170–184. https://doi.org/10.1016/J.EGYPRO.2012.03.018.

[107] J. Veerman, R.M. de Jong, M. Saakes, S.J. Metz, G.J. Harmsen, Reverse electrodialysis: Comparison of six commercial membrane pairs on the thermodynamic efficiency and power density, J. Memb. Sci. 343 (2009) 7–15. https://doi.org/10.1016/J.MEMSCI.2009.05.047.

[108] J. Veerman, M. Saakes, S.J. Metz, G.J. Harmsen, Reverse electrodialysis: Evaluation of suitable electrode systems, J. Appl. Electrochem. 40 (2010) 1461–1474. https://doi.org/10.1007/S10800-010-0124-8/TABLES/3.

[109] J. Veerman, M. Saakes, S.J. Metz, G.J. Harmsen, Reverse electrodialysis: Performance of a stack with 50 cells on the mixing of sea and river water, J. Memb. Sci. 327 (2009) 136–144. https://doi.org/10.1016/J.MEMSCI.2008.11.015.

[110] P. Długołecki, J. Dabrowska, K. Nijmeijer, M. Wessling, Ion conductive spacers for increased power generation in reverse electrodialysis, J. Memb. Sci. 347 (2010) 101–107. https://doi.org/10.1016/J.MEMSCI.2009.10.011.

[111] B.B. Sales, F. Liu, O. Schaetzle, C.J.N. Buisman, H.V.M. Hamelers, Electrochemical characterization of a supercapacitor flow cell for power production from salinity gradients, Electrochim. Acta. 86 (2012) 298–304. https://doi.org/10.1016/J.ELECTACTA.2012.05.069.

[112] O. Burheim, B.B. Sales, O. Schaetzle, F. Liu, H.V.M. Hamelers, Auto Generative Capacitive Mixing for Power Conversion of Sea and River Water by the Use of Membranes, J. Energy Resour. Technol. Trans. ASME. 135 (2013). https://doi.org/10.1115/1.4007717/368050.

[113] Z. Jia, B. Wang, S. Song, Y. Fan, A membrane-less Na ion battery-based CAPMIX cell for energy extraction using water salinity gradients, RSC Adv.

3 (2013) 26205–26209. https://doi.org/10.1039/C3RA44902E.

[114] S.H.M.H. Tehrani, S.A. Seyedsadjadi, A. Ghaffarinejad, Application of electrodeposited cobalt hexacyanoferrate film to extract energy from water salinity gradients, RSC Adv. 5 (2015) 30032–30037. https://doi.org/10.1039/C5RA03909F.

[115] S. Alzahrani, A.W. Mohammad, N. Hilal, P. Abdullah, O. Jaafar, Comparative study of NF and RO membranes in the treatment of produced water-Part I: Assessing water quality, Desalination. 315 (2013) 18–26. https://doi.org/10.1016/j.desal.2012.12.004.

[116] M. Talaeipour, J. Nouri, A.H. Hassani, A.H. Mahvi, An investigation of desalination by nanofiltration, reverse osmosis and integrated (hybrid NF/RO) membranes employed in brackish water treatment, J. Environ. Heal. Sci. Eng. 15 (2017) 1–9. https://doi.org/10.1186/s40201-017-0279-x.

[117] A. Shrivastava, S. Rosenberg, M. Peery, Energy efficiency breakdown of reverse osmosis and its implications on future innovation roadmap for desalination, Desalination. 368 (2015) 181–192. https://doi.org/10.1016/j.desal.2015.01.005.

[118] S. Porada, R. Zhao, A. Van Der Wal, V. Presser, P.M. Biesheuvel, Review on the science and technology of water desalination by capacitive deionization, Prog. Mater. Sci. 58 (2013) 1388–1442. https://doi.org/10.1016/j.pmatsci.2013.03.005.

[119] S. Jiang, H. Sun, H. Wang, B.P. Ladewig, Z. Yao, A comprehensive review on the synthesis and applications of ion exchange membranes, Chemosphere. 282 (2021) 130817. https://doi.org/10.1016/j.chemosphere.2021.130817.

[120] D.H. Nam, M.A. Lumley, K.S. Choi, Electrochemical Redox Cells Capable of Desalination and Energy Storage: Addressing Challenges of the Water-Energy Nexus, ACS Energy Lett. 6 (2021) 1034–1044. https://doi.org/10.1021/acsenergylett.0c02399.

[121] P. Srimuk, X. Su, J. Yoon, D. Aurbach, V. Presser, Charge-transfer materials for electrochemical water desalination, ion separation and the recovery of elements, Nat. Rev. Mater. 5 (2020) 517–538.

https://doi.org/10.1038/s41578-020-0193-1.

[122] J. Ahn, J. Lee, S. Kim, C. Kim, J. Lee, P.M. Biesheuvel, J. Yoon, High performance electrochemical saline water desalination using silver and silver-chloride electrodes, Desalination. 476 (2020). https://doi.org/10.1016/j.desal.2019.114216.

[123] P. Srimuk, S. Husmann, V. Presser, Low voltage operation of a silver/silver chloride battery with high desalination capacity in seawater, RSC Adv. 9 (2019) 14849–14858. https://doi.org/10.1039/c9ra02570g.

[124] J. Ahn, S. Kim, S. il Jeon, C. Lee, P.M. Biesheuvel, J. Lee, J. Yoon, New method for electrochemical ion separation (ElONS) for chloride/nitrate separation using Ag/AgCl electrodes with a cation exchange membrane, J. Environ. Chem. Eng. 9 (2021) 106876. https://doi.org/10.1016/j.jece.2021.106876.

[125] J. Lee, S. Kim, J. Yoon, Rocking Chair Desalination Battery Based on Prussian Blue Electrodes, ACS Omega. 2 (2017) 1653–1659. https://doi.org/10.1021/acsomega.6b00526.

[126] W. Tang, J. Liang, D. He, J. Gong, L. Tang, Z. Liu, D. Wang, G. Zeng, Various cell architectures of capacitive deionization: Recent advances and future trends, Water Res. 150 (2019) 225–251. https://doi.org/10.1016/j.watres.2018.11.064.

[127] A. Kalfa, B. Shapira, A. Shopin, I. Cohen, E. Avraham, D. Aurbach, Capacitive deionization for wastewater treatment: Opportunities and challenges, Chemosphere. 241 (2020) 125003. https://doi.org/10.1016/j.chemosphere.2019.125003.

[128] J. Wang, J. Dai, Z. Jiang, B. Chu, F. Chen, Recent progress and prospect of flow-electrode electrochemical desalination system, Desalination. 504 (2021) 114964. https://doi.org/10.1016/j.desal.2021.114964.

[129] Y.U. Shin, J. Lim, C. Boo, S. Hong, Improving the feasibility and applicability of flow-electrode capacitive deionization (FCDI): Review of process optimization and energy efficiency, Desalination. 502 (2021) 114930. https://doi.org/10.1016/j.desal.2021.114930.

[130] E. Avraham, Y. Bouhadana, A. Soffer, D. Aurbach, Limitation of Charge Efficiency in Capacitive Deionization, J. Electrochem. Soc. 156 (2009) P95. https://doi.org/10.1149/1.3115463.

[131] J.C. Farmer, D. V. Fix, G. V. Mack, R.W. Pekala, J.F. Poco, Capacitive deionization of NH4ClO4 solutions with carbon aerogel electrodes, J. Appl. Electrochem. 26 (1996) 1007–1018. https://doi.org/10.1007/BF00242195.

[132] A. Hemmatifar, J.W. Palko, M. Stadermann, J.G. Santiago, Energy breakdown in capacitive deionization, Water Res. 104 (2016) 303–311. https://doi.org/10.1016/j.watres.2016.08.020.

[133] E.N. Guyes, A.N. Shocron, A. Simanovski, P.M. Biesheuvel, M.E. Suss, A one-dimensional model for water desalination by flow-through electrode capacitive deionization, Desalination. 415 (2017) 8–13. https://doi.org/10.1016/j.desal.2017.03.013.

[134] Y. Qu, P.G. Campbell, A. Hemmatifar, J.M. Knipe, C.K. Loeb, J.J. Reidy, M.A. Hubert, M. Stadermann, J.G. Santiago, Charging and Transport Dynamics of a Flow-Through Electrode Capacitive Deionization System, J. Phys. Chem. B. 122 (2018) 240–249. https://doi.org/10.1021/acs.jpcb.7b09168.

[135] J. Janata, Potentiometric Sensors, in: Princ. Chem. Sensors, Springer US, Boston, MA, 2009: pp. 119–199. https://doi.org/10.1007/b136378_6.

[136] A.I. Masliy, N.P. Poddubny, Influence of solid phase conductivity on spatial localization of electrochemical processes in flow-through porous electrodes Part I: Electrodes with uniform conducting matrix, J. Appl. Electrochem. 27 (1997) 1036–1044. https://doi.org/10.1023/A:1018430408634/METRICS.

[137] H. Ha, J. Payer, The effect of silver chloride formation on the kinetics of silver dissolution in chloride solution, Electrochim. Acta. 56 (2011) 2781–2791. https://doi.org/10.1016/j.electacta.2010.12.050.

[138] R. Hołyst, A. Poniewierski, Electrochemical Systems, Thermodyn. Chem. Phys. Eng. (2012) 245–263. https://doi.org/10.1007/978-94-007-2999-5_11.

[139] J. Newman, K.E. Thomas-Alyea, Electrochemical Systems, John Wiley Sons. (2012).

[140] P.M. Biesheuvel, Y. Fu, M.Z. Bazant, Electrochemistry and capacitive charging of porous electrodes in asymmetric multicomponent electrolytes, Russ. J. Electrochem. 48 (2012) 580–592. https://doi.org/10.1134/S1023193512060031/METRICS.

[141] R. Zhao, M. van Soestbergen, H.H.M. Rijnaarts, A. van der Wal, M.Z. Bazant, P.M. Biesheuvel, Time-dependent ion selectivity in capacitive charging of porous electrodes, J. Colloid Interface Sci. 384 (2012) 38–44. https://doi.org/10.1016/J.JCIS.2012.06.022.

[142] A.N. Colli, J.M. Bisang, Tertiary Current and Potential Distribution including Laminar/Turbulent Convection, Diffusion, and Migration by the Finite Volume Method Using OpenFOAM, Ind. Eng. Chem. Res. 60 (2021) 11927–11941. https://doi.org/10.1021/ACS.IECR.1C01884/ASSET/IMAGES/LARGE/IE1C01884_0012.JPEG.

[143] S. Moshtarikhah, N.A.W. Oppers, M.T. de Groot, J.T.F. Keurentjes, J.C. Schouten, J. van der Schaaf, Nernst–Planck modeling of multicomponent ion transport in a Nafion membrane at high current density, J. Appl. Electrochem. 47 (2017) 51–62. https://doi.org/10.1007/s10800-016-1017-2.

[144] J.E. Guyer, D. Wheeler, J.A. Warren, FiPy: Partial Differential Equations with Python, Comput. Sci. Eng. 11 (2009) 6–15. https://doi.org/10.1109/MCSE.2009.52.

[145] A.N. Colli, H.H. Girault, Compact and General Strategy for Solving Current and Potential Distribution in Electrochemical Cells Composed of Massive Monopolar and Bipolar Electrodes, J. Electrochem. Soc. 164 (2017) E3465–E3472. https://doi.org/10.1149/2.0471711JES/XML.

[146] D.R. Lide, CRC Handbook of Chemistry and Physics: A Ready-Reference of Chemical and Physical Data, 85th ed Edited by David R. Lide (National Institute of Standards and Technology). CRC Press LLC: Boca Raton, FL. 2004. 2712 pp. $139.99. ISBN 0-8493-0485-7., J. Am. Chem. Soc. 127 (2005) 4542–4542. https://doi.org/10.1021/ja041017a.

[147] A.N. Colli, J.M. Bisang, A multi-region and open-source computational fluid dynamic tool for electrochemical systems with three-dimensional electrodes, AIChE J. 67 (2021) e17371. https://doi.org/10.1002/AIC.17371.

[148] F. Pargar, D. Koleva, Polarization Behaviour of Silver in Model Solutions, Int. J. Struct. Civ. Eng. Res. (2017) 172–176. https://doi.org/10.18178/ijscer.6.3.172-176.

[149] S.K. Patel, P.M. Biesheuvel, M. Elimelech, Energy Consumption of Brackish Water Desalination: Identifying the Sweet Spots for Electrodialysis and Reverse Osmosis, ACS ES&T Eng. 1 (2021) 851–864. https://doi.org/10.1021/acsestengg.0c00192.

[150] L. Wang, C. Violet, R.M. DuChanois, M. Elimelech, Derivation of the Theoretical Minimum Energy of Separation of Desalination Processes, J. Chem. Educ. 97 (2020) 4361–4369. https://doi.org/10.1021/acs.jchemed.0c01194.

[151] J. Kucera, Flux, in: Reverse Osmosis - Ind. Process. Appl. (2nd Ed., John Wiley & Sons, 2015.

[152] Z. Yang, X.-H. Ma, C.Y. Tang, Recent development of novel membranes for desalination, Desalination. 434 (2018) 37–59. https://doi.org/10.1016/j.desal.2017.11.046.

[153] F.A.L. DULLIEN, Multiphase Flow of Immiscible Fluids in Porous Media, in: Porous Media, Elsevier, 1992: pp. 333–485. https://doi.org/10.1016/b978-0-12-223651-8.50011-0.

[154] L. Song, C. Liu, A total salt balance model for concentration polarization in crossflow reverse osmosis channels with shear flow, J. Memb. Sci. 401–402 (2012) 313–322. https://doi.org/10.1016/j.memsci.2012.02.023.

[155] N. Seyedhassantehrani, J.W. Palko, Microfluidic Ionic Separations Using Selective Electrodes, in: 2020 Virtual AIChE Annu. Meet., 2020. https://www.aiche.org/academy/conferences/aiche-annual-meeting/2020/proceeding/paper/347r-microfluidic-ionic-separations-using-selective-electrodes.

[156] Z.Q. Yan, L.M. Zeng, Q. Li, T.Y. Liu, H. Matsuyama, X.L. Wang, Selective separation of chloride and sulfate by nanofiltration for high saline wastewater recycling, Sep. Purif. Technol. 166 (2016) 135–141. https://doi.org/10.1016/j.seppur.2016.04.009.

[157] R.S. Gawaad, S.K. Sharma, S.S. Sambi, Sodium Sulphate Recovery from Industrial Wastewater Using Nano-Membranes: a Review, Int. Rev. Chem. Eng. 3 (2011) 392–398.

[158] N. Hilal, V. Kochkodan, H. Al Abdulgader, S. Mandale, S.A. Al-Jlil, A combined ion exchange-nanofiltration process for water desalination: I. sulphate-chloride ion-exchange in saline solutions, Desalination. 363 (2015) 44–50. https://doi.org/10.1016/j.desal.2014.11.016.

[159] Deepti, A. Sinha, P. Biswas, S. Sarkar, U. Bora, M.K. Purkait, Separation of chloride and sulphate ions from nanofiltration rejected wastewater of steel industry, J. Water Process Eng. 33 (2020) 101108. https://doi.org/10.1016/j.jwpe.2019.101108.

[160] M. Reig, C. Valderrama, O. Gibert, J.L. Cortina, Selectrodialysis and bipolar membrane electrodialysis combination for industrial process brines treatment: Monovalent-divalent ions separation and acid and base production, 2016. https://doi.org/10.1016/j.desal.2016.08.010.

[161] A.T. Besha, M.T. Tsehaye, D. Aili, W. Zhang, R.A. Tufa, Design of monovalent ion selective membranes for reducing the impacts of multivalent ions in reverse electrodialysis, Membranes (Basel). 10 (2020). https://doi.org/10.3390/membranes10010007.

[162] W.L. Marshall, R. Slusher, Thermodynamics of calcium sulfate dihydrate in aqueous sodium chloride solutions, 0-110°, 1966. https://doi.org/10.1021/j100884a044.

[163] Y. Zhang, Z. Yang, D. Guo, H. Geng, C. Dong, Effect of Chloride Salts and Bicarbonate on Solubility of CaSO4 in Aqueous Solutions at 37°C, Procedia Environ. Sci. 18 (2013) 84–91. https://doi.org/10.1016/j.proenv.2013.04.012.

[164] M.V.I. and S.A. Bushmin, Empirical model of the Gibbs free energy for saline solutions of arbitrary concentration: Application for H2O–NaCl solutions at 423.15 K-573.15 K and pressures from saturation up to 5 kbar, (2007) 1–26. https://arxiv.org/ftp/arxiv/papers/1705/1705.02901.pdf (accessed March 22, 2018).

[165] N.Y. Yip, D.A. Vermaas, K. Nijmeijer, M. Elimelech, Thermodynamic,

energy efficiency, and power density analysis of reverse electrodialysis power generation with natural salinity gradients, Environ. Sci. Technol. 48 (2014) 4925–4936. https://doi.org/10.1021/es5005413.

[166] N.Y. Yip, M. Elimelech, Thermodynamic and energy efficiency analysis of power generation from natural salinity gradients by pressure retarded osmosis, Environ. Sci. Technol. 46 (2012) 5230–5239. https://doi.org/10.1021/es300060m.

[167] A. Macías-García, M.A. Díaz-Díez, M. Alfaro-Domínguez, J.P. Carrasco-Amador, Influence of chemical composition, porosity and fractal dimension on the electrical conductivity of carbon blacks, Heliyon. (2017) e04024. https://doi.org/10.1016/j.heliyon.2020.e04024.

[168] J. Lai, A. Nsabimana, R. Luque, G. Xu, 3D Porous Carbonaceous Electrodes for Electrocatalytic Applications, Joule. 2 (2018) 76–93. https://doi.org/10.1016/j.joule.2017.10.005.

[169] G. Wang, Y. Liu, Y. Duan, J. Ye, Z. Lin, Effects of porosity on the electrochemical oxidation performance of Ti4O7 electrode materials, Ceram. Int. 49 (2023) 15357–15364. https://doi.org/10.1016/J.CERAMINT.2023.01.120.

[170] M. Nasir, Y. Nakanishi, A. Patmonoaji, T. Suekane, Effects of porous electrode pore size and operating flow rate on the energy production of capacitive energy extraction, Renew. Energy. 155 (2020) 278–285. https://doi.org/10.1016/J.RENENE.2020.03.163.

[171] A. Aldalbahi, M. Rahaman, M. Almoiqli, A. Hamedelniel, A. Alrehaili, Single-Walled Carbon Nanotube (SWCNT) Loaded Porous Reticulated Vitreous Carbon (RVC) Electrodes Used in a Capacitive Deionization (CDI) Cell for Effective Desalination, Nanomaterials. 8 (2018). https://doi.org/10.3390/NANO8070527.

[172] N.I. Madondo, S. Rathilal, B.F. Bakare, E.K. Tetteh, Effect of Electrode Spacing on the Performance of a Membrane-Less Microbial Fuel Cell with Magnetite as an Additive, Mol. 2023, Vol. 28, Page 2853. 28 (2023) 2853. https://doi.org/10.3390/MOLECULES28062853.